EFFECT OF CORROSION ON THE SEISMIC RESPONSE OF A SINGLE-BENT, REINFORCED CONCRETE BRIDGE

A Thesis

by

JESSICA ANNE HARVAT

Submitted to the Office of Graduate Studies of
Texas A&M University
in partial fulfillment of the requirements for the degree of

MASTER OF SCIENCE

May 2009

Major Subject: Civil Engineering

EFFECT OF CORROSION ON THE SEISMIC RESPONSE OF A SINGLE-BENT, REINFORCED CONCRETE BRIDGE

A Thesis

by

JESSICA ANNE HARVAT

Submitted to the Office of Graduate Studies of
Texas A&M University
in partial fulfillment of the requirements for the degree of

MASTER OF SCIENCE

Approved by:

Chair of Committee,	Joseph M. Bracci
Committee Members,	Paolo Gardoni
	David Woodcock
Head of Department,	David V. Rosowsky

May 2009

Major Subject: Civil Engineering

ABSTRACT

Effect of Corrosion on the Seismic Response of a Single-Bent, Reinforced Concrete Bridge. (May 2009)

Jessica Anne Harvat, B.S., Texas A&M University

Chair of Advisory Committee: Dr. Joseph M. Bracci

The effect of corrosion on a single-bent, reinforced concrete (RC) bridge subject to seismic loading is the primary focus of this research. This work attempts to determine the effects of decreasing rebar diameter and concrete cover spalling on the strength and stiffness of the RC bridge. The application of these results to the field of historic preservation will also be explored.

Through the use of static and dynamic analyses, this research shows that the effects of corrosion only have a slight influence on the seismic fragility of the RC bridge. The loss of three inches of concrete cover from the bridge column is shown to have a greater effect on the strength and stiffness of the bridge than decreasing the rebar diameter by 10%. The deformation capacity and demand both increase for bridges with reduced reinforcing steel and concrete cover; however, the capacity increases to a greater degree than the demand. The seismic fragility of the bridge based on deformation criteria is greatest for the pristine structure, and it decreases as the level of damage increases. Future work should include verifying the hysteretic behavior by accounting for reinforcement slip caused by a loss of bond.

ACKNOWLEDGEMENTS

I would like to thank my committee chair, Dr. Bracci, for his guidance and mentorship over the past three years. I would also like to thank my committee members, Dr. Gardoni and Prof. Woodcock, for their guidance and support throughout the course of this research.

I also wish to say thanks to all of my friends and peers within the department who have helped me through my masters degree. A special thanks goes to Qindan Huang and Jinquan Zhong for their immense help with computer models, software, and general advice.

Additionally, the Texas A&M Association of Former Students and the Office of Graduate Studies deserve a heartfelt thank you for supplying the initial funding for my degree through the Graduate Merit Fellowship. My appreciation goes to Dr. Bracci, Dr. Barroso, and Dr. David V. Rosowsky for writing recommendation letters for this award, as well to Dr. Tony Cahill for compiling and submitting my nomination.

I also want to extend my gratitude to the National Science Foundation (NSF) which provided the fellowship that supported me through the latter part of my research. Special thanks go to Dr. Bracci, Dr. Barroso, Dr. Rosowsky, Prof. Woodcock, and Mr. Pat Sparks for believing in my abilities enough to write recommendations for me to the NSF Graduate Research Fellowship Program.

Finally, thanks to my parents and sisters for their encouragement and to my husband, Matthew, for his patience, love, and support throughout this process.

TABLE OF CONTENTS

Page

LIST OF FIGURES

Page

Page

LIST OF TABLES

Page

Page

1. INTRODUCTION

Aging infrastructure is currently a problem which is plaguing the United States and costing taxpayers billions of dollars each year. In 2005, the American Society of Civil Engineers (ASCE) estimated that the United States needed to invest $1.6 trillion dollars into its infrastructure system over the following 5 years; additionally, it was estimated the cost would be $9.4 billion each year for the next 20 years to fix all bridge deficiencies (ASCE 2005). In 2002, the National Association of Corrosion Engineers (NACE) reported that the total annual cost that is directly related to corrosion in infrastructure is $22.6 billion (NACE 2002). Recently, the *Concrete Repair Bulletin* estimated that the annual cost for rehabilitation, repair, protection, and strengthening of concrete structures is $18-$20 billion (Emmons and Sordyl 2006). The maintenance, repair, and replacement costs for deteriorating existing structures are substantial; therefore, an undisputed need exists for understanding the behavior of existing structures and for developing strategies to optimize the use of current resources (Vu and Stewart 2000).

Corrosion of steel reinforcing bars (rebar) in concrete is a common, natural phenomenon which can accelerate the rate of deterioration of a structure, and it has the potential to affect all types of reinforced concrete (RC) structures. Specifically, Vu and Stewart (2000) mentioned corrosion as one of the primary causes of deterioration in bridge decks and piers. Corrosion in reinforced concrete is initiated when chloride ions

---

This thesis follows the style of *Journal of Structural Engineering*.

penetrate the concrete cover, which ranges from about 1.5” to about 3” for bridge structures, and react with the reinforcing steel. The ensuing chemical process alters the mechanical and physical properties of the steel material. Once the corrosion process begins, the effective area of the corroding rebar decreases while corrosion byproducts, such as rust, form simultaneously on the surface of the bars; this causes an expansion in volume which displaces the concrete. The pressure created by the corrosion process is localized at the interface between the steel and the concrete and induces tensile stresses in the concrete. The tensile stresses can then lead to external cracking and eventual concrete cover spalling (Ghandehari et al. 2000; Vu and Stewart 2000).

In high seismic regions, such as California, concrete deterioration and rebar corrosion over time may weaken structures and make them more vulnerable to future earthquake hazards. The effects of both rebar corrosion and the subsequent spalling of the concrete cover are the focus of this work. An example single-bent, RC bridge designed based on typical California specifications for seismic loads is used to illustrate the effects of corrosion and spalling on the dynamic response of RC bridges. More specifically, this work attempts to determine the resulting effects on the strength and stiffness of RC bridges. Additionally, the results of this work will be compared with the results from previous work (Choe et al. 2007a, 2008) which studied the effect of corrosion on a similar bridge, neglecting the effect of changes in stiffness resulting from concrete cover spalling.

The results of this work can be used by engineers to assess the structural performance of existing structures. The preservation and rehabilitation of historic

structures is important because of their value to the community. The results of this work can be widely applied to historic RC structures in seismic regions that are affected by corrosion in order to help determine the structural integrity over time. This work will help enable engineers to more accurately evaluate and understand the condition and level of safety for corroding RC structures under seismic loading. It will also allow engineers to evaluate alternative approaches to repair and improve the performance of historic bridges with minimal impact on their historic appearance.

In this thesis, a literature review of the current work in the field that relates to this topic will be presented followed by a specific description and verification of the analytical model. Subsequently, the detailed results of this work will be given. A summary of all results, conclusions, and suggestions for future work can be found at the end of this thesis. More details to supplement the work provided herein can be found in the Appendices.

2. LITERATURE REVIEW

In order to understand the current state of knowledge regarding the issue of corrosion in reinforced concrete bridges and the applications of previous work to the field of historic preservation, a literature review was performed. The main topics of interest were the effect of rebar corrosion and cover thickness on the strength and stiffness of a concrete specimen. Additionally, previous research and case studies performed on historic structures subject to corrosion were reviewed. Supplemental literature review material can be found in APPENDIX A.

2.1 Strength

There has been a substantial amount of work done to document the effect of corrosion on the strength of RC elements. One issue confronting such structures is the loss of bond strength at the interface between the rebar and the concrete during the corrosion process. Al-Sulaimani et al. (1990) showed that the effect of bond strength is relatively substantial when no concrete confinement is present. However, work performed by Ghandehari et al. (2000) shows that the effect of corrosion on bond strength is negligible when a high percentage of confining transverse steel is used. Because the bridge column in this research is designed based on the seismic provisions of California that require high transverse steel ratios in columns to confine the core concrete and ensure significant deformation before failure, the loss of bond strength is neglected in this work. Based on this same justification, Choe et al. (2007a) made the assumption that the bond strength is negligible when corrosion effects on a RC bridge column are considered.

Work performed by Castel et al. (2000) examined the ultimate behavior of corroded RC specimens in the lab and found that beams with corrosion in the tensile region typically exhibited a decrease in strength of approximately 20%. This value corresponds almost directly with the average maximum reduction in the cross-sectional area of the tensile region steel rebar (Castel et al. 2000). This means that knowing the percent decrease in the rebar area (which can be obtained by field testing) should allow the prediction of the expected decrease in strength; this result is supported by the first principle in bending theory and the ACI design equations where the strength is directly proportional to the cross-sectional area of the steel (ACI 2008). Thus, this work reported that a decrease in bond strength has little effect on the ultimate strength of a corroded element (Castel et al. 2000).

Vu and Stewart (2000) have examined the effect of concrete cover spalling on structural strength. Experimental results from Vu and Stewart (2000) have shown that cover spalling leads to a reduced concrete compression zone and thus reduces flexural capacity. Additionally, the shear capacity is decreased because of the loss of section depth caused by the spalling concrete cover. Again, the work done by Vu and Stewart (2000) neglected the reduction in bond strength.

The time-dependent effect of corrosion on structural strength is another important factor. Almusallam et al. (1996) noted that a slight increase in the ultimate strength is observed when a small amount of corrosion occurs; however, further corrosion results in a sharp decrease in strength. It also showed that the flexural strength decreases progressively with an increasing degree of corrosion (Almusallam et al. 1996).

Because this research is only concerned with the effects of corrosion after the process has propagated to a severe state, the time dependent effects of corrosion will not be considered in this work.

Enright and Frangopol (1998) considered the time variant loss of strength due to corrosion of steel rebar, and found that a decrease of 17% of the rebar diameter in a #11 rebar is expected over 80 years. In contrast, Choe et al. (2007a) reported a reduction of approximately 3% in the mean diameter of the reinforcing steel in the columns over 100 years, but the maximum rebar diameter reduction between the upper and lower bounds of the confindence interval over the same time period is approximately 7%.

The differences in expected bar deterioration between Choe et al. (2007a) and Enright and Frangopol (1998) are explained by the different causes of the corrosion that are assumed in each work. Because this research is closely related to the bridge model represented in Choe et al. (2007a), a bar diameter reduction value of 10% is chosen to account for the effects of corrosion for the lifetime of the structure.

2.2 Stiffness

Stiffness is another important quantity used to measure structural integrity; therefore, it is necessary to examine the effect of corrosion on structural stiffness. In fact, one previous study has shown that stiffness actually decreases faster than strength as a result of the onset of corrosion (Li 2003b). Specifically, one example showed that a decrease in stiffness of 40% from the original state occurred over the same time as only a 10% decrease in strength (Li 2003b). While stiffness is important to the behavior of corroded

RC structures, there has not been nearly as much work done in this area as compared to the strength.

Castel et al. (2000) studied the effect of corrosion on both strength and stiffness, and the results show that corrosion in rebars in the tension region can have a significant impact on the service behavior of a structure. Additionally, information related to the reliability effects of corrosion induced stiffness deterioration can be found in Li et al. (2003).

2.3 Historic Preservation

Corrosion is a widespread issue, and it affects many historic structures annually throughout the country. In fact, many older RC structures are at higher risk for corrosion because of their greater time of exposure to corroding elements, such as de-icing salts or saltwater along a coastline. Many examples of historic bridges or buildings subject to corrosion and the possibility of seismic loading exist throughout the country. This research will help engineers understand the current condition of damaged structures to ensure that the proper treatment is administered. The designation of a bridge as "historic" adds to the complexity of the project, in that the historic appearance and character of the structure should be retained to the highest degree possible.

One example of an historic structure damaged by corrosion is a 1915 reinforced concrete, double-tiered trafficway viaduct in Kansas City, Missouri, and a case study of this structure is given in *Structure* magazine (Ball 2007). Although Kansas City is not located in a notoriously high seismic region, the corrosion problem itself was enough to

warrant a major restoration effort. The viaduct article references how exposure to chloride ions has caused reduced steel cross-sectional areas and concrete cover spalling. While the specific details of rehabilitative and restorative techniques is beyond the scope of this research, this article promotes the use of one specific rehabilitation method to passivate the active corrosion and extend the service life of the structure while maintaining its historic qualities (Ball 2007).

To emphasize the importance of aging infrastructure, work done by Stewart and Rosowsky (2001) noted that over 350,000 concrete bridges exist in the United States, and the rate of structural deterioration of these bridges seems to be increasing. Additionally, the Federal Highway Administration (FHWA) has created a National Bridge Inventory System in order to monitor the level of deterioration of bridges in the United States, and this inventory has been used to estimate that 150-200 bridges suffer either full or partial collapses each year. It also estimated that roughly 45% of bridges are currently structurally deficient and an estimated $90 billion is necessary to fix this problem (Stewart and Rosowsky 2001). Frequently, the cost to repair corrosion-related damage to existing structures can be approximately 25% of the original construction cost (Stewart and Rosowsky 2001). Additionally, many older bridges have garnered historic designations which increase the cost to protect them. An increasing number of these historic bridges are considered structurally deficient each year, and work must be done to ensure the protection and safety of these structures.

There has also been research performed with the goal of predicting the condition of an existing structure without physically performing on-site inspections. One such

example of a model with that purpose has been given by Malioka and Faber (2004). This work attempted to model the spatial variability of corrosion initiation and propagation so that the structural and serviceability performance can be predicted (Malioka and Faber 2004). This work is applicable to cases where it is not feasible or economically efficient to collect on-site data; however, this research assumes that enough on-site data is obtained to understand the degree of corrosion. The results of this work suggest a more cost-effective approach to analyzing the condition of historic structures.

One study which can be used for life-cycle or service-life analyses has been provided by Choe et al. (2007a). This work developed probabilistic drift and shear force capacity models for corroding RC columns in order to estimate the fragility (probability of failure) of deteriorated structural components. This work can be applied to either new or existing structures (such as historic structures) that are subjected to future or current deterioration.

Another study related to condition assessment of existing structures has been performed by Malioka and Faber (2003), and it attempted to create a probabilistic method to quantify inspection results for RC structures. The method would help determine the current condition, the predicted deterioration in the future, the expected service life remaining, and the estimated service life costs for the structure (Malioka and Faber 2003). This work would be ideal for historic structures because of the prediction of the remaining service life length and cost estimates. This method would also help eliminate the subjective nature of personal inspections and ensure that future recommendations are made in a systematic manner (Malioka and Faber 2003).

More motivation for this research comes from the fact that over 50% of bridges in the United States are over 50 years old; this means that many bridges around the country qualify for placement on the National Register of Historic Places (Stewart and Rosowsky 1998). Because the rate of deterioration increases as a structure ages, many reasons exist for why it is important to be able to adequately assess the current condition of an existing structure (Stewart and Rosowsky 1998). Many probabilistic models, like the one proposed by Stewart and Rosowsky (1998), account for uncertainties in material properties, geometric dimensions, environmental conditions, and inspection data.

Most research focused on condition assessment of existing structures can be directly applied to historic structures. However, the structural engineer should always be sure to give adequate consideration to the historic fabric of a structure before committing to any structural rehabilitation approach.

3. MODEL CREATION

To evaluate the effects of corrosion on the seismic response of a bridge structure, an accurate computer model must be created. A single-bent bridge, designed based on typical California guidelines, is used for this work in order to facilitate the comparison between the results of this work and those of previous studies (Choe et al. 2008; Mackie and Stojadinović 2003). The OpenSees (Open System for Earthquake Engineering Simulation) software created by the University of California, Berkeley is used to build a finite element model of the RC bridge. OpenSees is an open-source code, finite element software program which has been developed to foster computer modeling in the field of earthquake engineering and is capable of modeling nonlinear systems with many different materials and element types (OpenSees Computer Software 2008). Information about the bridge dimensions, material properties, earthquake records, and corrosion analysis cases is presented within this section.

3.1 Bridge Layout and Modeling

A three-dimensional, single-bent bridge (shown in Fig. 1) is used in this research with a circular column cross-section and a single pile shaft foundation; both the column and pile have identical cross-sections along their lengths. The deck spans to the abutments (not shown in the figure) on both sides of the column are the same length. The abutment and pile stiffnesses are modeled with springs in multiple directions.

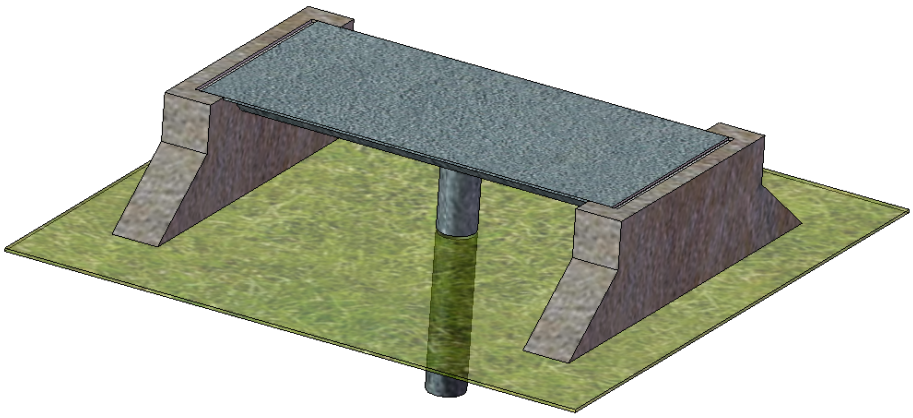

Fig. 1. Bridge Schematic

Fig. 2 shows a simplified version of the OpenSees model that is used. The x-direction is referred to as the longitudinal direction, the y-direction is transverse, and the z-direction is vertical. There are six degrees of freedom for each node in the model: translation and rotation in the global x, y, and z directions.

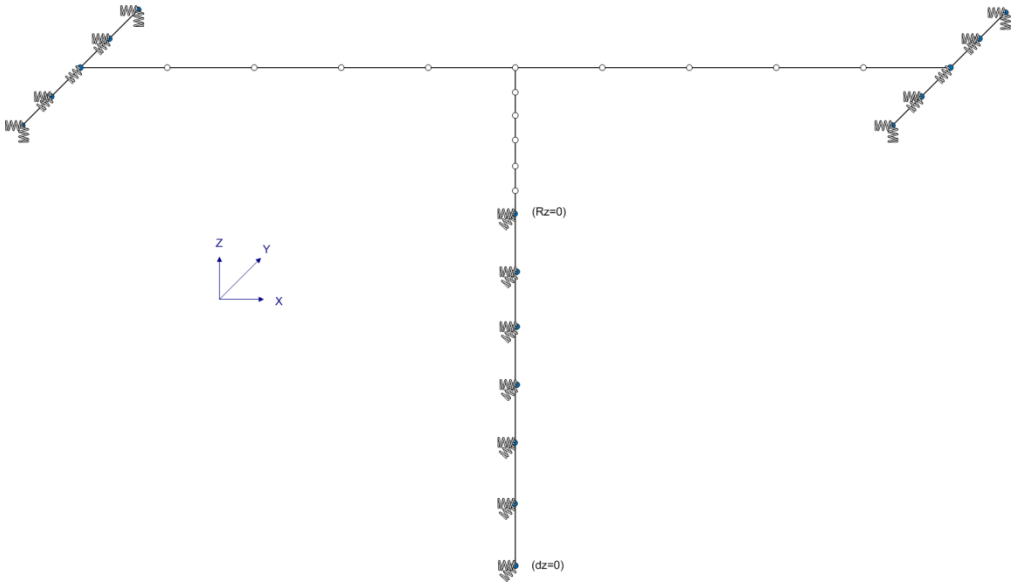

Fig. 2. OpenSees Bridge Model Representation

As seen in Fig. 2, the pile, column, deck, and abutments are all subdivided into separate elements for the bridge model. The column and pile elements are modeled as nonlinear beam-column elements while the deck and the abutments are modeled as elastic beam-column elements. The bridge dimensions are chosen to be comparable with work performed by Choe et al. (2008) and are given in Table 1. The cover thickness presented in Table 1 represents the clear cover from the outer surface of the concrete to the edge of the transverse steel.

Table 1. Bridge Dimensions

Property	Value
Deck Length	120 ft
Deck Thickness	84 in
Abutment Length	36 ft
Column Height	25 ft
Pile Height	44 ft
Column Diameter	63 in
Cover Thickness	3.0 in

The nonlinear beam-column elements used to model the bridge column and pile are force-based elements with distributed plasticity and five integration points along their length. The column and pile are each subdivided into six elements of equal length. Each element is developed using fiber-discretized, circular cross-sections containing three different materials: reinforcing steel, unconfined concrete cover, and confined core concrete. More detail on the material properties is given in Section 3.2.

The elastic beam-column elements used for the deck and the abutments are defined by simply providing values for the material properties of each element. The deck

is subdivided into ten equal elements, and each abutment is subdivided into four equal elements.

The gravity loads applied to the structure include the self weight of all members as well as an additional 10% of the self weight of the deck. This additional weight is added to the bridge deck to account for any superimposed dead loads which may be found on the structure, and it helps slightly increase the susceptibility of the column to nonlinear geometric effects (Mackie and Stojadinović 2003).

3.2 Material Properties

The materials used for each element in the given bridge model are explained in this section. Table 2 shows the most general material properties which are assumed throughout the entire bridge. The longitudinal steel modeled in the column and pile are #11 bars with a cross-sectional area of 1.41 in^2 and the transverse steel is modeled as #6 bars with a cross-sectional area of 0.75 in^2.

Table 2. Bridge Material Properties

Property	Value
f_y	65 ksi
$f_c^{'}$	4 ksi
ρ_{long}	0.02
ρ_{trans}	0.007

3.2.1 Column

The concrete core, concrete cover, and steel reinforcement used to create the column fiber sections are all defined with separate material properties, and the final section is also given a torsional rigidity of $GJ_c = 2.32*10^9$ k-in^2. The bottom node of the column is restrained from rotating around the global z-axis (torsion); however, all other column nodes are free to move in any of the six degrees of freedom (Mackie and Stojadinović 2003). The mass assigned to each node of the column is 0.035 k-s^2/in based on the self weight of the tributary area of the node.

A representation of the circular fiber elements defined within OpenSees is shown in Fig. 3. The fiber section is composed of 96 radial divisions in the concrete core and 24 radial divisions in the concrete cover; there are 36 divisions in the theta direction for both the core and cover. The number of fibers defined in the radial direction corresponds directly with Mackie and Stojadinović (2003).

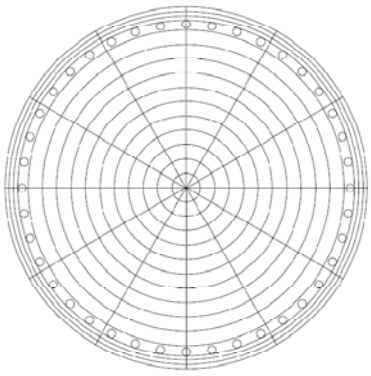

Fig. 3. Fiber Cross-Section

The concrete cover is defined using the Concrete01 material within OpenSees which assumes that the concrete material has no tensile strength. Table 3 shows the material properties for the unconfined, cover concrete,

Table 3. Concrete Cover Material Properties

Property	Value
$f_c^{'}$	4 ksi
$f_{cu}^{'}$	0 ksi
ε_c	0.002
ε_{cu}	0.005

where $f_c^{'}$ is the unconfined concrete compressive strength, $f_{cu}^{'}$ is the unconfined concrete crushing strength, ε_c is the concrete strain at maximum strength, and ε_{cu} is the concrete strain at ultimate strength. The values used for the cover concrete properties are commonly accepted values for unconfined concrete.

The concrete core is defined using the Concrete01 material and the confined concrete model proposed by Mander et al. (1988). The material properties used for this model are given in Table 4,

Table 4. Concrete Core Material Properties

Property	Value
$f_{cc}^{'}$	5.35 ksi
$f_{ccu}^{'}$	4.22 ksi
ε_{cc}	0.00537
ε_{ccu}	0.0197

where f'_{cc} is the confined compressive strength, f'_{ccu} is the confined concrete crushing strength, ε_{cc} is the confined concrete strain at maximum strength, and ε_{ccu} is the confined concrete strain at ultimate strength. The confined concrete compressive strength used to model the core is determined using the following equation,

$$f'_{cc} = f'_c\left(2.254\sqrt{1+\frac{7.94\,f'_l}{f'_c}}-2\frac{f'_l}{f'_c}-1.254\right) \quad (1)$$

where f'_l is the effective lateral confining stress (Mander et al. 1988). The confined concrete ultimate strength and the confined concrete strains noted in Table 4 are also calculated following the procedure proposed by Mander et al. (1988).

The stress-strain curves for the cover (unconfined) and core (confined) concrete are shown in Fig. 4 (where compression is negative). The confined, core concrete has a higher maximum compressive strength and reduces to a lower strength as the strain increases, representative of the strength of the confined core after the cover has spalled off. The unconfined cover concrete decreases to zero stress once the cover cracks and spalls because it can no longer carry any load.

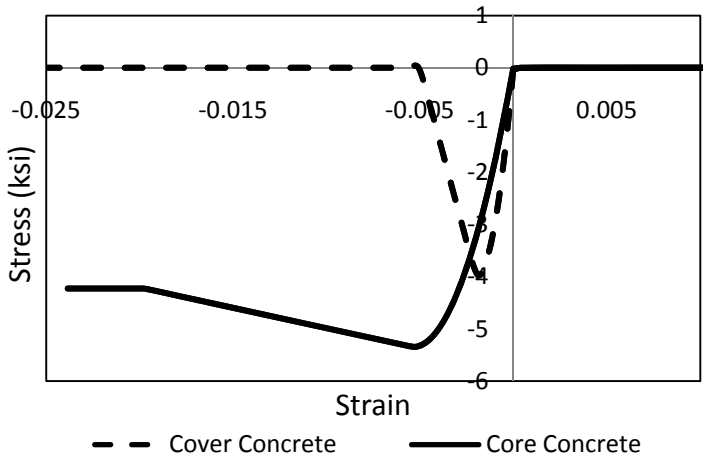

Fig. 4. Stress-Strain Relationship for Concrete Material

The steel reinforcement is defined using the Steel02 material within OpenSees which assumes linearly elastic behavior until the yield point is reached. Beyond yield, strain hardening is defined based on a ratio between the post-yield tangent and the initial elastic tangent stiffnesses. Table 5 gives the material properties for the reinforcing steel used in the column,

Table 5. Concrete Material Properties

Property	Value
f_y	65 ksi
E	29,000 ksi
B_s	0.01

where f_y is the yield strength, E is the initial elastic tangent, and B_s is the strain hardening ratio. The material properties for the reinforcing steel are assumed to be the

same in both tension and compression, and Fig. 5 shows the stress-strain diagram of the steel.

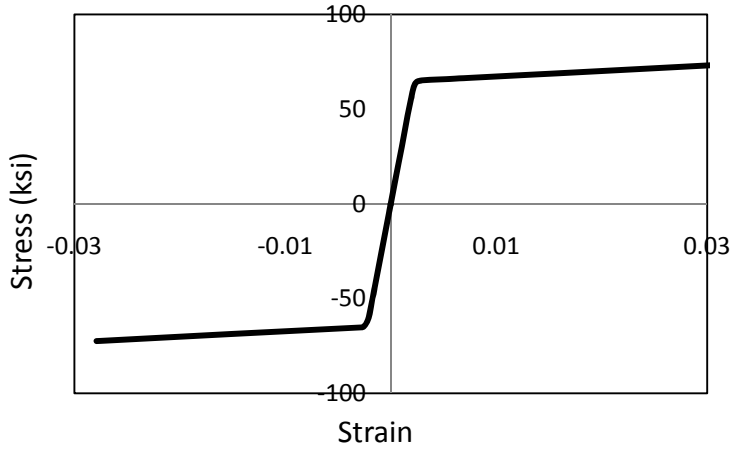

Fig. 5. Stress-Strain Relationship for Reinforcing Steel Material

3.2.2 Pile

The material properties for the pile are identical to those used for the fiber section in the column elements, and it is assumed that the longitudinal reinforcement from the column is continuous into the pile. However, unlike the column, the bottom node of the pile is restrained from translating in the vertical direction (Mackie and Stojadinović 2003). The mass assigned to each node of the pile is 0.061 k-s^2/in.

Additionally, every node along the length of the pile is restrained in the longitudinal and transverse directions with nonlinear springs to represent the effect of the soil. Only USGS soil group B is represented in this research, and the development of the spring stiffnesses follows the procedure set forth in Mackie and Stojadinović (2003).

Seven P-y springs are used to represent the soil along the depth of the pile, and the spring stiffnesses are equal in both the longitudinal and transverse directions at a given pile depth. The ultimate load bearing capacity for each spring is determined using the following equation, shown in Mackie and Stojadinović (2003),

$$p_u = \min \begin{Bmatrix} (C_1 x + C_2 D)\gamma' x \\ C_3 D \gamma' x \end{Bmatrix} \tag{2}$$

where C_1, C_2, and C_3 are constants obtained from API (1993), D is the average pile diameter, γ' is the effective soil weight, and x is the depth below grade. The spring load-deflection behavior is then determined with the following relationship,

$$P = Ap_u \tanh\left(\frac{kx}{Ap_u} y\right) \tag{3}$$

where A is a constant for cyclic loading, k is the initial modulus of the subgrade reaction found from API (1993), and y is the lateral deflection. Table 6 shows the values used for each P-y spring property in the OpenSees model.

Table 6. Soil P-y Spring Properties

Property	Value
C_1	4.65
C_2	4.35
C_3	100
k	446 lb/in^3
A	0.9
ϕ'	39^o
γ'	137 pcf

3.2.3 Deck

The elastic beam-column elements used to model the deck are defined by the material properties given in Table 7. There are rigid connections between the deck and the column and between the deck and the abutments. The deck properties shown in Table 7 are given by Mackie and Stojadinović (2003) for a typical concrete, box girder deck with a width of 36 ft. The mass assigned to each of the inner nodes of the deck is 0.319 k-s^2/in; the mass assigned to each of the two outer deck nodes (near the abutments) is 0.159 k-s^2/in. These masses are calculated based on the self-weight of the tributary area of each node along the deck.

Table 7. Deck Material Properties

Property	Value
A	8,960 in^2
E	3,605 ksi
G	1,502 ksi
J	7,755,150 in^4
I_y	7,724,363 in^4
I_z	123,533,760 in^4

3.2.4 Abutments

The abutment stiffness and strength properties used for this model have been proposed by Caltrans and presented by Mackie and Stojadinović (2003). The elements used for the abutments are defined as rigid links used only to transfer the effect of the abutment

springs along the width of the deck. Table 8 shows the material properties assigned to the abutments. There are no nodal masses assigned to the abutments.

Table 8. Abutment Material Properties

Property	Value
A	9,000,000 in^2
E	9,000,000 ksi
G	9,000,000 ksi
J	9,000,000,000 in^4
I_y	9,000,000,000 in^4
I_z	9,000,000,000 in^4

Each abutment has four elements and five nodes; there is a total of nine springs along each abutment which account for the bearing pads, the longitudinal abutment stiffness, the transverse abutment stiffness, and/or the vertical abutment stiffness. To stay consistent with the model used by Mackie and Stojadinović (2003), seat-type abutments are modeled with a gap of 6 inches in the longitudinal direction. The deck rests on two elastomeric bearing pads at each end (two nodes), and these pads are modeled using springs with elastic-perfectly-plastic behavior in both the longitudinal and transverse directions. Thus, the bearing pads account for four springs along each abutment. Two vertical springs are also modeled for each abutment to resist vertical motion. One spring is applied to the model to account for the transverse abutment stiffness; this spring is modeled with elastic-perfectly-plastic behavior and zero gap. The last two springs modeled along each abutment account for the longitudinal abutment stiffness. There is a gap of 6 inches in the longitudinal direction; therefore, these springs

are not activated until they have been compressed by 6 inches (i.e. the gap has been closed). Once the gap has been closed, the longitudinal springs have elastic-perfectly-plastic behavior as well. All springs are activated only when in compression; none of the springs are active in tension. The values used for the abutment spring stiffnesses are obtained by Mackie and Stojadinović (2003) and are shown in Table 9.

Table 9. Abutment Spring Stiffnesses

Type of Spring	Spring Stiffness
Bearing Pads	10 k/in
Vertical Restraint	2,315 k/in
Transverse Gap Element	627 k/in
Longitudinal Gap Element	1,107.5 k/in

3.3 Earthquake Records

To be able to perform a seismic dynamic analysis on the given bridge, a suite of earthquakes which constitutes a representative sample of expected seismic activity for the bridge is developed. For this research, the bin method proposed by Shome (1999) is used. This method involves creating five separate, imaginary bins based on the moment magnitude (M) and the closest distance to the rupture zone (R) of the earthquake. The five bins used are:

(1) SMSR – Small Magnitude, Short Range: M = [5.5,6.5]; R = [15km, 30km]

(2) SMLR – Small Magnitude, Long Range: M = [5.5,6.5]; R = [30km, 50km]

(3) LMSR – Large Magnitude, Short Range: M = [6.5,7.5]; R = [15km, 30km]

(4) LMLR – Large Magnitude, Long Range: M = [6.5,7.5]; R = [30km, 50km]

(5) Near – Near field: M = [6.0,7.5]; R = [0km, 15km]

The first four bins, with R>15km, are considered 'ordinary' ground motions, and the fifth bin, with R<15km, is composed of 'near-field' ground motions (Shome 1999).

For this study, six earthquakes are chosen for each bin and are obtained from the Pacific Earthquake Engineering Research (PEER) Center Strong Motion Catalog online (PEER 2008). The six specific records chosen for each bin are directly obtained from previously developed bins, with 20 earthquakes each, in Huang et al. (2008). In order to ensure that the six earthquakes chosen for each bin are representative of all earthquakes in that bin, the median spectral acceleration values for each bin are compared against the corresponding spectra determined by the attenuation law developed by Abrahamson and Silva (1997). Fig. 6 shows a comparison of the median pseudo spectral acceleration (PSA) curves among the attenuation law, the 20 earthquake record bins, and the 6 earthquake record bins. As expected, the curves for 20 earthquakes and for 6 earthquakes are not as smooth as the attenuation law; however, the general shapes are comparable.

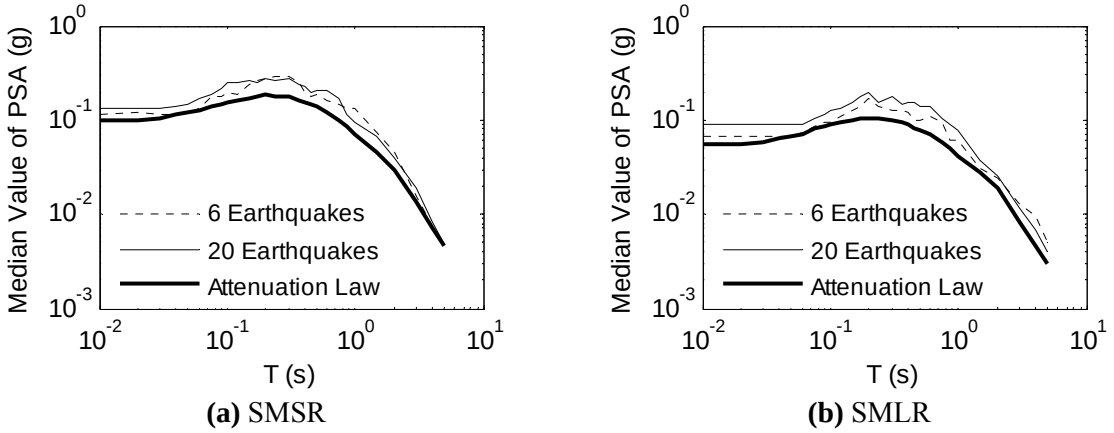

(a) SMSR **(b)** SMLR

Fig. 6. Median Acceleration Spectra Comparisons

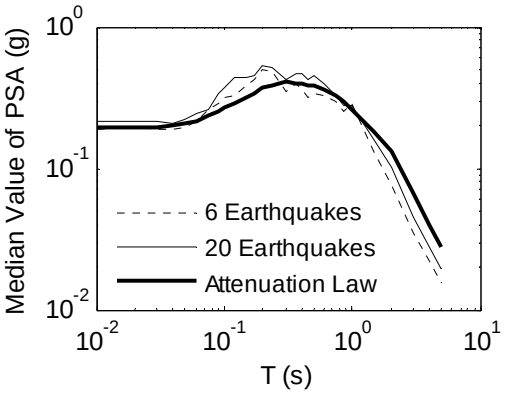

(c) LMSR

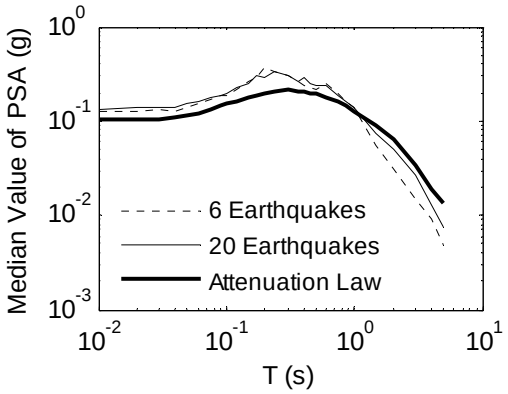

(d) LMLR

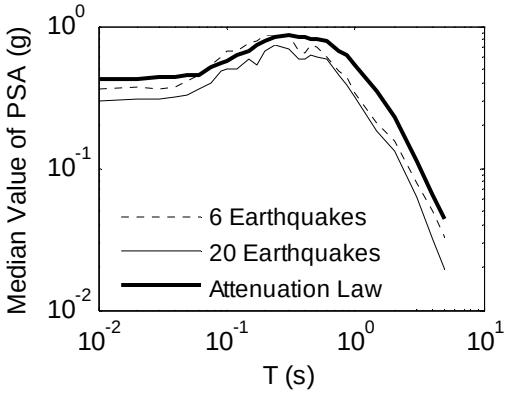

(e) Near

Fig. 6. Continued

The standard deviations of the spectral accelerations for each bin are also compared against the expected attenuation law results, and a visual comparison is made. Based on previous work performed by Shome (1999) and Huang et al. (2008), the maximum difference in the standard deviation between the median records in each bin and the corresponding attenuation law results is kept below a value of 0.2. More specific details regarding the method used to determine the final six earthquakes for each bin can be seen in APPENDIX B.

Ten additional bins are created by simply scaling the records in the previous five bins by certain determined constants. The reason for scaling the earthquake bins is to be able to study more inelastic behavior in the bridge under seismic loads, and the method used to determine the appropriate scale factors is based on the work done by Luco (2001). This work states that an appropriate scale factor results in the mean and the "one sigma level" values of the spectral displacement plots being similar between the average of the ordinary bins and the near-field bin. The first set of scaled up records uses a scaling factor of six for the ordinary bins and a factor of two for the near field bins; the second set of scaled records uses a factor of eleven for the ordinary bins and four for the near field bins. More detail on the development of these scale factors can be found in APPENDIX B. All earthquake records used in this model are applied in three orthogonal directions, and the two horizontal components are randomly assigned to the lateral and transverse directions of the bridge for each earthquake. More details about each earthquake record used in this analysis can be found in APPENDIX B as well.

3.4 Analysis Cases

The OpenSees model is used to analyze four cases which represent the extreme damage cases related to corrosion of the rebar and spalling of the concrete cover. The first case considers no damage; therefore, the full concrete cover thickness and full rebar diameters are assumed for the bridge column. This case is denoted as FCFB (full concrete cover, full rebar diameters), and it is considered to be a pristine structure. The second case assumes that rebar corrosion has occurred, but the full concrete cover thickness is still present. This case would be applicable in existing structures if the

concrete cover has not yet spalled off or if the cover has been replaced back to its original thickness using an unspecified retrofitting technique. This case is referred to as FCPB (full concrete cover, partial rebar diameters). The third case accounts for no decrease in rebar diameters because of corrosion; however, the entire concrete cover is assumed to have spalled off. The third case is denoted by NCFB (no concrete cover, full rebar diameters), and it can be seen in existing structures that are subject to concrete cover deterioration unrelated to corrosion. The fourth case considered in this study assumes that the entire cover has spalled off and all rebar diameters have been decreased. The last case is referred to as NCPB (no concrete cover, partial rebar diameters), and this is seen in existing structures when corrosion of the rebar produces rust products that cause the cover concrete to experience tension cracking and spalling.

A constant reduction of 10% of the rebar diameter is assumed for both the FCPB and NCPB cases; this value is chosen based on the results of Choe et al. (2007a) which show the likely decrease in rebar diameter caused by corrosion propagation over the lifetime of the proposed bridge. For this level of bar reduction, the corrosion is dominated by a chloride-induced exposure condition of the bridge column: in other words, the column is assumed to be partially submerged in seawater for 100 years (Choe et al. 2007a). The work done by Choe et al. (2007a) shows that the expected decrease in the mean area of longitudinal reinforcement over 100 years is about 5%; however, to account for the differences between the upper and lower bounds of the confidence band, a value of 10% is chosen.

4. MODEL VALIDATION

Before actually using the model of the given bridge to obtain any results, the accuracy of the model output must be verified. First, the strength and stiffness values and the relative changes in those values for the four cases (FCFB, FCPB, NCFB, and NCPB) are checked. Secondly, the static pushover curves from OpenSees are compared with those from additional analysis programs. Additionally, the fundamental periods and mode shapes are checked using various methods of modal analysis. The damping ratio is also verified with two different methods using the dynamic response data created within OpenSees. The end of this section presents some of the limitations of this model.

For most model verification purposes, the axial load applied to the column due to its own self-weight is assumed to be 80 kips; although, the gravity load for the column alone actually ranges from 66.5 to 81.1 kips depending on the amount of concrete cover that has spalled off. Some model verification analyses are also run with scalar multiples of the gravity load in order to compare the software results under more substantial axial loads in the column.

4.1 Strength and Stiffness

The accuracy of the strength and stiffness values obtained from the static pushover results is verified using hand calculations with assistance from software programs such as Matlab and PCA Column.

In order to verify the stiffness values reported by OpenSees, Matlab is used to perform a bilinear analysis on the OpenSees pushover data obtained for a column with

roller abutment supports (no abutment stiffnesses). The ratios of the full bridge stiffness with and without corrosion effects obtained from the Matlab bilinear analysis are compared with those obtained from hand calculations. The corrosion effects accounted for at this stage are a removal of 3 inches of concrete cover along with 10% of the longitudinal rebar diameters in the column. The decrease in rebar diameter is assumed to have a negligible effect on the stiffness due to its insignificant contribution to the moment of inertia of the column cross-section. However, the reduction in the column diameter as a result of removing the concrete cover has a much more significant effect on the stiffness.

The stiffness comparison used for the hand calculations is performed by evaluating the ratio of the moment of inertia of the concrete in the column with the cover removed to the moment of inertia of the concrete in the full column; this value is determined to be 0.67. This ratio can also be compared with the results of the Matlab bilinear analyses. The ratio of the bilinear stiffness of the NCFB case to that of the FCFB case is 0.75 while the stiffness ratio between the NCPB and the FCPB cases is 0.72. Fig. 7 shows the relationship between the base column shear and the lateral drift for the longitudinal direction; it is clear that the FCFB case has a greater stiffness than the other cases.

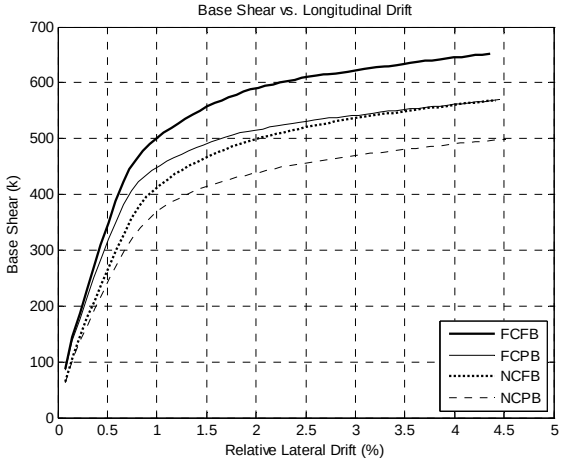

Fig. 7. OpenSees Pushover Results

The previous stiffness ratios indicate that removing 3 inches of concrete cover for a column with a 63-inch diameter decreases the stiffness by approximately 27%. Thus, the change in stiffness obtained from the OpenSees analysis is verified. APPENDIX C has more detailed information and calculations for the stiffness verification process.

Approximate hand calculations are also done to compare the differences in strength between the four cases for corrosion (FCFB, FCPB, NCFB, and NCPB). It is important to note that a reduction of 10% of the rebar diameter corresponds to a decrease in the rebar area of approximately 20%. Based on the direct relationship assumed between the concrete strength and the rebar area in the ACI Code (ACI 2008), the strength is expected to be decreased by approximately 20%. The decrease in concrete cover is not assumed to have a significant effect on the overall strength. From the pushover results obtained from OpenSees, the decrease in strength at 4.5% relative drift

between the FCFB and FCPB cases is approximately 14% while the decrease in strength between the NCFB and NCPB cases at the same level of drift is approximately 13%. The calculations to support these values can be found in APPENDIX C. The OpenSees results are close to the expected strength reduction from the hand calculations; therefore, the OpenSees results are confirmed.

In addition to the hand calculations, an axial load – moment interaction diagram developed with the commercial software, PCA Column, is used to help verify the section capacity results reported in OpenSees. PCA Column does not account for concrete confinement or strain hardening in the rebar; these are two things that the OpenSees program considers in its analysis. More information about the PCA Column model can be found in APPENDIX D.

Based on the interaction diagram developed in PCA Column, the values for the cracking moment (M_{cr}), the yield moment (M_y), the ultimate moment (M_{ult}), the yield curvature (ϕ_y), and the ultimate curvature (ϕ_{ult}) could be determined for any value of axial load. These values are calculated for the axial load values of 80 kips and 800 kips and are shown in Table 10. An axial load of 80 kips is used because it is the approximate self weight of the column alone, and an axial load of 800 kips is an easy multiple of the self weight used to help validate the P-Δ effects (in a future section). APPENDIX D shows the assumptions made when calculating these values.

Table 10. Material Section Properties

	Axial Load	
Property	80 kips	800 kips
M_{cr}	33,780 k-in	39,000 k-in
M_{y}	67,560 k-in	78,000 k-in
M_{ult}	97,800 k-in	108,000 k-in
ϕ_{y}	0.000052 (1/in)	0.0000599 (1/in)
ϕ_{ult}	0.000827 (1/in)	0.000829 (1/in)

As the interaction diagram shows, the maximum axial compressive capacity of this column is around 14,000 kips. Clearly, the axial load capacity of this column is much greater than the demand from the self-weight of a single column. For the OpenSees full bridge model where the deck loads are incorporated, the axial load is increased significantly; although, the total axial load still does not approach the capacity given by PCA Column.

A section analysis is also performed in OpenSees to obtain the moment-curvature diagram for the column fiber cross-section. The moment-curvature relationships for all four cases are shown in Fig. 8.

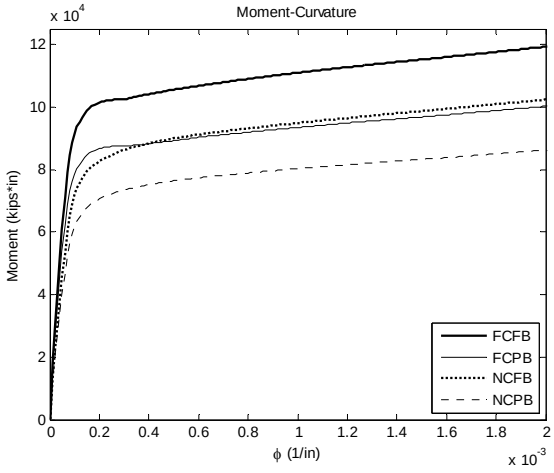

Fig. 8. OpenSees Moment-Curvature Results

The important moment and curvature values for the FCFB case are shown in Table 11 for the case when the axial load is equal to the half of the self weight of the deck plus half of the self weight of the column. This axial load value, calculated within OpenSees, is found to be 656.5 kips. For a direct comparison with the PCA Column data, Table 11 shows the moment and curvature values that correspond with those given in Table 10.

Table 11. OpenSees Moment-Curvature Results (FCFB)

Property	80 kips	800 kips
M_{cr}	41,273 k-in	43,261 k-in
M_{y}	82,545 k-in	86,521 k-in
M_{ult}	108,373 k-in	115,763 k-in
ϕ_{y}	0.000141 (1/in)	0.000096 (1/in)
ϕ_{ult}	0.001600 (1/in)	0.001300 (1/in)

The moment and curvature values found using OpenSees (Table 11) are all slightly higher than those found using PCA Column (Table 10). The reason for these differences is because different assumptions are used when calculating the yield and ultimate curvature values. More detail on this topic can be seen in APPENDIX D.

4.2 Validation of Static Pushover

In addition to the strength and stiffness verifications made using the static pushover results, second order p-delta (P-Δ) effects and the general shape of the pushover curves are checked. The pushover analysis performed in OpenSees is a displacement controlled analysis, and the pushover force is applied at the top node of the column.

One program that is used to help verify the OpenSees results is a program called 'Inelastic Damage Analysis of Structural Systems,' or IDASS (Kunnath 2003). Two comparison studies are performed between OpenSees and IDASS for a single RC column (no pile, deck, or abutments): one with an 80 kip axial load and one with an 800 kip axial load. For each axial load case, two analyses are performed: the first analysis accounts for second order P-Δ effects while the second analysis neglects P-Δ effects. For more information regarding the modeling differences between IDASS and OpenSees, refer to APPENDIX E.

Fig. 9 shows the results from IDASS and OpenSees for the 80 kip axial load. The IDASS results show a decrease in base shear of 4.8 kips between the linear and P-Δ cases at 6% drift while the OpenSees results show a difference of less than 1 kip between the linear and P-Δ results for the same scenario.

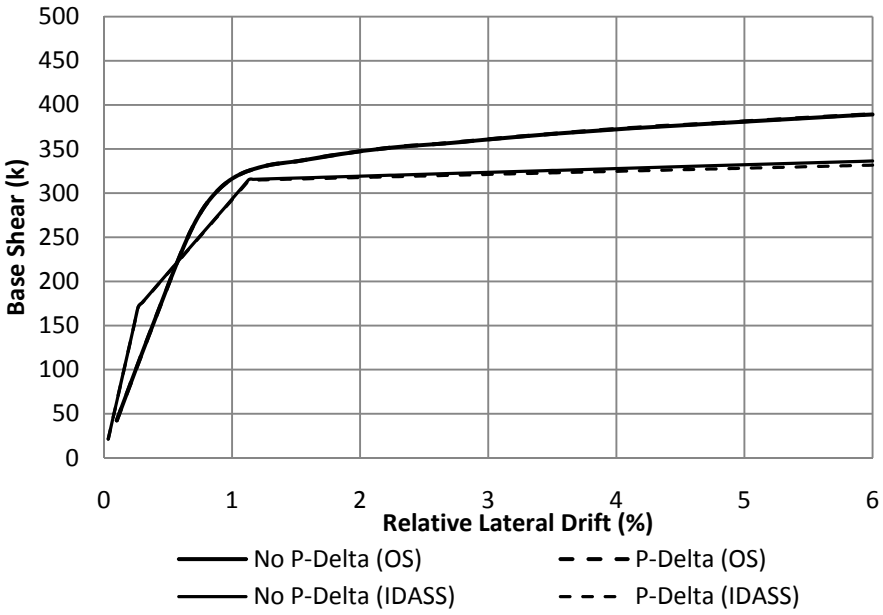

Fig. 9. Pushover Comparison (80k)

It can be seen in Fig. 9 that the IDASS model begins to yield near the same level of drift as the OpenSees model; however, the strength is slightly greater in the OpenSees model. Additionally, the IDASS model shows a defined change in stiffness at the point where the concrete cracks, but the OpenSees results do not show this. For the IDASS model, it is assumed that the cracking moment is exactly half of the yield moment. Fig. 10 shows similar results for the 800 kip axial load case. As expected, the higher axial load increases the P-Δ effect; however, the IDASS model still shows a much higher decrease in maximum base shear than the OpenSees model.

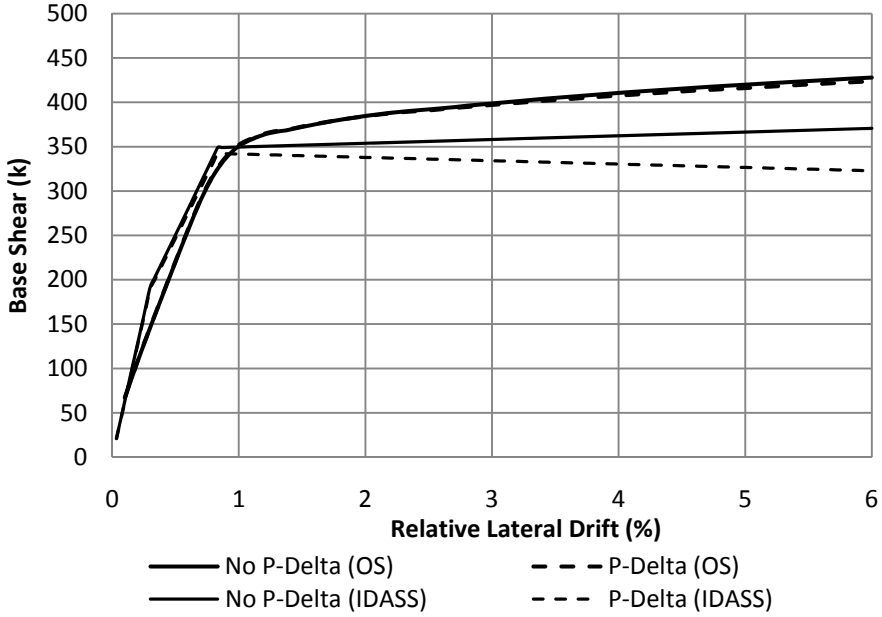

Fig. 10. Pushover Comparison (800k)

The reason why the pushover results from IDASS show a more drastic difference in the results when the P-Δ effects are accounted for is because of the difference in defining the Δ value. The Δ value in IDASS is defined to the centroid of the column cross-section while the Δ value within OpenSees is defined to the neutral axis of the cross-section. Since the neutral axis of the fiber cross-section within OpenSees is constantly shifting during the static pushover analysis, this Δ value is less than the one assumed within IDASS.

A second program used to validate the pushover results for the single column obtained from OpenSees is USC_RC (Esmaeily 2001). This program is used to verify the general shape of the pushover curve for the 800 kip axial load; it does not include the

option of accounting for or neglecting P-Δ effects. More information on this program can be found in APPENDIX E as well.

As shown in Fig. 11, the shape of the USC_RC pushover curve is very similar to the OpenSees results. The slight bump shown in the USC_RC results is not seen in the OpenSees data because the reinforcing steel material models are slightly different.

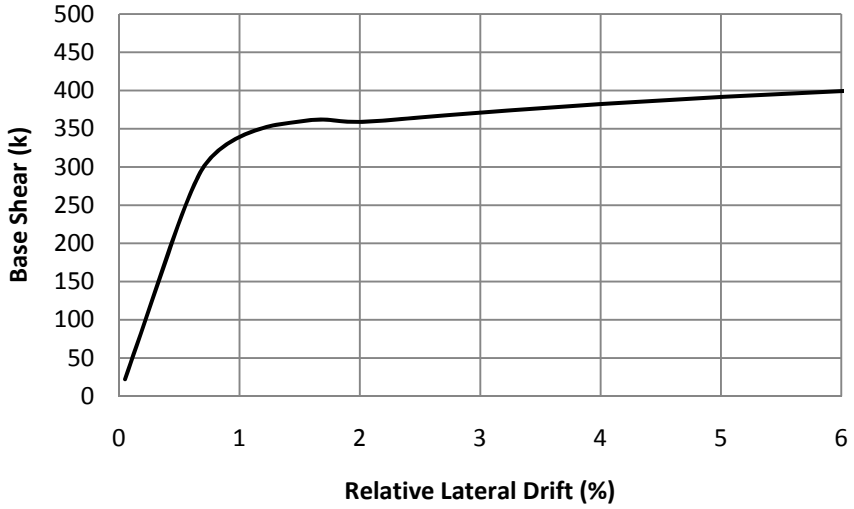

Fig. 11. USC_RC Pushover Curve (800k)

Overall, the static pushover results from the OpenSees model are comparable to those obtained using IDASS and USC_RC. There are slight variations in all three models which prevent them from providing identical results; however, since they all seem relatively close, the OpenSees static pushover results seem to be correct for this model.

One unique issue encountered with the OpenSees fiber model is the fact that that during the static pushover analysis of the full bridge with the abutment stiffnesses added, the top node of the column displaced vertically upward, causing a steady increase in the axial load in the column from approximately 800 kips to 1,300 kips. The best explanation for this behavior is made by examining the stresses at the center of the fiber section, the point where the nodal displacement is recorded. Upon further analysis, it is determined that throughout the entire pushover analysis, the center of the cross-section remains in tension. Since the section rotates about its neutral axis during the pushover analysis, all points in tension are displaced upward while those in compression are displaced downward. Since the abutments restrict the top of the column from displacing downward at all, the rotation of the section moves the top node vertically upward, resulting in an increased axial load. This phenomenon is not seen in IDASS or in USC_RC.

4.3 Modal Analyses

While the pushover data is useful for verifying the static structural response, a series of modal analyses is performed to verify the dynamic properties of the OpenSees model. There are two main purposes for performing a modal analysis for the given bridge structure. First, a modal analysis helps to show how the structure will behave under dynamic loading. Typically it is important to understand the general behavior of a structure so that it can be designed to avoid its fundamental frequencies. Secondly, the modal analysis is also important for finding the fundamental periods for the longitudinal and transverse directions; these values are used to find the expected displacement values

from specific earthquake response spectras. The spectral values are then compared with the maximum displacement values obtained with the OpenSees dynamic analysis to see how closely the spectra matched with the analytical model.

Several different procedures for obtaining the fundamental frequencies and periods for the longitudinal and transverse modes are performed to ensure that the values obtained are accurate. There are seven different methods used for the comparison study, and each method is explained in detail in APPENDIX F. Two different abutment types are also used in order to help check expected values. The first abutment type is a true roller support with restraint only in the vertical direction. The second abutment type is denoted as the Caltrans abutment, and it is restrained in the vertical, longitudinal, and transverse directions with springs to represent the stiffness of the abutment. More details about the Caltrans abutment can be found in Section 3.2. Lastly, it should be noted that only the FCFB case is used for the modal analysis comparisons shown in APPENDIX F; however, two final modal analyses are performed on all four bridge cases (FCFB, FCPB, NCFB, and NCPB) for the final bridge configuration.

In order to choose the most accurate values for the longitudinal and transverse periods to be used with the earthquake response spectral data, each of the methods given in APPENDIX F are compared. Table 12 shows a concise comparison of the periods for the longitudinal, transverse, and vertical displacement modes for the Caltrans abutment case found from each analysis method.

Table 12. Modal Analysis Period Comparison - Caltrans

Mode	OpenSees "eigen"	ETABS	Matlab FFT	Matlab TDD	OpenSees Pushover	Hand Calculations	PEER Report
Longitudinal	0.2982	-	0.6068	0.6023	0.4762	-	-
Transverse	0.1816	-	0.2979	0.3011	0.2011	-	-
Vertical	0.6061	-	0.0972	0.0975	0.0848	-	-

Table 13 shows a similar comparison of the periods for the roller abutment case. Note that the ETABS and hand calculations are only performed for the roller abutment case. The ETABS model also does not report a vertical displacement mode when the modal analysis is performed. The PEER Report (Mackie and Stojadinović 2003) also does not report a period for the vertical displacement mode.

Table 13. Modal Analysis Period Comparison - Roller

Mode	OpenSees "eigen"	ETABS	Matlab FFT	Matlab TDD	OpenSees Pushover	Hand Calculations	PEER Report
Longitudinal	0.0909	0.4509	0.6425	0.6399	0.5518	0.4500	0.5500
Transverse	0.6424	0.5561	0.7447	0.7313	0.6172	0.4500	0.6400
Vertical	1.6939	-	0.0900	0.0898	0.0848	0.0410	-

Based on the discussion and results presented in APPENDIX F, it is clear that the ETABS results are not very accurate for the Caltrans case due to modeling difficulties. The values obtained from the OpenSees "eigen" command leave much room for doubt based on the explained first mode presented. The results obtained from the OpenSees pushover curves can be debated based on the stiffnesses chosen for the first part of the bilinear analysis. In other words, the initial stiffnesses are approximate and are based on

the conditions used to develop the bilinear curve. The FFT and TDD analyses are both useful because they use response data obtained directly from OpenSees to determine the frequencies. Therefore, there are no errors introduced from building a new model. The hand calculations are relatively inaccurate due to the simplifying assumptions made; however, they do give good approximate values for the periods. The PEER report is also inaccurate for this bridge because the model used to obtain those periods is slightly different and not completely well defined (Mackie and Stojadinović 2003).

As a result of the modal analysis verification, a range of periods is chosen for analyzing the OpenSees model data. The OpenSees pushover results seem to give a relatively accurate lower bound on the expected periods while the Matlab FFT results give a fairly accurate upper bound. For all response spectra calculations and comparisons, the results will be presented using the Matlab FFT periods.

4.4 Damping Verification

One benefit of performing the Matlab FFT analysis is that the free vibration response data is also used to verify the level of damping in the structure. Two different methods are used to calculate the damping ratio: the logarithmic decrement method and the half-power bandwidth method. Both methods are performed to check damping ratio of the free vibration response data for the longitudinal direction with both the Caltrans and roller abutments. The equivalent viscous damping ratio input into the OpenSees model is 2%.

APPENDIX G presents more detailed information and exact calculations for determining the damping ratio. The results of the logarithmic decrement method verified

that the structure is experiencing 2% damping; the Caltrans case showed a damping ratio of 1.95% while the roller abutment case showed a damping ratio of 1.94%.

The second method used to verify the damping ratio is the half-power bandwidth method. This method requires that the response data be transformed into the frequency domain. This is easily done using the FFT procedure in Matlab, and more detail can be seen in APPENDIX G. Similar to the logarithmic decrement method, the half-power bandwidth method confirmed the damping ratio to be approximately 2%. The Caltrans case resulted in a damping ratio of 2.1% while the roller abutment case showed a damping ratio of 2.09%.

4.5 Limitations

Although this model is accurate enough to provide the comparison data that is desired for this research, the limitations of the OpenSees model must be clearly presented. First of all, the assumed 10% decrease in rebar diameter due to corrosion is based on the work performed by Choe et al. (2007a) for concrete specimens in a "splash zone" where there is high exposure to both salt water and oxygen. This is not the only type of corrosion that a RC structure could be exposed to, nor is it necessarily the most severe case of corrosion possible. Additionally, Choe et al. (2007a) assumed that the initiation time for corrosion is based on Fick's Second Law for chloride permeation through undamaged concrete; however, if the cover concrete is cracked then the corrosion initiation time could be significantly shorter than the time assumed. A significantly faster rate of corrosion and a greater decrease in rebar area over the lifespan of the structure might result.

Another limitation of this model is that it only accounts for extreme cases for the lifetime of the structure. The model does not account for the time-dependent effects of corrosion; instead, it just compares the pristine structure with the most severely damaged case (no concrete cover and reduced rebar diameters).

This model also assumes that the corrosion level is uniform from the bottom of the pile to the top of the column. Although, this is probably not the most likely case, it does yield conservative results. The model also neglects the effects of localized, or pitting, corrosion. Additionally, the given OpenSees model assumes that the full cover thickness spalls along the entire length of the column and the pile. Again, this is not completely realistic because real structures would most likely be repaired before the damage progresses to this state. However, this assumption does constitute a "worst case" scenario for comparison purposes.

Another assumption made in the OpenSees model is that the abutment springs do not degrade or sustain damage over time as a result of the cyclic loading. Especially in the longitudinal direction where the gap is set at six inches, it is assumed that the bridge does not hit the abutments (i.e. the gap is not closed) more than once or twice for each earthquake. Therefore, the effects of abutment damage are assumed to be negligible.

This research also assumes that the strength and stiffnesses losses due to corrosion are accounted for by modeling the decrease in rebar cross-sectional area and the decrease in concrete cover. It is assumed that the effect of the loss of bond between the concrete and steel is negligible; although, this may not be the case in all situations. The bond deterioration might result in a loss of strength as well as a more degrading

hysteretic behavior. Even though corrosion in the reinforcing steel occurs, the stress-strain behavior of the reinforcing steel is assumed to remain the same for both the pristine and the corroded specimens.

Additionally, this model is only directly applicable to single-bent, RC bridges subject to corrosion and seismic loads where the abutment stiffness is very significant in one direction. In this research, the transverse abutment stiffness is large enough in magnitude to help offset the increase in period expected by inducing damage in the column. If a bridge with multiple bents is analyzed, the transverse period is expected to be less dependent on the transverse abutment stiffness; therefore, a more significant difference between the undamaged and damaged columns in the transverse direction is expected.

Lastly, the results presented herein have been developed based on the behavior of one bridge with a representative sample of earthquake records for California. More certainty in the results would be expected if a suite of bridges with different geometric properties are analyzed for the same earthquake records.

While it is important to keep these limitations in mind, the results of this research can still be broadly applied to a variety of different structures subject to corrosion and other vibrational loadings. In further sections of this report, the results of this work will be related to additional, especially historic, structures.

5. ANALYSIS RESULTS

The results obtained from static and dynamic analyses of the RC bridge accounting for the spalled concrete cover and the decreased rebar diameter are presented herein. The seismic fragility is also developed and presented within this section.

5.1 Static Analysis

The effect of corrosion damage on the strength and stiffness of the bridge using a static analysis in OpenSees is given in this section. Two different types of static pushover curves are developed for the bridge in each direction. The first pushover curves show the relationship between the base shear in the column and the relative lateral drift between the top and bottom of the column. Fig. 12 (a) and (b) show these curves for the bridge in the longitudinal and transverse directions, respectively.

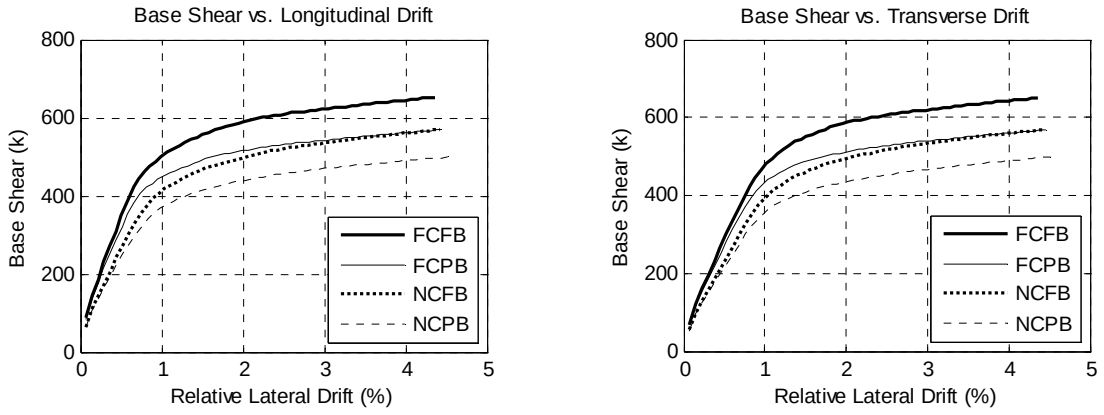

(a) Longitudinal Pushover (b) Transverse Pushover

Fig. 12. OpenSees Static Pushover Analysis Results (Column Base Shear)

The column shears are very similar in both directions; however, the static pushover relationship between the total pushover force and the relative lateral drift changes drastically to account for the different abutment stiffness values. The static pushover results in the longitudinal and transverse directions for the total pushover force are shown in Fig. 13 (a) and (b), respectively.

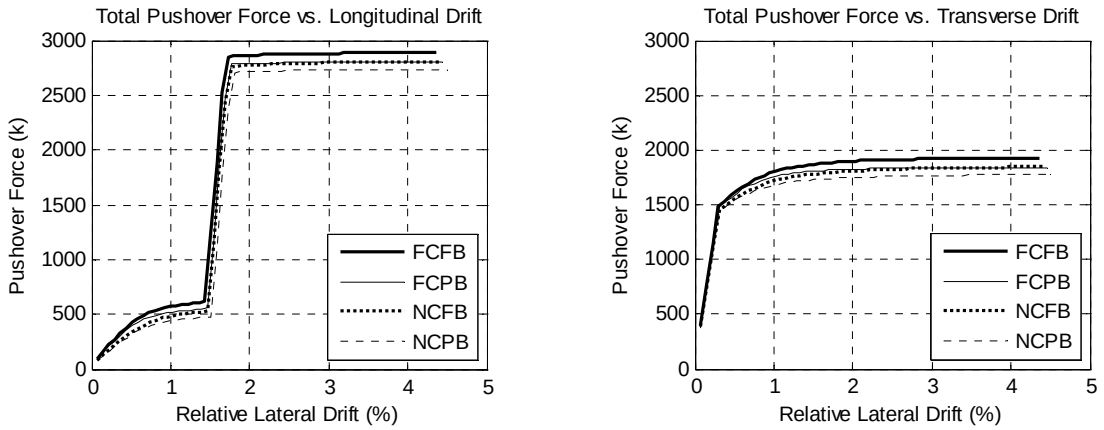

(a) Longitudinal Pushover (b) Transverse Pushover

Fig. 13. OpenSees Static Pushover Analysis Results (Total Pushover Force)

5.1.1 Strength

The large increases in strength for the results with the total pushover force are a result of the abutments described in Section 3.2. In the longitudinal direction, there is a six inch gap between the edge of the deck and the abutment; this is shown in Fig. 13 (a) by the jump in strength near 1.5% relative drift. The transverse direction does not have a gap between the deck and the abutment; therefore, there is a significant increase in the initial strength shown in Fig. 13 (b).

It is clear from the previous static pushover results that the FCFB case consistently has the greatest strength, the NCPB case consistently has the lowest strength, and the FCPB and NCFB cases have intermediate strength values. The FCPB case has a higher strength than the NCFB case for lower values of drift; however, as the drift increases, the strength in the NCFB case increases at a slightly faster rate than that of the FCPB case.

While the results for the total pushover force are useful for verifying the effect of the abutments, the corrosion damage accounted for within this research is limited to the column. Therefore, the strength decrease in the column due to the corrosion damage must be obtained; this is found in Fig. 12. Table 14 shows the decrease in strength for all of the cases representing a decrease in concrete cover or rebar diameter. The first column denotes which two cases are compared: FCFB – NCFB and FCPB – NCPB represent the reduction in strength resulting from removal of the concrete cover while FCFB – FCPB and NCFB – NCPB represent the strength reduction resulting from a decrease in rebar diameter. The strength reduction values change as the drift increases; therefore, results at both 1% and 2% relative drift are presented.

Table 14. Strength Reductions

Cases	1% Drift	2% Drift
FCFB – NCFB	17.6 %	15.0 %
FCPB – NCPB	18.6 %	16.2 %
FCFB – FCPB	9.6 %	11.6 %
NCFB – NCPB	6.3 %	12.8 %

The static pushover results show that removing the concrete cover results in a decrease of approximately 17% in the base shear while decreasing the rebar diameter by 10% results in a decrease in the base shear of approximately 10%. These values are obtained by averaging the results shown in Table 14.

5.1.2 Stiffness

Another important structural parameter affected by corrosion is the stiffness. The static pushover results presented previously also give important information regarding the stiffness changes in the bridge resulting from corrosion damage. Fig. 12 shows the static base shear vs. lateral drift plot and clearly shows a decrease in the initial slope, or stiffness, of the pushover curve as the level of corrosion damage is increased. Similar to the relationship for strength, the FCFB case has the highest stiffness followed by the FCPB, NCFB, and NCPB cases. Table 15 shows the initial stiffness values in each direction from the column base shear pushover curves for each of the four cases. The stiffness values are obtained from a bilinear analysis of the pushover data.

Table 15. OpenSees Bilinear Pushover Stiffnesses

Case	Longitudinal Stiffness (k/in)	Transverse Stiffness (k/in)
FCFB	224.16	177.66
FCPB	210.69	167.72
NCFB	167.27	143.01
NCPB	151.31	133.82

From the previous table, the percent decrease in stiffness resulting from the removal of the concrete cover and the decrease in rebar diameter is calculated and shown in Table 16.

Table 16. Stiffness Reductions

Cases	Longitudinal	Transverse
FCFB – NCFB	25.4 %	19.5 %
FCPB – NCPB	28.2 %	20.2 %
FCFB – FCPB	6.0 %	5.6 %
NCFB – NCPB	9.5 %	6.4 %

The decrease in stiffness resulting from concrete cover spalling alone is approximately 27% in the longitudinal direction and approximately 20% in the transverse direction. The decrease in stiffness resulting from a decrease in rebar diameter alone is approximately 8% in the longitudinal direction and approximately 6% in the transverse direction. It can be seen that the stiffness values for the longitudinal direction are slightly higher than those for the transverse direction; however, these stiffness values do not account for the effect of the abutments. Once the abutment stiffnesses are added, the longitudinal stiffnesses are drastically higher than the stiffnesses in the transverse direction, which can be seen in Fig. 13 of the previous section where the pushover curve accounts for the effect of the abutment stiffnesses.

When the total pushover force for the full bridge significantly increases in the longitudinal direction after the abutment stiffnesses are activated (i.e. once the gap of six inches is closed), the effects of the decreased concrete cover and rebar diameter are

decreased. Before the abutment springs are activated, the stiffness of the bridge (corresponding to the total pushover force) is relatively low; therefore the effects of the damage will be greater. However, once the abutment springs are activated in this direction, the total pushover force for all cases is significantly larger making the difference between the damaged and undamaged cases relatively small. For the transverse direction, the abutment springs are activated immediately; therefore, there is a large increase in the initial stiffness of the bridge. For both the longitudinal and transverse directions, the abutment spring stiffnesses are significantly larger than the stiffness of the column; therefore, once the abutment springs are activated, the corrosion damage causes a relatively insignificant difference in stiffness between the four cases.

5.2 Dynamic Analysis

The dynamic analysis performed in this research is similar to that used in Mackie and Stojadinović (2003). The displacement response data is normalized based on the height of the column, and it is referred to as the drift (in percent). The drift in the longitudinal direction ($\Delta_{x,i}$) at every analysis time step, for example, is found using the following equation,

$$\Delta_{x,i} = \left(\frac{x_i}{L} \right) \cdot 100\% \tag{4}$$

where x_i is the relative displacement in the longitudinal direction at each time step, i, and L is the length of the column (L=300 in).

The lateral drift vs. time results for each earthquake in the longitudinal and transverse directions are developed, and an example of this data is shown in Fig. 14 (a)

and (b), respectively, for the first earthquake in the Near field bin. For clarity purposes, only the FCFB and NCPB cases are shown here; however, these plots are developed for all four analysis cases of each earthquake record.

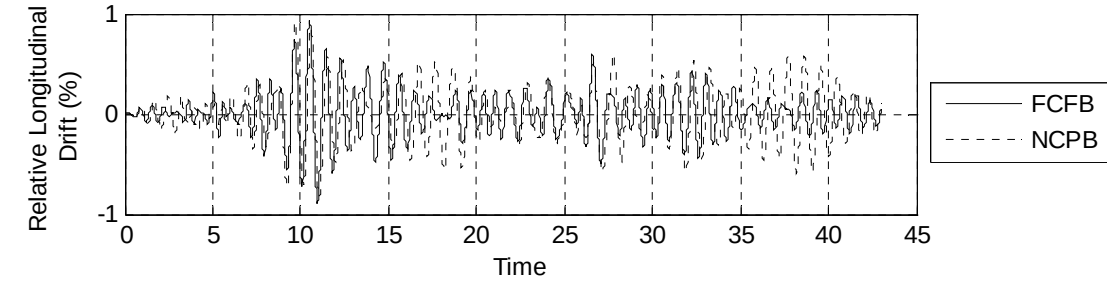

(a) Longitudinal Direction

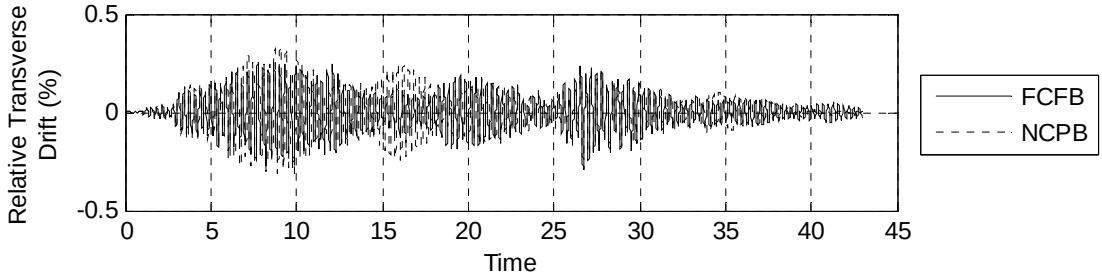

(b) Transverse Direction

Fig. 14. Earthquake Time Histories (Near, Earthquake 1)

These plots show the differences in magnitude of the longitudinal and transverse drifts for the FCFB and NCPB cases. In most cases, the frequency content of the responses remained similar between the four analysis cases; however, the NCPB case has almost consistently higher drift values. The higher drifts are expected in the damaged cases because of the decreased stiffness due to the loss of the concrete cover.

These figures also show the difference in frequency content between the longitudinal and transverse directions; the frequency in the transverse direction is noticeably higher.

5.2.1 Strength

The dynamic relationship between the column base shear and the lateral drift shows a relationship between the strengths of the four analysis cases that is similar to what is seen with the static analysis. Fig. 15 shows the longitudinal base shear vs. the longitudinal drift, the transverse base shear vs. the transverse drift, and the total base shear vs. the total drift in the column for the fourth earthquake in the SMLR bin scaled up by a factor of 11.

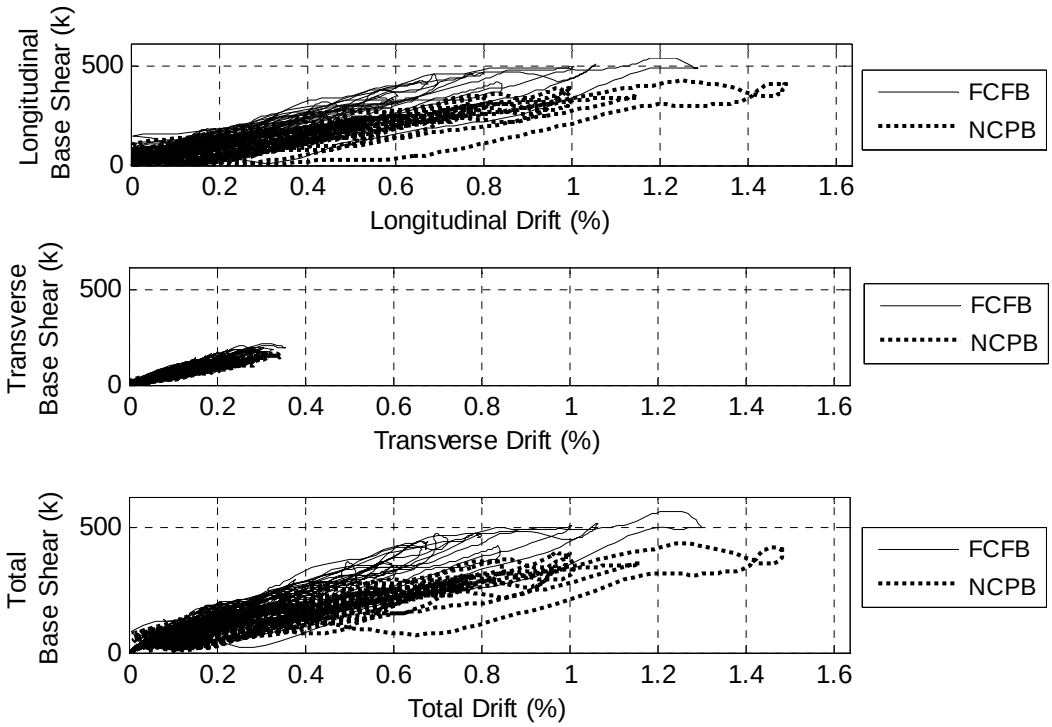

Fig. 15. Base Shear vs. Lateral Drift (SMLR, Earthquake 4, Scaled (11))

The total base shear, $V_{total,i}$, and the total lateral drift, $\Delta_{total,i}$, at every analysis time step are defined in the following equations,

$$V_{total,i} = \sqrt{V_{x,i}^2 + V_{y,i}^2} \tag{5}$$

$$\Delta_{total,i} = \sqrt{\Delta_{x,i}^2 + \Delta_{y,i}^2} \tag{6}$$

where $V_{x,i}$ and $V_{y,i}$ are the base shear forces in the longitudinal and transverse directions, respectively, and $\Delta_{x,i}$ and $\Delta_{y,i}$ are the lateral drifts in the longitudinal and transverse directions, respectively, at every point in time. The results for the total base shear and total drift are plotted only in the first quadrant because only positive values are obtained from these calculations; to correspond with this data, the longitudinal and transverse plots are also shown only in the first quadrant. In reality, the longitudinal and transverse base shear vs. drift plots have data in the first and third quadrants.

As shown, the drift values corresponding to the longitudinal direction are greater than the similar results in the transverse direction; this is true for most earthquake records. There are only a few cases where the transverse drift is larger than the longitudinal drift, and it is assumed that either there is model instability (as in the case of the third earthquake record in the scaled up Near field bin) or the magnitude of the earthquake record in the transverse direction is significantly larger than the one applied in the transverse direction.

From the base shear vs. lateral drift plots, it is found that most of the unscaled earthquake records remained in the elastic range; however, as the scale factor is increased, the earthquake responses become more inelastic. Interestingly, the results for

some of the inelastic cases (like Fig. 15, for example) tend to have wavy lines, and some even have loops at or near the maximum drift values which are not seen in typical force-displacement curves. These loops are most likely due to three-dimensional modal coupling effects and the application of vertical earthquake records. These loops are only seen with the nonlinear results.

The dynamic base shear vs. lateral drift plots show that the NCPB bridge column has consistently lower base shear values than the FCFB column. In other words, there is a decrease in strength from the FCFB to the NCPB case. While the data for the FCPB and NCFB cases is not presented in this section, the FCPB case shows a slight decrease in strength and stiffness from the FCFB case while the NCFB case shows a slight increase in strength and stiffness from the NCPB case.

5.2.2 Stiffness

The dynamic relationship between the column base shear and the lateral drift is also informative for determining the differences in stiffness between the undamaged and damaged analysis cases. In addition to showing a decrease in strength, Fig. 15 shows a decrease in stiffness between the FCFB and NCPB cases. The slope of the curves for the NCPB case is less steep than the FCFB case; therefore, the NCPB case reaches higher drift values for a given lateral force. This means that the NCPB case is less stiff than the FCFB case under dynamic loading, and this result is comparable to that found from the static analysis. Although the dynamic base shear vs. lateral drift data for the FCPB and NCFB cases is not presented in this section, the results follow the same trend seen in the static analysis.

In addition to evaluating the relationship between the base shear and lateral drift, the relationship between the lateral drifts in the two horizontal directions is compared for all four analysis cases. Fig. 16 tracks the top column node in the horizontal plane during the dynamic analysis induced by the sixth earthquake in the SMSR bin. The FCFB and NCPB results are the only ones shown here for clarity purposes; however, this analysis is performed for all four analysis cases using the data from all of the earthquake records.

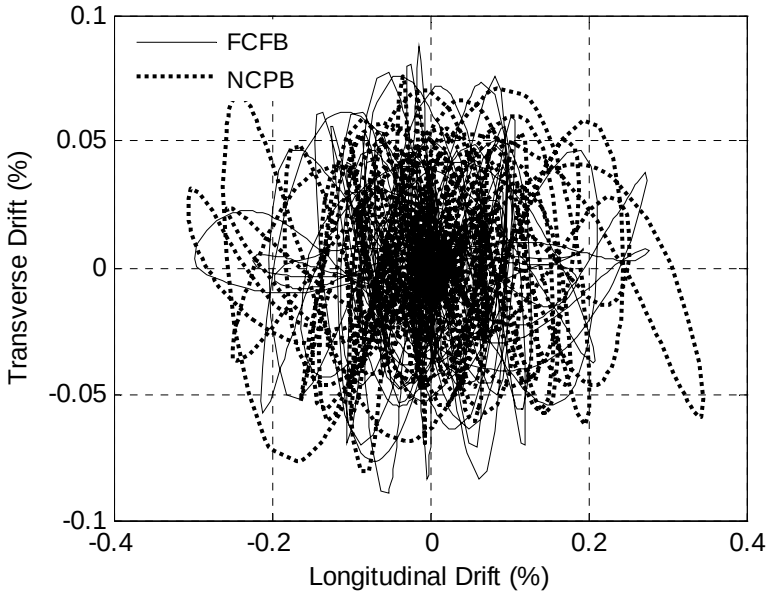

Fig. 16. Transverse Drift vs. Longitudinal Drift (SMSR, Earthquake 6)

The previous figure shows two important results: first of all, the drift in the longitudinal direction is much larger than the drift in the transverse direction, and secondly, the drifts for the NCPB case are larger in almost all directions. The first result could mean that either the transverse direction is stiffer or that a smaller dynamic force is

applied in the transverse direction. Because the path of the NCPB case has larger drift values than the FCFB case, it is concluded that the damaged case is less stiff. The NCPB case does not show a greater drift value in both the longitudinal and transverse directions in every earthquake response; however, this trend is seen for most cases. These increased drift values are expected because of the decreased stiffness in the NCPB case resulting from the corrosion damage.

After comparing the drifts in the longitudinal and transverse direction to each other, the value of the total drift and its corresponding angle are determined for each analysis case. In this case, the total drift refers to the drift calculated using the square root of the sum of the squares of the horizontal components of drift at every time. The equations for the total drift and the angle of this drift at every point in time are given in the following equations,

$$\Delta_{total,i} = \sqrt{\Delta_{x,i}^2 + \Delta_{y,i}^2} \tag{7}$$

$$\alpha_i = \tan^{-1}\left(\frac{\Delta_{y,i}}{\Delta_{x,i}}\right) \tag{8}$$

where $\Delta_{x,i}$ is the longitudinal drift, $\Delta_{y,i}$ is the vertical drift, and α_i is the angle of drift at every point in time. According to this definition of α_i, the longitudinal direction is along the 0^0 line. The first plot in Fig. 17 shows the results for the total drift at every point in time, the second plot shows the total drift at each point in time near the maximum total drift, and the third plot shows the angle of drift at each point in time near the maximum total drift. Fig. 17 shows the results for the sixth earthquake record in the un-scaled

SMSR bin. Only data from the FCFB and NCPB analysis cases is shown here; however, this same procedure is performed for all earthquake records and all four analysis cases.

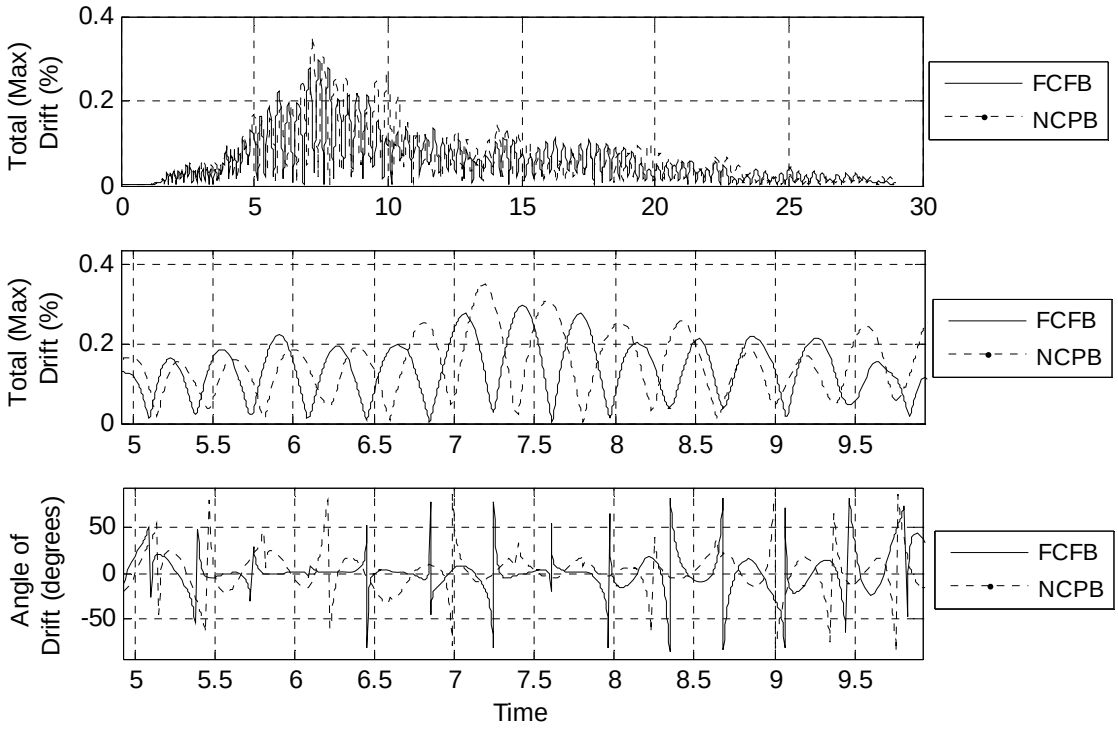

Fig. 17. Total Drift and Corresponding Drift Angle (SMSR, Earthquake 6)

After analyzing the previous data for all earthquakes, it is found that the maximum drift value typically occurs very close to the 0^0 line; this corresponds to a maximum drift in the longitudinal direction. This result means that the displacements in the longitudinal direction are greater than those in the transverse direction for most earthquake records; this is justified by the fact that the period in the longitudinal direction is larger than the period in the transverse direction. This figure also shows that

the total drift from the NCPB case is larger at most points in time; however, the damage does not change the angle of the maximum drift.

Another way that the changes in stiffness due to increased corrosion damage can be tracked is through the changes in the fundamental periods of the bridge prior to seismic loading. Table 17 shows the periods in the longitudinal, transverse, and vertical directions for each of the four analysis cases. These particular periods are found using the Fast Fourier Transform (FFT) analysis described in APPENDIX F.

Table 17. Bridge Periods (sec)

Direction	FCFB	FCPB	NCFB	NCPB
Longitudinal	0.6068	0.6068	0.7123	0.7123
Transverse	0.2979	0.2979	0.3034	0.3034
Vertical	0.0972	0.0969	0.1060	0.1057

Table 17 shows that the periods in the longitudinal and transverse directions do not change when the rebar diameter is decreased; however, there is an increase in the periods when the concrete cover is removed. This means that the stiffness decreases in all directions when the concrete cover is removed, but it remains virtually the same in the longitudinal and transverse directions when the rebar diameter is decreased. This result is expected based on some of the model verification results presented previously.

Table 17 also shows that the difference in the periods in the longitudinal direction is much greater than the difference in the transverse direction. The period decreases more in the longitudinal direction because of the six inch gap between the

bridge deck and the abutment which allows the column stiffness to dominate the period. This gap is not present in the transverse direction; therefore, the significantly larger abutment stiffness controls the period in that direction and the damage in the column has little effect.

These longitudinal and transverse periods are used to determine the spectral acceleration and displacement values used for each selected earthquake time history in the following sections. The acceleration and displacement response spectras used for this research were downloaded directly from the PEER Strong Motion Database (2008) website; these curves are verified for 5% damping using the earthquake acceleration record and Newmark's method for linear systems. The relationship between the spectral acceleration (S_a) and the spectral displacement (S_d) is given below, where T is the period.

$$S_a = \omega^2 S_d \tag{9}$$

$$\omega = \frac{2\pi}{T} \tag{10}$$

As an example, the displacement response data for the first earthquake in the Near Field bin is shown in Fig. 18 along with its corresponding 5% damped spectral acceleration and spectral displacement curves in the longitudinal direction. The longitudinal periods for the FCFB and NCPB cases are marked on the response spectra curves using a solid and dashed line, respectively, to denote the spectral values which are used for the analyses in future sections. This same procedure is repeated in the

transverse direction using the appropriate periods given in Table 17. The entire process is then repeated for all earthquakes used for the dynamic analysis in OpenSees.

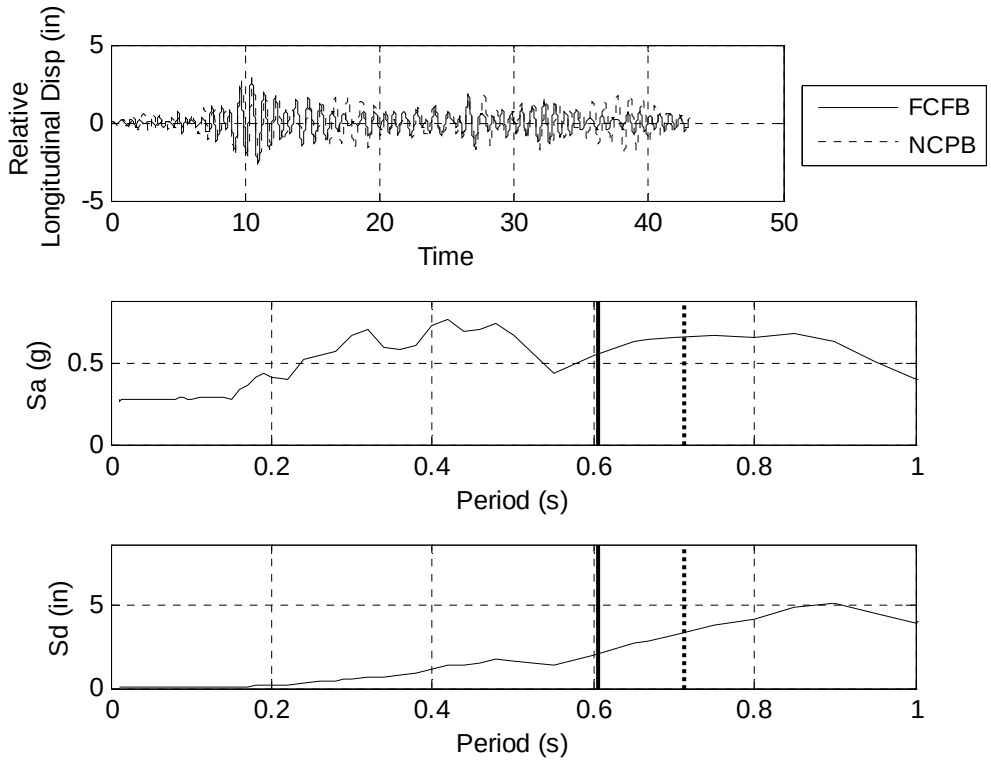

Fig. 18. Acceleration and Displacement Response Spectras (Near, Earthquake 1)

One important issue to note is that the spectral response curves are dependent on the amount of damping in the structure. The OpenSees model accounts for 2% equivalent viscous damping in addition to material hysteretic damping. Therefore, all response spectras used for this research correspond to 5% damping; this is also a commonly accepted value for design.

5.3 Fragility

One way that the behavior of the bridge is quantified in this research is through the use of the structural fragility. Fragility is defined as the conditional probability of failure of a structure with a specific set of demand parameters (Gardoni et al. 2002). To perform a fragility analysis, it is necessary first to develop both a demand and a capacity model.

5.3.1 Demand Models

For this research, two different procedures are used to develop the probabilistic demand models. In general, the demand models are developed based on the relationship between the maximum lateral drift from the OpenSees analysis and the spectral acceleration from the earthquake response spectras because of the precedence set in Ramamoorthy et al. (2006). A probabilistic linear model using the maximum likelihood estimate (MLE) approach is developed to capture the demand data, and the model is represented by the following equation,

$$\ln\left(\Delta_{total,true}\right) = \theta_0 + \theta_1 \ln\left(S_{a,SRSS}\right) + \sigma\varepsilon \tag{11}$$

where θ_0 and θ_1 are unknown model parameters, ε is a random variable with zero mean and a unit standard deviation, and σ is the unknown standard deviation of the model. For the single degree of freedom bridge modeled in this research, the previous equation, representing a single linear model, is sufficient.

The first demand model developed a relationship between the maximum total drift for each earthquake time history obtained from the OpenSees analysis, $\Delta_{total,true}$, and

the square root of the sum of the squares (SRSS) of the spectral acceleration values in both the x and y directions, $S_{a,SRSS}$. These quantities are described as follows,

$$\Delta_{total,true} = \max\left(\sqrt{\Delta_{x,i}^2 + \Delta_{y,i}^2}\right) \tag{12}$$

$$S_{a,SRSS} = \sqrt{S_{a,x}^2 + S_{a,y}^2} \tag{13}$$

where $\Delta_{x,i}$ and $\Delta_{y,i}$ are the values of drift at every analysis time step in the longitudinal and transverse directions, respectively, and $S_{a,x}$ and $S_{a,y}$ are the spectral acceleration values corresponding to the bridge periods in the longitudinal and transverse directions, respectively. One data point is collected for each earthquake, and Fig. 19 (a) and (b) show the resulting plots in the natural log space and the original space, respectively. Only the FCFB and NCPB cases are shown for clarity reasons.

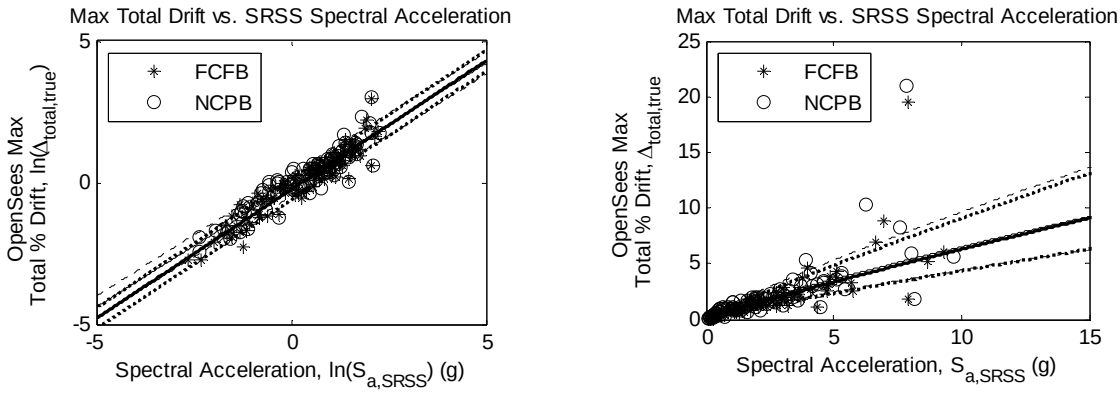

(a) Natural Log Space **(b)** Original Space

Fig. 19. Maximum Total Drift vs. SRSS Spectral Acceleration

The figures above show that the NCPB case has slightly higher demands than the FCFB case; however, there is not a significant difference in the demands. These results show that the difference in the demand model between the four analysis cases is relatively small. The values and statistical information for the unknown probabilistic demand model parameters for each corresponding damage analysis case are shown in Table 18.

Table 18. MLE Statistics for Parameters in Total Demand Model ($S_{a,SRSS}$)

				Correlation Coefficients		
Case	Parameter	Mean	Standard Deviation	θ_0	θ_1	σ
FCFB	θ_0	-0.2571	0.0426	1.0		
	θ_1	0.9095	0.0365	-0.2811	1.0	
	σ	0.3669	0.0283	-0.0425	-0.0684	1.0
FCPB	θ_0	-0.2232	0.0424	1.0		
	θ_1	0.9105	0.0367	-0.2824	1.0	
	σ	0.3825	0.0289	-0.0069	0.0274	1.0
NCFB	θ_0	-0.1355	0.0415	1.0		
	θ_1	0.8617	0.0367	-0.2600	1.0	
	σ	0.3732	0.0280	0.0069	0.0270	1.0
NCPB	θ_0	-0.1053	0.0465	1.0		
	θ_1	0.8595	0.0369	-0.2175	1.0	
	σ	0.3891	0.0294	0.0178	-0.0024	1.0

This demand model is also developed in an identical way using the spectral displacement values, as opposed to the spectral acceleration values. Similar figures and tables of information are developed, and these can be found in APPENDIX H.

The second demand model developed also related the maximum total drift obtained from OpenSees to the spectral acceleration values; however, the procedure is slightly different. The first step in this method is determining the relationship between the maximum drift and the corresponding spectral acceleration in each of the respective horizontal directions (i.e. longitudinal and transverse). Fig. 20 (a) and (b) show the results for the FCFB and NCPB cases in the natural log space for the longitudinal and transverse directions, respectively. Similar figures are also made for the FCPB and NCFB cases.

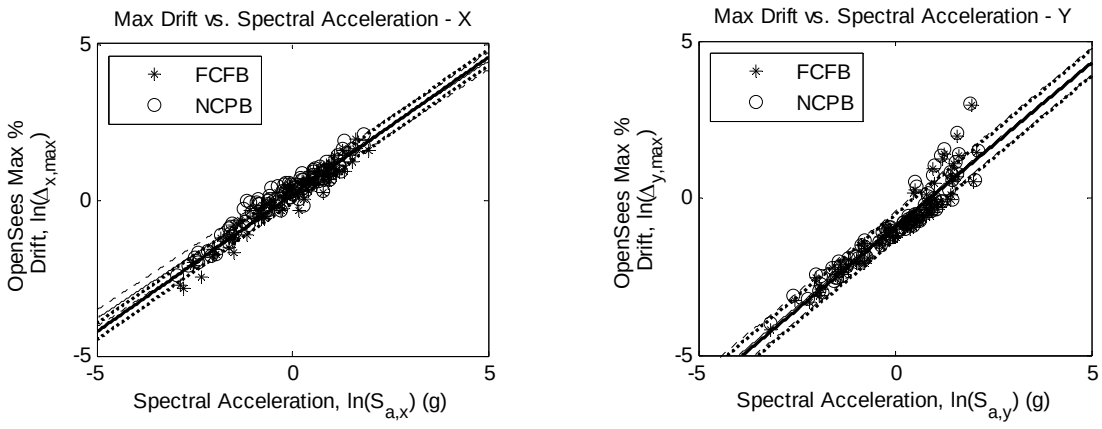

(a) Longitudinal Direction

(b) Transverse Direction

Fig. 20. Maximum Drift vs. S_a

The MLE method is used to fit a single linear model to the data in each of the figures above, and equations of the following form are developed.

$$\ln\left(\Delta_{x_{\max,calc}}\right) = \theta_{0,x} + \theta_{1,x} \cdot \ln\left(S_{a,x}\right) \pm \sigma_x \varepsilon \tag{14}$$

$$\ln\left(\Delta_{y_{\max,calc}}\right) = \theta_{0,y} + \theta_{1,y} \cdot \ln\left(S_{a,y}\right) \pm \sigma_y \varepsilon \tag{15}$$

A single linear model with a varying standard deviation value (σ_y) in the transverse direction can be developed based on the noticeable jump in the scatter shown in Fig. 20 (b); however, this is not accounted for in the current research. The unknown parameters for each analysis case are tabulated with their corresponding statistical information for each direction. Table 19 and Table 20 show this data for the longitudinal and transverse directions, respectively.

Table 19. MLE Statistics for Parameters in Longitudinal Demand Model ($S_{a,x}$)

				Correlation Coefficients		
Case	Parameter	Mean	Standard Deviation	$\theta_{0,x}$	$\theta_{1,x}$	σ_x
FCFB	$\theta_{0,x}$	0.1528	0.0271	1.0		
	$\theta_{1,x}$	0.8792	0.0238	0.1538	1.0	
	σ_x	0.2571	0.0190	0.0113	0.0060	1.0
FCPB	$\theta_{0,x}$	0.1884	0.0397	1.0		
	$\theta_{1,x}$	0.8807	0.0277	0.2072	1.0	
	σ_x	0.2782	0.0207	0.0125	0.0270	1.0
NCFB	$\theta_{0,x}$	0.2811	0.0299	1.0		
	$\theta_{1,x}$	0.8249	0.0238	0.2469	1.0	
	σ_x	0.2522	0.0206	0.0981	0.0643	1.0
NCPB	$\theta_{0,x}$	0.3085	0.0276	1.0		
	$\theta_{1,x}$	0.8247	0.0255	0.2844	1.0	
	σ_x	0.2752	0.0200	0.1286	-0.0983	1.0

Table 20. MLE Statistics for Parameters in Transverse Demand Model ($S_{a,y}$)

				Correlation Coefficients		
Case	Parameter	Mean	Standard Deviation	$\theta_{0,y}$	$\theta_{1,y}$	σ_y
FCFB	$\theta_{0,y}$	-0.9617	0.0431	1.0		
	$\theta_{1,y}$	1.0483	0.0370	-0.0817	1.0	
	σ_y	0.4138	0.0307	0.0416	0.0172	1.0
FCPB	$\theta_{0,y}$	-0.9450	0.0445	1.0		
	$\theta_{1,y}$	1.0552	0.0401	-0.0589	1.0	
	σ_y	0.4211	0.0319	0.0092	-0.0383	1.0
NCFB	$\theta_{0,y}$	-0.9023	0.0454	1.0		
	$\theta_{1,y}$	1.0308	0.0389	-0.0390	1.0	
	σ_y	0.4249	0.0317	-0.0055	-0.0014	1.0
NCPB	$\theta_{0,y}$	-0.8848	0.0461	1.0		
	$\theta_{1,y}$	1.0397	0.0394	-0.0372	1.0	
	σ_y	0.4320	0.0340	-0.0109	0.0014	1.0

After the maximum drift values in each horizontal direction, $\Delta_{x_{\max,calc}}$ and $\Delta_{y_{\max,calc}}$, are calculated based on $S_{a,x}$ and $S_{a,y}$, respectively, the total maximum drift is calculated using the following equation.

$$\Delta_{total,calc} = \sqrt{\Delta^2_{x_{\max,calc}} + \Delta^2_{y_{\max,calc}}} \tag{16}$$

This maximum total drift, calculated based on the spectral accelerations, is then compared to the maximum total drift found from the OpenSees results. The equation for the OpenSees maximum total drift, $\Delta_{total,true}$, is the same as the one used in the previous demand model, and it is shown again in the following equation.

$$\Delta_{total,true} = \max\left(\sqrt{\Delta_{x,i}^2 + \Delta_{y,i}^2}\right) \tag{17}$$

The relationship between the total maximum drift obtained from OpenSees is then compared against the total maximum drift calculated based on the spectral acceleration values, and Fig. 21 is created. This figure shows the FCFB and NCPB data only, but the same process is performed for the FCPB and NCFB cases as well.

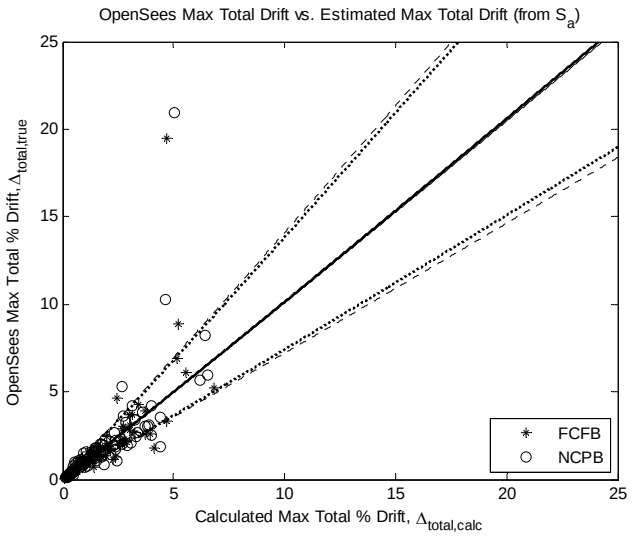

Fig. 21. OpenSees Total Maximum Drift vs. Calculated Maximum Drift (Based on S_a)

In general, it is expected that the data on the horizontal axis in the previous figure should be greater than the corresponding data on the vertical axis since the horizontal axis over-predicts the maximum total drift by using a combination of the maximum drift in the longitudinal and maximum drift in the transverse directions. However, this is not the case for all data points because the maximum drifts in the longitudinal and transverse

directions are calculated based on the single linear models shown in Fig. 20 For some earthquakes (specifically, the third earthquake in the scaled up Near field bin), the calculated maximum longitudinal and transverse drifts are much less than the actual OpenSees records. As an example, the data point near (5,20) on the previous figure follows this explanation.

The previous figure is the second demand model that is used in this research to develop the fragility, and a single linear model of the following form is developed in the natural logarithmic scale for the results,

$$\ln\left(\Delta_{total,true}\right) = \theta_0 + \theta_1 \cdot \ln\left(\Delta_{total,calc}\right) \pm \sigma\varepsilon \tag{18}$$

where $\Delta_{total,true}$ represents the OpenSees results and $\Delta_{total,calc}$ represents the results calculated from the spectral acceleration values for each earthquake. The unknown parameters, and their statistical data, are given in Table 21 for all four analysis cases.

Table 21. MLE Statistics for Parameters in Total Demand Model (Based on S_a)

				Correlation Coefficients		
Case	Parameter	Mean	Standard Deviation	θ_0	θ_1	σ
FCFB	θ_0	-0.0467	0.0332	1.0		
	θ_1	1.0251	0.0327	-0.1223	1.0	
	σ	0.3114	0.0210	-0.1167	0.0578	1.0
FCPB	θ_0	-0.0458	0.0351	1.0		
	θ_1	1.0244	0.0351	-0.1421	1.0	
	σ	0.3290	0.0280	-0.0318	0.0557	1.0
NCFB	θ_0	-0.0489	0.0351	1.0		
	θ_1	1.0255	0.0369	-0.1998	1.0	

Table 21. Continued

Case	Parameter	Mean	Standard Deviation	Correlation Coefficients		
				θ_0	θ_1	σ
NCPB	σ	0.3194	0.0252	0.0759	-0.0414	1.0
	θ_0	-0.0461	0.0364	1.0		
	θ_1	1.0227	0.0369	-0.2274	1.0	
	σ	0.3360	0.0261	-0.0202	0.0372	1.0

This demand model is useful because it helps show the accuracy of the models in the separate longitudinal and transverse directions. The calculated maximum total drift was expected to be slightly larger than the OpenSees maximum total drift; however, the OpenSees data is slightly larger based on the best fit line. When accounting for the 90% confidence bounds (noted by the dashed lines in Fig. 21), the maximum total drift from OpenSees has almost a 1:1 relationship with the maximum total drift calculated based on the spectral acceleration values. This entire process is also repeated using the relationship between the maximum drift values and the spectral displacement, and the results can be seen in APPENDIX H.

This second demand model also shows that there is not a significant difference in the demand between the four analysis cases; however, this demand model shows that the FCFB case actually has slightly higher demands. This result is not expected, and it is most likely due to a bias in the data that results from comparing the OpenSees drift values to predicted drift values based on S_a instead of comparing the OpenSees results directly to S_a.

5.3.2 Capacity Model

After the two demand models are developed, the deterministic and probabilistic drift capacities are calculated based on the method developed in Gardoni et al. (2002) and modified in Choe et al. (2007b). The drift capacity is defined as the drift corresponding to a decrease in lateral load resistance of 20% compared to the peak value (Gardoni et al. 2002). The input values for the capacity model can be seen in Table 22 for both the FCFB and NCPB cases.

Table 22. Capacity Model Variables

Property	FCFB	NCPB
$f_c^{'}$	4 ksi	4 ksi
f_y	65 ksi	65 ksi
f_{su}	97.5 ksi	97.5 ksi
f_{yh}	65 ksi	65 ksi
d_b	1.41 in	1.269 in
d_s	0.75 in	0.675 in
H	300 in	300 in
D_g	63 in	57 in
Clear Cover	3 in	0 in
S	4.49 in	4.49 in
Number of bars	40	40
P	1200 k	1200 k
ϕ_y	0.00010414 1/in	0.00012049 1/in
ϕ_u	0.00140997 1/in	0.00136994 1/in
M_y	88,494 k-in	61,542 k-in
M_I	102,435 k-in	74,191 k-in

The axial load for the column, P, represents the self weight of the bridge deck, and S represents the spacing between the transverse, hoop steel. The yield and ultimate curvature and moment values are obtained from OpenSees based on the definition provided in Gardoni et al. (2002). The yield moment, M_y, is defined as the moment which first induces yielding of the longitudinal column reinforcement. The ideal moment, M_I, represents the moment which corresponds to the idealized yield curvature, ϕ_y. The ultimate curvature, ϕ_u, represents the curvature when the strain in the concrete reaches its ultimate confined strain (Gardoni et al. 2002). The input moment and curvature values used in the capacity model are verified using results from PCA Column and USC_RC. While these programs do not give the exact same values, the results are comparable, especially when considering the modeling differences in all three programs. The comparison data for the moment and curvature values can be seen in APPENDIX I, and more information regarding the modeling differences between the three programs can be found in APPENDIX D and APPENDIX E.

The deterministic and probabilistic results from the drift capacity model are shown in Table 23. The values of $\hat{d}$ and d_{corr} correspond to the deterministic and probabilistic drift capacities, respectively. The values shown in Table 23 for Δ_f, Δ_{sh}, Δ_{sl}, and Δ_p refer to the flexural, shear, slip, and plastic deflections, respectively, and these parameters are defined in Gardoni et al. (2002). The probabilistic drift capacity accounts for uncertainties in modeling as well as biases inherent in the deterministic

model (Gardoni et al. 2002). The probabilistic capacity is a more accurate, albeit less conservative, estimate of the ultimate drift capacity at collapse.

Table 23. Drift Capacity Results

Property	FCFB	FCPB	NCFB	NCPB
Δ_f (in)	3.4172	3.3651	3.7124	3.9190
Δ_{sh} (in)	0.0376	0.0355	0.0355	0.0353
Δ_{sl} (in)	0.4353	0.3892	0.4729	0.4533
Δ_p (in)	14.788	13.165	15.591	13.634
$\hat{d}$ (%)	0.0623	0.0565	0.0660	0.0601
d_{corr} (%)	0.0777	0.0810	0.0874	0.0904

One interesting feature of the drift capacity results is that all of the damaged cases have higher probabilistic drift capacity values than the undamaged (FCFB) case. One possible explanation for this is because the corrosion damage decreases the stiffness of the bridge, leading to higher drift capacity values. Reducing the concrete cover is found to cause a greater increase in the probabilistic drift capacity than reducing the rebar diameter.

The probabilistic drift capacity even increases slightly when the rebar diameter is the only parameter altered to account for corrosion damage; this result is contrary to that seen in Choe et al. (2007a). The results in Choe et al. (2007a) show that the drift capacity decreases slightly over time as the rebar diameter is decreased. It is unclear why these results contradict each other.

The drift capacity developed in this section reflects the ultimate collapse capacity of the structure; however, it is informative to examine this structure based on other traditional capacity limits as well. Three common drift capacities are 1%, 2%, and 4% which represent the serviceability, damage control, and collapse prevention limit states, respectively.

5.3.3 Fragilities

Once the drift demand models and capacity limits are developed for the given bridge, the fragility is approximated by the following equation, originally presented by Wen et al. (2004),

$$F(S_a) \cong 1 - \Phi\left(\frac{\mu_c - \mu_d}{\sqrt{\sigma_d^2 + \sigma_m^2 + \sigma_c^2}}\right) \tag{19}$$

where μ_c and μ_d are the predicted drift capacity and demand, respectively, in the natural logarithmic space for a given spectral acceleration; σ_c and σ_d are the standard deviations associated with the capacity and demand models, respectively; and σ_m represents the modeling uncertainty for the entire system. For this research, σ_c is set equal to 0.4 (Choe et al. 2007b) and σ_m is set equal to 0.3 (Wen et al. 2004). A similar approximate fragility model is used in Ramamoorthy et al. (2006).

The probabilistic capacity values, denoted as d_{corr} in Table 23, are used for the μ_c values in all fragility calculations. As mentioned previously, two different demand models are created; therefore, two different fragilities are developed. The first fragility

curve is developed based on the following demand model, and it is conditioned on $S_{a,SRSS}$.

$$\ln\left(\Delta_{total,true}\right) = \theta_0 + \theta_1 \ln\left(S_{a,SRSS}\right) \pm \sigma\varepsilon \tag{20}$$

The first part of Fig. 22 shows the capacity and demand models for all four analysis cases as a function of $S_{a,SRSS}$. As long as the capacity is greater than the demand, the fragility has a value, i.e. there is a low probability of failure. Once the capacity value equals the demand, the probability of failure is 50%. This can be seen by comparing the two plots in Fig. 22. According to these results, the fragility reaches 0.5 for all four analysis when $S_{a,SRSS}$ is between 12g and 14g. These spectral acceleration values are extremely high because of the high capacity model and the low fundamental periods of the system.

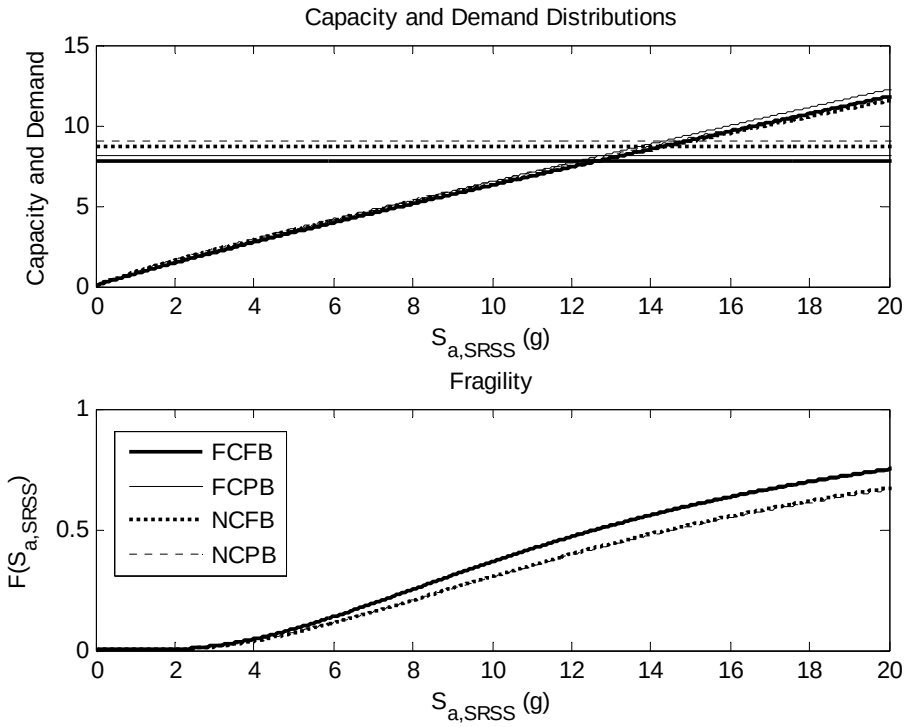

Fig. 22. Capacity and Demand Models with Corresponding Fragility (Based on $S_{a,SRSS}$)

As shown in the previous figure, there is not a significant difference between the four analysis cases. However, it is interesting to note that the fragilities for both cases with full concrete cover have steeper curves than their counterpart cases with no cover. Additionally, the FCFB case has the steepest curve, meaning the highest probability of failure at all levels of S_a. This means that the probability of failure caused by exceeding the drift capacity is greater for the undamaged case. The loss of concrete cover is also found to have a greater effect on the fragility that the loss of rebar diameter. This result is explained because the drift capacities for the damaged cases are higher than the undamaged case, but the demands remain almost the same between the four cases.

For comparison purposes, the fragilities corresponding to the commonly used drift capacity values of 1%, 2%, and 4% are developed for the FCFB case. Fig. 23 shows the capacity and demand models along with the fragility for a drift capacity of 4%. This case represents a conservative collapse prevention limit state for RC structures. It can be seen that the spectral acceleration necessary for a 50% probability of failure of the bridge with a drift capacity of 4% is between 6.0g and 7.0g. This is a significantly smaller spectral acceleration than the one determined from the previous fragility.

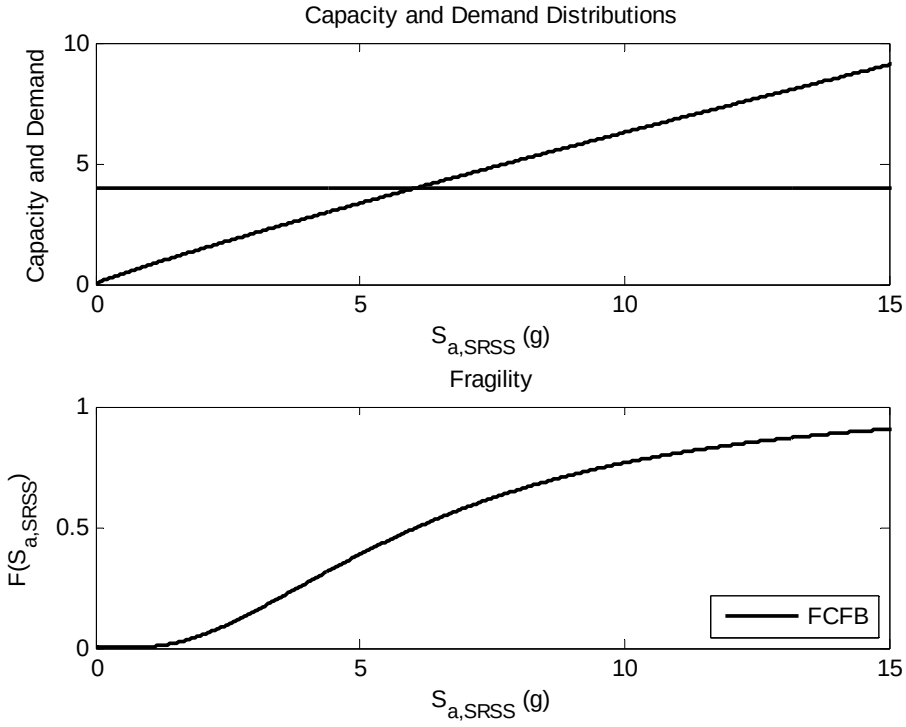

Fig. 23. Capacity and Demand Models with Corresponding Fragility (4% Drift)

The capacity and demand models and the fragility corresponding to a drift capacity of 2% are shown in Fig. 24 for the FCFB case. This drift capacity represents a limit state for damage control. As expected, the spectral acceleration necessary for a 50% probability of failure with a 2% drift capacity is much less than the previous two cases. A spectral acceleration value slightly below 3.0g results in a fragility value of 0.5 for this case.

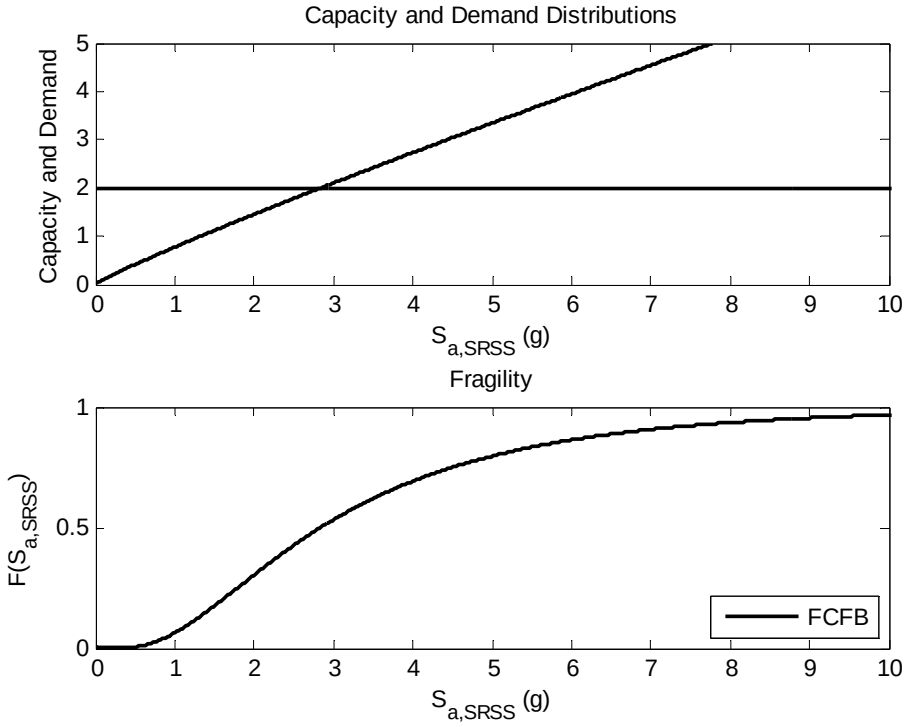

Fig. 24. Capacity and Demand Models with Corresponding Fragility (2% Drift)

Similar plots are presented in Fig. 25 for a drift capacity of 1%, representing a serviceability limit state. This figure shows that a spectral acceleration value just below

1.5g will cause a 50% probability of failure for the FCFB case. When compared to a typical building structure, this spectral acceleration seems high; however, the high stiffness of this bridge dictates the necessity of high forces to reach the specified drift values.

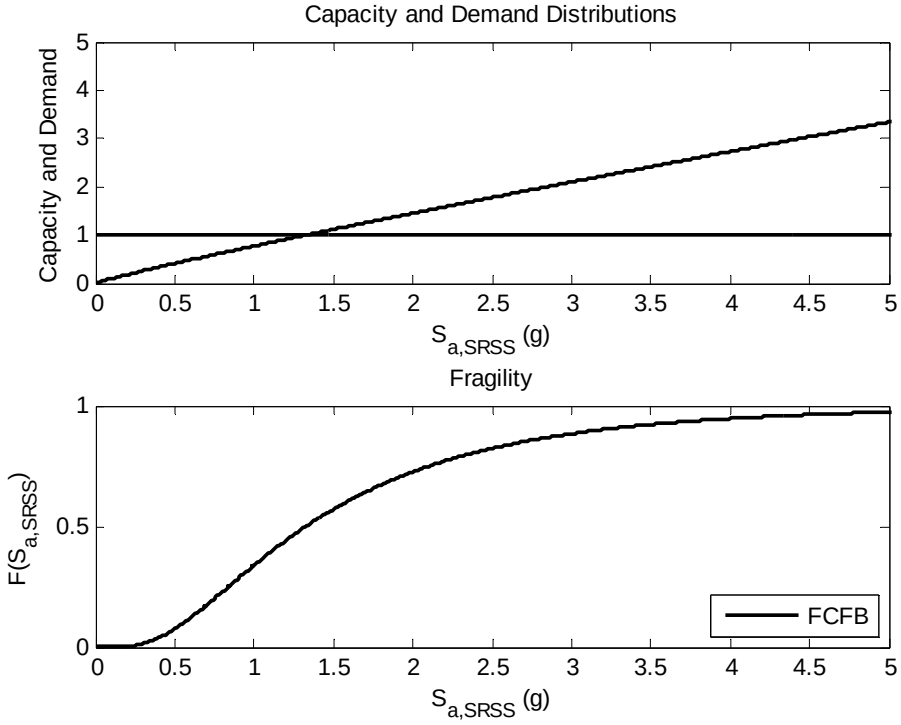

Fig. 25. Capacity and Demand Models with Corresponding Fragility (1% Drift)

Because $S_{a,SRSS}$ is not a very informative parameter for design, a fragility contour plot conditioned on both $S_{a,x}$ and $S_{a,y}$ is also developed for the first demand model. This fragility contour is seen in Fig. 26 for all four analysis cases, and it shows that the

FCFB case has the highest probability of failure while the NCPB case has the lowest probability of failure. This is the same result seen in the previous fragility curves.

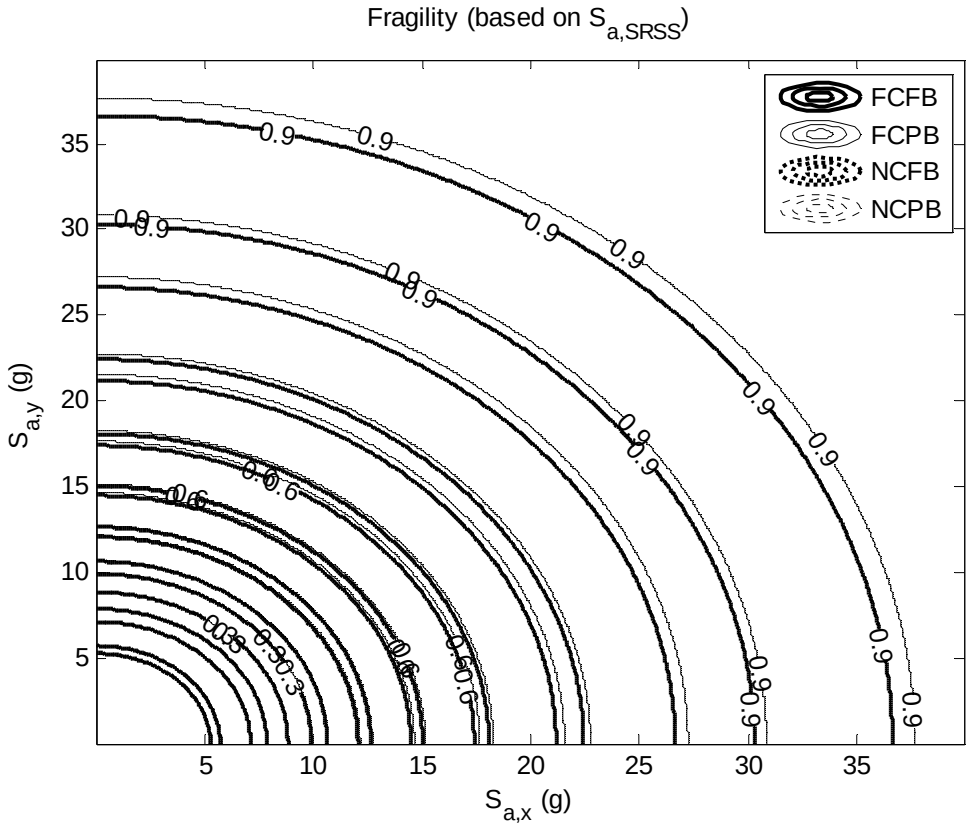

Fig. 26. First Demand Model Fragilities – 4 Cases

Since the fragilities for the four cases are difficult to distinguish in the previous plot, Fig. 27 shows the results for the FCFB and NCPB cases only. One interesting feature of these contours is the fact that both $S_{a,x}$ and $S_{a,y}$ have an equal influence on the fragility; however, this should not necessarily be the case because of the different periods in the longitudinal and transverse directions.

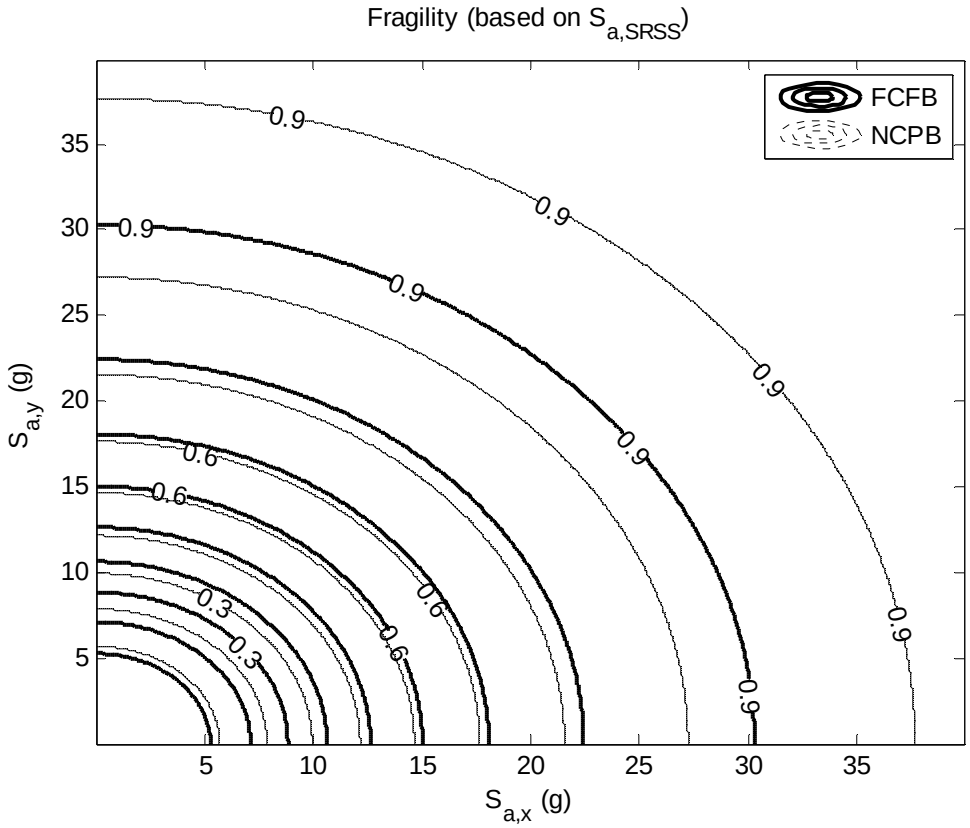

Fig. 27. First Demand Model Fragilities – 2 Cases

A second fragility contour is developed using the second demand model and the same capacity model as the previous case. The demand model for this fragility is given by the following equations, which have been described previously.

$$\ln\left(\Delta_{total,true}\right) = \theta_0 + \theta_1 \cdot \ln\left(\Delta_{total,calc}\right) \pm \sigma\varepsilon \tag{21}$$

$$\Delta_{total,calc} = \sqrt{\Delta^2_{x_{\max,calc}} + \Delta^2_{y_{\max,calc}}} \tag{22}$$

$$\Delta_{x_{\max,calc}} = e^{\left(\theta_{0,x} + \theta_{1,x} \ln\left(S_{a,x}\right)\right)} \tag{23}$$

$$\Delta_{y_{\max,calc}} = e^{\left(\theta_{0,y} + \theta_{1,y} \ln\left(S_{a,y}\right)\right)} \tag{24}$$

The fragility contour plot given in Fig. 28 also shows that there is a larger difference in the probability of failure due to the loss of concrete cover than there is due to the reduction in rebar diameter.

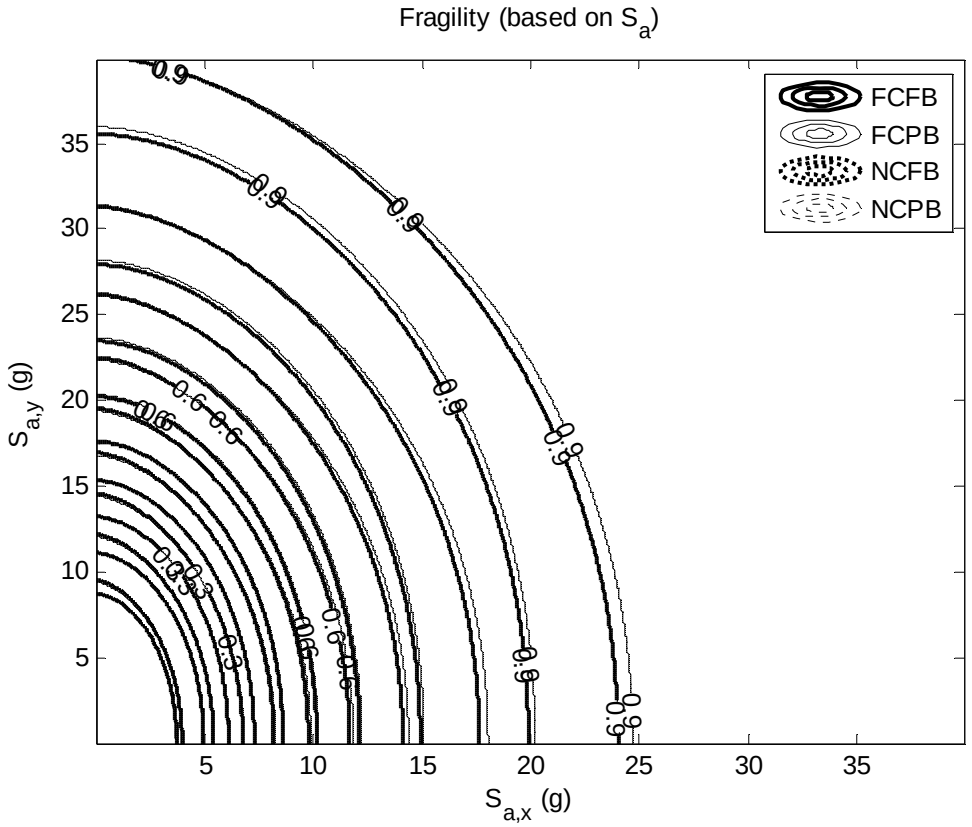

Fig. 28. Second Demand Model Fragilities – 4 Cases

Additionally, this fragility shows that the FCFB case has the highest fragility for a given value of $S_{a,x}$ and $S_{a,y}$, and the NCPB case has the lowest fragility. Since the results for the four analysis cases are hard to distinguish in the previous figure, the fragilities for the FCFB and NCPB cases only are shown in Fig. 29.

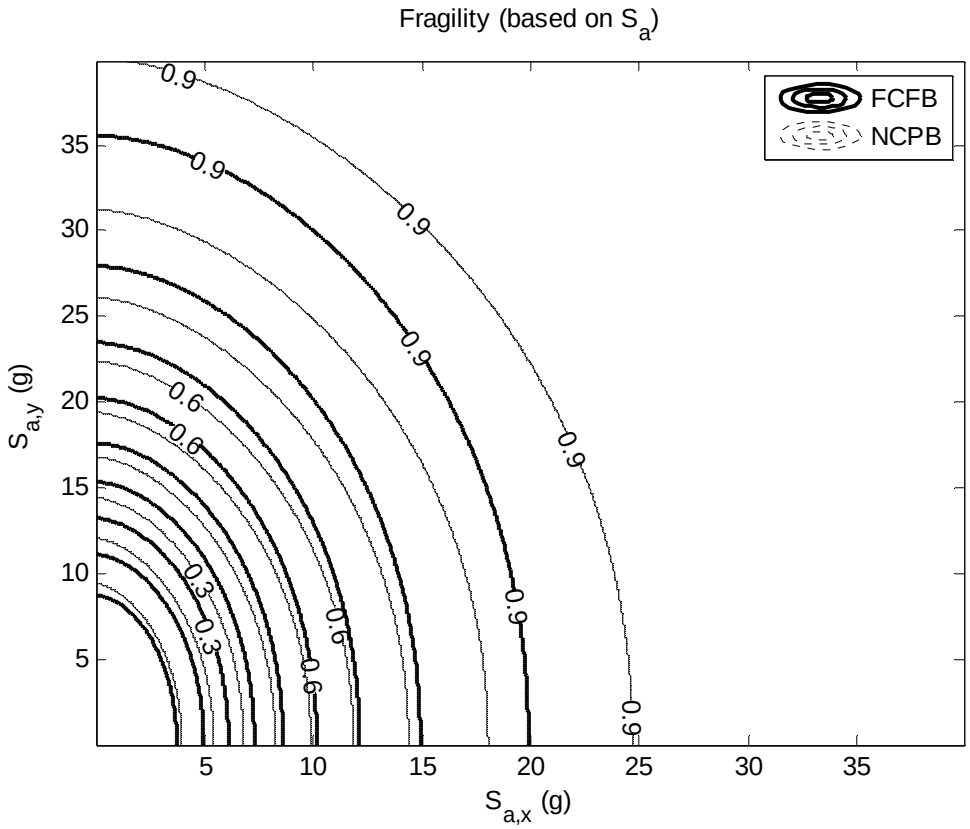

Fig. 29. Second Demand Model Fragilities – 2 Cases

The relative changes in fragility between the four analysis cases have the same relationship for both the first and second demand models; however, there is a slight difference in the shape of the fragility contours between the first and second demand models. The first demand tends to weight the effect of $S_{a,x}$ and $S_{a,y}$ more equally by using the SRSS method to calculate the fragility, while the second demand model accounts for more of the individual effects of $S_{a,x}$ and $S_{a,y}$ when calculating the fragility. The second demand model more accurately reflects the contributions of $S_{a,x}$

and $S_{a,y}$; therefore, the second demand model is more appropriate for this type of fragility.

In any case, both demand models yield the same overall results for the four analysis cases. The FCFB case has the highest fragility, and the NCPB case has the fragility, based on the probability of the drift demand exceeding its corresponding capacity level. The fragility of the FCPB case is not significantly different than that of the FCFB case, and the fragility of the NCFB case is not significantly different than that of the NCPB case.

This result may seem counterintuitive since it means that the pristine bridge seems to have a higher probability of failure than the bridge with corrosion damage; however, this study only accounts for failure resulting from the drift demand exceeding the drift capacity. Overall, the difference between the fragility of the FCFB case and the NCPB case is relatively small at the lower levels of S_a where most earthquake records fall.

6. HISTORIC PRESERVATION CONCERNS

The effect of corrosion damage on historic structures subject to dynamic loading is an important issue, especially with the current aging infrastructure crisis in the United States. It was reported in 2002 that the total annual cost directly related to corrosion in the United States is $22.6 billion (NACE 2002). It was also estimated that the United States would need to invest nearly $9.4 billion dollars per year for the next 20 years in order to fix all bridge deficiencies (ASCE 2005). One study also found that over the past twenty years, the United States has lost over fifty percent of its historic bridges (Sparks 2006). At this point, there is clearly an undisputed need for understanding the behavior of deteriorating RC structures, especially those affected by corrosion. Another concern is that many of these structures are reaching the commonly assumed 50 year age limit necessary to be placed on the National Register of Historic Places; this historic designation will increase the number of restrictions associated with working to strengthen these structures.

While the results obtained in this research are directly related to a specific single-bent bridge under seismic loads, the knowledge gained can be applied broadly to different types of historic structures. There are many historic structures subject to corrosion which must also endure other types of dynamic loadings. This section attempts to broaden the impact of this research.

Before working with an historic structure, it is important to first understand the preservation philosophy with which many of these structures are handled. There are a few basic principles for structural restorations set forth by the Venice Charter in 1964 and presented by Penelis (2002). One of the most important principles is to respect the original materials and time period of the structure. A structural engineer should try to use materials which are compatible with the original fabric, both aesthetically and in terms of material properties (Penelis 2002). Additionally, if replacement parts must be added, they must be done so in harmony with the existing structure; however, an effort must be made to distinguish them from the original historical fabric. Additions to the structure are also only allowed if they do not detract from the significant features of the existing structure. It is also important to strive to use only reversible strengthening and modification techniques when working with historic structures; however if irreversible techniques must be used, then they should be durable alternatives (Penelis 2002). While many of these principles are highly subjective and cannot always be satisfied, the State Historic Preservation Officer (SHPO) is a useful point of contact for consultations related to appropriate modifications.

There are many structures to which the research can be applied almost directly. For example, many historic bridges are highly susceptible to corrosion-related damage due to coastal exposure or deicing salts, and many of these bridges are located in the highly seismic region of the western United States. A case study of the Colorado Street Bridge in Pasadena, California was presented by Thomasen (1995). This reinforced concrete arch bridge with eleven spans was built in 1912-1913, and it was subject to a

significant reduction in steel cross-section and exposed rebar due to corrosion. Because of the low strength concrete and weak abutment supports, each span was essentially designed as its own structure during the rehabilitation process. For this project, the state of California required that the work done on this structure was extensive enough to bring it fully up to the current seismic codes at the time of rehabilitation. The damage seen in this structure is representative of exactly what was studied in this research; however, Thomasen (1995) did not present enough technical information in order to verify any specific results of this work. The process used for rehabilitation included completely encasing large sections of the bridge structure in a steel collar for confinement strength, rebuilding multiple columns, and stiffening the piers (Thomasen 1995). All exposed concrete on the bridge was fully "restored" at the end of the project to ensure that the final structure looked identical to the original bridge. This case study is a good example of how to rehabilitate a damaged structure to ensure safety while making every effort to maintain the historic character. However, it is important to note that many of the techniques used in the rehabilitation of the Colorado Street Bridge do not follow the principles set forth in the Venice Charter. For example, the rehabilitation effort intended for the new additions to look identical to the existing features in appearance; however, the Venice Charter clearly states that all modifications and additions should be clearly distinguishable from the original work.

The work performed on Soldier Field Stadium in Chicago is another example of an historic structure subject to corrosion damage. A case study of the corrosion mitigation process for this structure was presented by Johnson and Lee (2004). This

stadium was built on the Chicago lakefront between 1922 and 1926, and many of the transfer girders and RC beams located in the interior sections of the stadium were subject to corrosion. The Soldier Field case study gives a good summary of the corrosion mitigation techniques applicable for use in an historic structure (Johnson and Lee 2004). The corrosion in this stadium was mostly attributed to either carbonation in the concrete or high chloride content in the architectural coverings of the structural members. This is an interesting concept because it means that many historic structures can be subject to corrosion levels high enough to cause concrete cover spalling even when they are not located in notoriously high susceptibility areas (i.e. near de-icing salts or seawater spray). The only likely dynamic load that this structure is likely to see is the vibrational load from the crowds in the stands. This dynamic load is not nearly as destructive as the seismic loads evaluated for this research; however, over an extended period of time, this relatively low dynamic load could potentially exacerbate problems initiated by the corrosion.

Unexpected or unusual dynamic loads on certain structures could also cause problems in historic structures, especially those subject to corrosion. For example, a large number of people crossing a given bridge at one time can alter the fundamental behavior of the structure and induce unexpected swaying and dynamic motion. This type of dynamic loading could have potentially devastating results for historic structures that have already been weakened due to corrosion.

Another type of dynamic loading that could potentially affect historic structures subject to corrosion is that due to railroad traffic. There are many historic railroad depots

and railroad bridges subject to high cycle fatigue from train vibrations. These dynamic loads are similar to seismic events because of their short durations; however, seismic forces typically cause much higher strains than railroad forces. Another difference between railroad vibrations and seismic events is the frequency of occurrence: railroad vibrations typically affect a structure multiple times a day while seismic events occur much less frequently. The results of this research for the smaller magnitude earthquake records could potentially be applied to structures subject to railroad vibrations; however, some limitations would obviously need to be taken into consideration.

There are many possible preservation and/or rehabilitation techniques that can be used when working with historic structures that have been subject to corrosion. First of all, the surface concrete cover should be patched in a way that does not detract from the aesthetic features of the structure. Patching the concrete cover not only helps stiffen the structure, it also helps protect the rebar from prolonged contact to corrosion-inducing agents. Another way that the rebar can be protected from future corrosion is to use one of many electrochemical treatment options, some of which are provided in Johnson and Lee (2004), to passivate the active corrosion. This alternative will not reverse any of the damage that has already been done; however, it will help to prevent future damage from occurring. Another possible technique would be to add carbon fiber sheets (CFS) to the structure to help increase confinement and increase the resistance to dynamic loads. Since using CFS has proven to be controversial for the aesthetic qualities in some historic structures, this technique should be used with caution.

In general, corrosion in historic RC structures is an important issue confronting the field of historic preservation. Not only can corrosion threaten the structural integrity of an historic structure by decreasing the rebar diameter and spalling the concrete cover, it can also threaten the aesthetic qualities by causing rust staining and cracking in important architectural features.

7. CONCLUSION

7.1 Summary

The motivation of this work stems from the high percentage of corrosion-affected RC structures that are contributing to the aging infrastructure crisis that is currently affecting the United States. Many of these damaged structures are critical to serving the everyday needs of citizens while many other structures are critical to preserving the historic fabric of the built environment in the United States.

The purpose of this research is to determine the effect of corrosion on the seismic response of a single-bent, reinforced concrete bridge by evaluating the effects of changing the concrete cover and the rebar diameter. The changes in strength and stiffness are examined for four representative damage scenarios, and the results are applied to the broader field of historic preservation in order to help structural engineers evaluate and understand how corrosion-affected structures behave when subjected to dynamic loadings.

7.1.1 Effect of Concrete Cover

In general, the results of this research show that removing the concrete cover from a single-bent bridge column decreases the stiffness and, to a lesser extent, decreases the strength of the bridge. The concrete cover also has a significant effect on the drift capacity.

The change in stiffness is relatively significant when the bridge is not restrained by stiff abutment supports; this is seen in this research by the increase in the longitudinal

period when the concrete cover is removed. However, in directions with stiff abutment supports, removing the concrete cover has almost no effect at all; this result is documented in the transverse direction of this bridge.

The results of the static pushover analysis show that removing the concrete cover decreases the base shear and total pushover force for the bridge as well. The decrease in strength seen in the static analysis is more significant when the concrete cover is removed than it is when the rebar diameter is reduced.

Additionally, removing the concrete cover causes an increase in both the deterministic and probabilistic drift capacities. The increase in the probabilistic drift capacities is greater when the concrete cover is removed than when the rebar diameter is reduced. The increased drift capacities also lead to a decrease in the fragility for the cases where the concrete cover was removed.

7.1.2 Effect of Rebar Diameter

A 10% decrease in the diameter of the rebar in the bridge column, an expected worst case scenario for corrosion, also leads to a decrease in the stiffness and strength of the structure; however, the results are not as significant as those seen when removing the concrete cover. This result shows that removing three inches of concrete cover, or effectively decreasing the column diameter by six inches, has a greater effect on the overall behavior of the single-bent, bridge than reducing the rebar diameter by 10%.

The reduction in rebar diameter is found to have practically no impact on the longitudinal and transverse periods of the structure. Decreasing the rebar diameter actually slightly decreases the deterministic drift capacity; however, the rebar reduction

causes a slight increase in the probabilistic drift capacity. Overall, decreasing the rebar diameter only causes a very slight decrease in the fragility given in this report.

7.2 Conclusions

As a result of this study, it is determined that the corrosion damage studied in this research has little overall effect on the seismic behavior of the RC bridge. It is also found that removing three inches of concrete cover on a 63" column has a greater impact on the structural integrity of a single-bent RC bridge than decreasing the rebar diameter by 10%. Overall, this research found that structures damaged by corrosion have a slightly increased ultimate collapse drift capacity as well a slightly increased demand when subjected to seismic loads. The results of this research show that the change in fragility between a pristine bridge and a bridge damaged by corrosion is relatively small.

When the results of this research are compared with those seen in Choe et al. (2008) for a similar structure, a few key differences are found. This study confirms the results in Choe et al. (2008) that show that the fragility does not change drastically with a decrease of 10% in rebar diameter; however, there is a change in fragility due to removal of the concrete cover which is not seen in the previous research.

With regard to historic structures, any level of corrosion is significant because of the damaging effects that it could have on the historic fabric of the structure. If the corrosion is greater than approximately 10% of the rebar diameter (which may be likely in severe cases), then adequate repair and rehabilitation techniques must be utilized in accordance with the principles presented in this thesis.

The results of this study can be applied to structures beyond the single-bent RC bridge that is presented herein; however, the limitations of this research must be carefully considered. The results of other dynamic loading (railroad vibrations, for example) on RC structures subject to corrosion are expected to be similar to those seen in this study; however, the higher occurrence and lower magnitude of other dynamic loadings could lead to different results. A further study could be performed to verify these differences.

Additionally, future work should be done to confirm the effect of corrosion on the bond between the concrete and reinforcing steel. A decrease in bond strength is neglected in this study; however, it should be accounted for if it is determined to have a significant effect on the behavior of the structure. Additionally, this research could be extended to determine the change in shear capacity as the rebar diameter is decreased and the concrete cover is removed. Although the drift capacity is increased for the damaged analysis cases, the shear capacity should be reduced. Examining the effect of corrosion on shear capacity would also help confirm and quantify the change in structural strength due to corrosion. Additional work could also verify the results of this work by accounting for a greater reduction in the diameter of the reinforcing steel and a change in mechanical properties of the steel as it corrodes. Future work could also be done to account for more variability in the geometric parameters of the bridge; bridges with multiple columns and additional spans could reveal additional issues.

REFERENCES

Abrahamson, N.A. and Silva, W.J. (1997). "Empirical Response Spectral Attenuation Relations for Shallow Crustal Earthquakes." *Seismological Research Letters*, 68(1), 94-127.

Almusallam, A.A., Ahmad, S.A., Abdur, R.A., Dakhil, F.H., and Rasheeduzzafar. (1996). "Effect of Reinforcement Corrosion on Flexural Behavior of Concrete Slabs." *Journal of Materials in Civil Engineering,* 8(3), 123-127.

Al-Sulaimani, G.J., Kaleemullah, M., Basunbul, I.A., and Rasheeduzzafar. (1990). "Influence of Corrosion and Cracking on Bond Behavior and Strength of Reinforced Concrete Members." *ACI Structural Journal,* 87(2), 220-230.

American Concrete Institute (ACI). (2008). *Building Code Requirements for Structural Concrete (ACI 318-08) and Commentary (ACI 318R-08).* American Concrete Institute, Farmington Hills, MI.

American Petroleum Institute (API). (1993). "Recommended Practice for Planning, Designing, and Constructing Fixed Offshore Platforms – Load and Resistance Factor Design." *API Report No. RP2A-LRFD,* Washington, D.C.

American Society of Civil Engineers (ASCE). (2005). "Report Card for America's Infrastructure." *ASCE,* Reston, Virginia. http://www.asce.org/reportcard/2005-/index (Sept. 22, 2008).

Ball, J.C. (2007). "Electrochemical Treatment – Extending the Life of a Historic Viaduct Structure." *Structure Magazine,* October: 9-12.

Castel, A., Fancois, R., and Arliguie G. (2000). "Mechanical Behavior of Corroded Reinforced Concrete Beams – Part 1: Experimental Study of Corroded Beams." *Materials and Structures,* 33(9), 539-544.

Choe, D., Gardoni, P., Rosowsky, D., and Haukaas T. (2007a). "Probabilistic Capacity Models and Seismic Fragility Estimates for RC Columns Subject to Corrosion." *Reliability Engineering and System Safety,* 93(3), 383-393.

Choe, D., Gardoni, P., and Rosowsky, D. (2007b). "Closed-Form Fragility Estimates, Parameter Sensitivity, and Bayesian Updating for RC Columns." *Journal of Engineering Mechanics,* 133(7), 833-843.

Choe, D., Gardoni, P., Rosowsky, D., and Haukaas T. (2008). "Seismic Fragility Estimates for Reinforced Concrete Bridges Subject to Corrosion." *Structural Safety* (article in press).

Emmons, P. and Sordyl, D.J. (2006). "The State of the Concrete Repair Industry, and a Vision for Its Future." *Concrete Repair Bulletin,* July/August, 7-14.

Enright, M.P. and Frangopol, D.M. (1998). "Probabilistic Analysis of Resistance Degradation of Reinforced Concrete Bridge Beams under Corrosion." *Engineering Structures,* 20(11), 960-971.

Esmaeily, A. (2001). "USC_RC, Moment-Curvature and Force-Deflection Analysis of Reinforced Concrete Members." Kansas State University, Manhattan, KS. Software Version 1.0.4. http://www.usc.edu/dept/civil_eng/structural_lab/asad-/usc_rc.htm.

Gardoni, P., Kiureghian A.D., and Mosalam, K. (2002). "Probabilistic Capacity Models and Fragility Estimates for Reinforced Concrete Columns Based on Experimental Observations." *Journal of Engineering Mechanics,* 128(10), 1024-1038.

Ghandehari, M., Zulli, M., and Shah, S.P. (2000). "Influence of Corrosion on Bond Degradation in Reinforced Concrete." *Proceedings of the ASCE Engineering Mechanics Conference,* ASCE, Austin, TX, 1-15.

Huang, Q., Gardoni, P., and Hurlebaus, S. (2008). "Probabilistic Seismic Demand Models and Fragility Estimates for Reinforced Concrete Highway Bridges with One-Column Bent." *Journal of Structural Engineering,* (submitted).

Johnson, A.P. and Lee, S.K. (2004). "Soldier Field Stadium: Corrosion Mitigation for Historic Concrete." *APT Bulletin,* 35(2), 67-75.

Kunnath, S.K. (2003). "Inelastic Damage Analysis of Structural Systems (IDASS)." Davis, CA, Software Version 3.01.

Lawanwisut, W., Li, C.Q, and Aguiar, S.D. (2003). "Whole Life Assessment of Corrosion Affected Reinforced Concrete Structures." *Applications of Statistics in Civil Engineering.* Der Kiureghian, Madanat and Pestana (eds.), Millpress, Rotterdam: 573-580.

Lee, H.S., Kage, T., Noguchi, T., and Tomosawa, F. (2003). "An Experimental Study in the Retrofitting Effects of Reinforced Concrete Columns Damaged by Rebar Corrosion Strengthened with Carbon Fiber Sheets." *Cement and Concrete Research,* 33(4), 563-570.

Li, C.Q., Lawanwisut, W., and Zheng, J.J. (2003). "Time-dependent System Reliability of Deteriorating Reinforced Concrete Structures." *Applications of Statistics and Probability in Civil Engineering.* Der Kiureghian, Madanat and Pestana (eds.), Millpress, Rotterdam: 77-83.

Li, C.Q. (2003a). "Life-Cycle Modeling of Corrosion-Affected Concrete Structures – Propagation." *Journal of Structural Engineering* 129(6), 753-761.

Li, C.Q. (2003b). "Life Cycle Modeling of Corrosion Affected Concrete Structures – Initiation." *Journal of Materials in Civil Engineering.* 15(6), 594-601.

Luco, N. (2001). "Probabilistic Seismic Demand Analysis, SMRF Connection Fractures, and Near-source Effects." Ph.D. Dissertation, Dept. of Civil and Environmental Engineering, Stanford University, CA.

Mackie, K., and Stojadinović, B. (2003). "Seismic Demands for Performance-Based Design of Bridges." *PEER Report 2003/16,* Pacific Engineering Earthquake Research Center, University of California, Berkeley.

Malioka, V. and Faber, M.H. (2003). "Condition Indicators for Inspection and Maintenance Planning." *Applications of Statistics and Probability in Civil Engineering.* Der Kiureghian, Madanat and Pestana (eds.). Millpress, Rotterdam: 1101-1108.

Malioka, V. and Faber, M.H. (2004). "Modeling of the Spatial Variability for Concrete Structures." *Bridge Maintenance, Safety, Management, and Cost.* Watanabe, Frangopol, and Utsunomiya (eds.). Taylor and Francis Group, London: 825-826.

Mander, J.B., Priestley, M.J.N., and Park R. (1988). "Theoretical Stress-Strain Model for Confined Concrete." *Journal of Structural Engineering.* 114(8), 1804-1826.

National Association of Corrosion Engineers (NACE). (2002). "Corrosion Costs and Preventative Strategies in the United States." *Publication FHWA-RD-01-156.* Houston, TX, 1-12.

OpenSees Computer Software. (2008). http://opensees.berkeley.edu (Sept. 22, 2008).

PEER Strong Motion Database. (2008). http://peer.berkeley.edu/smcat (Sept. 22, 2008).

Penelis, G.G. (2002). "Structural Restoration of Historical Buildings in Seismic Areas." *Progress in Structural Engineering Materials,* 4(1), 64-73.

Ramamoorthy, S.K., Gardoni, P., and Bracci, J.M. (2006). "Probabilistic Demand Models and Fragility Curves for Reinforced Concrete Frames." *Journal of Structural Engineering.* ASCE, 132(10), 1563-1572.

Shome, N. (1999). "Probabilistic Seismic Demand Analysis of Nonlinear Structures," *Ph.D. Dissertation,* Dept. of Civil and Environmental Engineering, Stanford University, CA.

Sparks, P. (2006). *Preservation Texas Circuit Writer.* Preservation Texas, Vol. 8.

Stewart, M.G. and Rosowsky, D.V. (2001). "Corrosion, Deterioration, and Time-Dependent Reliability of Reinforced Concrete Bridge Decks." *Structural Engineering Research Report STR-97-01,* Clemson University, Clemson, SC.

Stewart, M.G. and Rosowsky, D. (1998). "Structural Safety and Serviceability of Concrete Bridges Subject to Corrosion." *Journal of Infrastructure Systems.* 4(4), 146-155.

Thomasen, S.E. (1995). "Seismic Strengthening of Historic Concrete Arch Bridges." *Transactions on the Built Environment,* WIT Press. 15(1), 77-84.

Val, D. (2007). "Deterioration of Strength of RC Beams due to Corrosion and Its Influence on Beam Reliability." *Journal of Structural Engineering.* ASCE, 133(9), 1297-1306.

Vu, K.A.T. and Stewart, M.G. (2000). "Structural Reliability of Concrete Bridges Including Improved Chloride-induced Corrosion Models." *Structural Safety,* 22(4), 313-333.

Wen, Y.K., Ellingwood, B.R., and Bracci, J.M. (2004). "Vulnerability Function Framework for Consequence-based Engineering." *DS-4 Technical Report*, Mid-America Earthquake Center, University of Illinois at Urbana-Champaign, Urbana, IL, 1-101.

APPENDIX A

ADDITIONAL LITERATURE REVIEW

The material in this appendix is intended to build upon the topics which are presented in the body of this thesis.

Strength

Al-Sulaimani et al. (1990) showed that the bond strength actually increases when corrosion levels are below one percent; however, with higher levels of corrosion, the bond strength steadily decreases until it is negligible. According to Al-Sulaimani et al. (1990), the initial increase in bond is justified because of the additional roughness created by the expanding rust products on the steel-concrete interface; however, over time these rust products begin to deteriorate and act more as a lubricating material. As the rebar ribs wear down and the corrosion products increase, the bond is lost at that interface. This work also determined that the cover-to-bar diameter ratio is a good parameter for measuring the corrosion protection level: a higher ratio is more desirable (Al-Sulaimani et al. 1990). This research showed that bond strength is relatively substantial when no concrete confinement is present.

Although this research makes no distinction between different sources of corrosion, many research projects have focused on this issue. In particular, Val (2007) examined the effects of both general and pitting corrosion on the flexural and shear strength of RC beams; the results showed that most beams subject to pitting corrosion

failed in shear as a result of the reduction in the smaller cross-sectional areas of the transverse reinforcement (Val 2007). It concluded that when analyzing structures subject to corrosion, the shear resistance of the beams should be considered with utmost importance, especially if pitting corrosion is present.

Vu and Stewart (2000) reported a reduction of approximately ten percent in flexural strength and less than five percent in shear capacity for a typical traffic bridge subject to corrosion because of close proximity to an atmospheric marine zone (as similar to this work). In this work, the flexural and shear capacities were noticeably lower for specimens with "poor" concrete material properties; the concrete is considered “poor” if it has a low concrete compressive strength (3.6 ksi) and limited concrete cover (approximately 1 inch) (Vu and Stewart 2000). This work assumes an unconfined concrete compressive strength of 4 ksi and a cover thickness of 3.0 inches which places it near the “poor” category. In contrast to the work performed by Val (2007), Vu and Stewart (2000) stated that flexural failure is more likely for specimens undergoing corrosion than shear failure.

Lee et al. (2003) stated that extremely corroded bars could fail in a brittle manner due to shear under seismic loads. Lee et al. (2003) have shown that the deterioration of the structural capacity of RC columns damaged by corrosion and strengthened with carbon fiber sheets (CFS) was caused mostly by the loss of rebar mechanical properties and the loss of confinement that occurs when the cover spalls. This study relates to this research because this work will consider a case with full concrete cover and only partial rebar diameters; this case represents specimens that have been subject to corrosion, lost

concrete cover, and then been retrofitted with CFS to replace the cover. This study also examined the effects of corrosion on columns, as opposed to beams; therefore, the results are more applicable to this work. Lee et al. (2003) concluded that the reduction in strength and deformability of a RC column with corrosion was a result of rebar fracture caused by local corrosion, a decrease in mechanical properties of the rebar, and a decrease in the confining effect of the concrete once the cover spalled off.

Enright and Frangopol (1998) considered the time variant loss of strength due to corrosion of steel rebar. This study showed that an increase in the mean concrete cover depth results in an increase in the mean corrosion initiation time; thus, the corrosion process will take longer to begin and the structure will retain its original strength for a longer period of time (Enright and Frangopol 1998). This work shows a decrease in rebar diameter of approximately 17% over 80 years resulting from corrosion in the deck due to runoff and/or traffic spray (Enright and Frangopol 1998).

Stiffness

Castel et al. (2000) studied the effect of corrosion on both strength and stiffness. In this study, the results showed that service behavior changes drastically with degradation of steel in the tensile region. More specifically, a loss of bending stiffness occurred as a result of the corrosion which could not be explained simply by a change in steel cross-sectional area. The ductility at the ultimate load state was also shown to be affected by the loss of steel cross-sectional area caused by corrosion. The results of this study showed that the beams with corrosion in the tensile zone showed a greater decrease in stiffness than those with corrosion in the compression zone. The stiffness loss obtained

was much greater than the amount expected from a decrease in steel cross-sectional area alone; therefore, this work concluded that a decrease in bond strength at the concrete-steel interface resulting from corrosion can contribute for up to about 50% of the stiffness reduction that is measured (Castel et al. 2000). Based on this work, the relationship between bond strength and structural stiffness is significant; however, the decrease in bond strength will not be considered in this work.

Li et al. (2003) also studied the importance of corrosion-induced stiffness deterioration and its effect on the reliability of structural systems. This study found that the load redistribution and the failure modes seen in a structure are dependent on the relative stiffnesses of the structural elements (Li et al. 2003). A stiffness deterioration function used within this study was developed based on a regression of previous test results.

Historic Preservation

Many non-destructive techniques can be used to help alleviate the problems caused by corrosion in historic structures. One example is the usage of carbon fiber sheets (CFS) which is an effective way of strengthening the shear capacity of a column while helping to prevent cracking and improving ductility (Lee et al. 2003). The strengthening effect of the CFS mainly results from the confining effects that they provide.

The concept of life-cycle modeling of RC structures subject to corrosion is a topic which has gained more attention recently. Work performed by Li (2003a, 2003b) considered both the initiation and propagation stages of rebar corrosion in RC structures

in order to try to assess the performance of a structure's entire service life. These performance-based models will ideally be used to analyze newly built RC structures to help decide when to inspect, repair, strengthen, replace, or demolish aging structures (Li 2003a). This work is beneficial for both engineers and property managers in order to determine a schedule for maintenance and repair (Li 2003b).

Another paper which attempted to use a reliability approach to create a life-cycle behavior assessment of RC structures subject to corrosion was done by Lawanwisut et al. (2003). This work studied the different "lifetimes" of a structure and determines the probability of attaining each lifetime (Lawanwisut et al. 2003). This work could be used to help engineers and property managers make confident decisions relating to repairs and rehabilitations of corroded RC structures.

Fragility

In addition to the changes in the strength and stiffness behaviors of RC structures subjected to corrosion, changes in the fragility resulting from corrosion should be examined as well. By studying the nonlinear response of a structure subjected to dynamic loadings, the effect of corrosion on the structural fragility can be investigated. The most common type of dynamic loading for the bridge structure considered in this work is seismic activity; this will be the main focus of this work. While the effect of bond loss on the hysteretic behavior of this structure is not a direct part of this work, it should be accounted for in future work.

One study that examined the effects of a cyclic horizontal loading test on a RC column was performed by Lee et al. (2003). Column specimens with varying degrees of corrosion were subjected to cyclic loading and the resulting load-deformation curves were given. These graphs show that increasing levels of corrosion alter the load-deformation curves by initially stiffening the members (rust products slightly increase the concrete confining pressure) and then subsequently softening the curves. Also, the cumulative energy absorption for specimens with larger degrees of corrosion was smaller, even when the extent of the deformation was the same. For this study, the specimens involved were only subject to approximately ten cycles of loading.

Two studies by Choe et al. (2007a, 2008) also considered the effect of seismic loading in RC bridges subject to corrosion. The first study (Choe et al. 2007a) developed probabilistic shear force and drift capacity models considering corrosion effects. The second study (Choe et al. 2008) developed fragility estimates for RC bridges subject to corrosion.

APPENDIX B

DEVELOPMENT OF EARTHQUAKE RECORD BINS

The process used to determine which six earthquakes should be used in each bin for the dynamic analysis within OpenSees will be explained here for reference. The general idea behind this approach is to compare the median value of the spectral acceleration curves from a given suite of earthquakes to a set of baseline acceleration spectra curves from the attenuation law (Abrahamson and Silva 1997). The earthquake records used in all bins are obtained directly from the PEER Strong Motion Database (2008), and the data for three orthogonal directions (two horizontal and one vertical) is used for each earthquake record. All earthquake records are formatted to have equally spaced response data every 0.02 seconds.

The first step is to develop the baseline spectral acceleration curves from the attenuation law results given by Abrahamson and Silva (1997). One curve is developed for each of the five bins, and these curves are shown in Fig. B1.

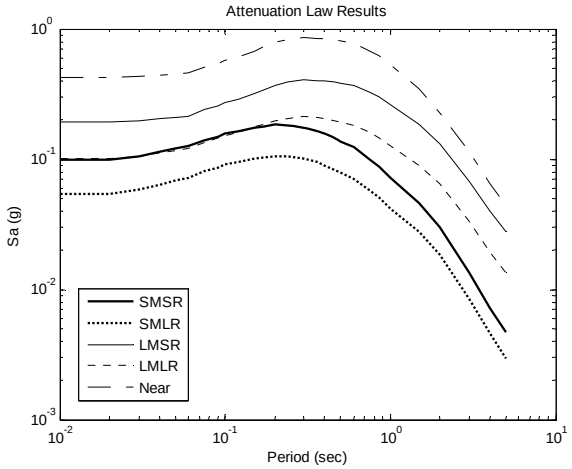

Fig. B1. Acceleration Response Spectra, (Attenuation Law)

The attenuation law curves represent bins with a reverse fault type and deep soil. However, since fault types vary for all earthquakes, a quick study was performed to determine that the attenuation law results do not change significantly based on this factor. It was found that the soil type (deep vs. shallow/rock soil) does influence the results significantly; therefore, only deep soil results are considered for this research.

Additionally, only the horizontal component results are checked in this study, and for each earthquake, the average of the two orthogonal horizontal direction records are compared against the attenuation law. Abrahamson and Silva (1997) also present sufficient information to repeat this process for the vertical earthquake records; however, that is not done for this research.

Once the baseline attenuation law spectral acceleration curves are developed for each bin, a series of earthquake records from the PEER Strong Motion Database (2008) are averaged and compared. To begin, a list of twenty earthquake records for each bin is

obtained from Huang et al. (2008). A group of six earthquake records is selected for each bin from the initial twenty earthquakes in order to decrease the computational time involved in running the dynamic analysis within OpenSees. To ensure that a representative sample of earthquakes is obtained for each bin, the median spectral acceleration curve for the six records is compared against the attenuation law curve for each respective bin. In addition to matching the median spectral accelerations with the attenuation law curves, the standard deviation of the six PEER earthquake records is tracked. While no specific maximum standard deviation value is given for the attenuation law, all standard deviations are kept less than approximately 0.2 (Shome 1999; Huang et al. 2008). The average error in the standard deviation, defined as the average of the difference between the standard deviation of the PEER record spectral acceleration values and the standard deviation of the attenuation law acceleration values for each period, is also found for each bin. Table B1 shows a comparison of these errors, in percent, for each bin with six earthquakes and with twenty earthquakes; as shown, the two different sized bins have comparably small errors, supporting the claim that using six records per bin is appropriate.

Table B1. Average Errors in Standard Deviation

Bin	6 Earthquakes	20 Earthquakes
SMSR	7.77 %	7.39 %
SMLR	8.74 %	6.42 %
LMSR	7.15 %	3.44 %
LMLR	10.2 %	9.93 %
Near	5.65 %	4.36 %

Once the previous analysis process is complete, thirty earthquakes have been chosen for the OpenSees dynamic analysis (six earthquakes per bin, five bins). Fig. B2 shows the median acceleration response spectra curves for each bin with six earthquakes. This figure is directly comparable to Fig. B1.

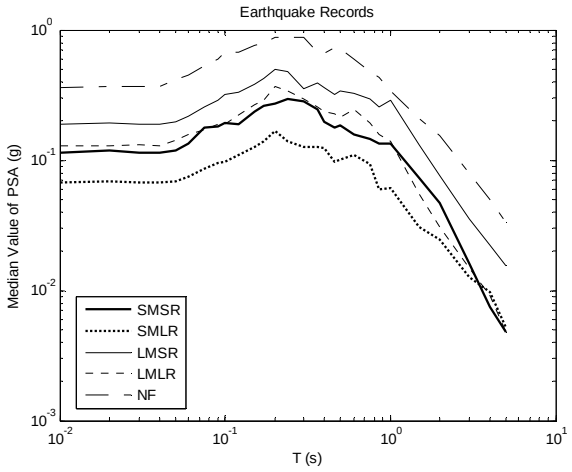

Fig. B2. Acceleration Response Spectras, (bins with 6 records)

Scaled Records

In addition to the five previously mentioned earthquake bins (SMSR, SMLR, LMSR, LMLR, and Near), ten more bins are developed for this study. Since the five initial bins resulted in limited non-linear behavior of the bridge, the earthquake records in each bin are scaled up by two sets of factor in order to induce additional non-linear results. For the first set of scaled up bins, the earthquake records within the ordinary bins (SMSR, SMLR, LMSR, and LMLR) are all scaled up by a factor of six while the records within the near field bin are scaled up by a factor of two. In the second set of scaled bins, the

ordinary bins are scaled by a factor of eleven while the near field bin is scaled up by a factor of four. These factors are determined by ensuring that the median and the "one sigma level" values for the elastic spectral displacements are approximately the same for both the near field and ordinary bins (Luco, 2001). Once the original bins have been scaled up, the ten new bins are added to the analysis (SMSR_sc6, SMLR_sc6, LMSR_sc6, LMLR_sc6, Near_sc6, SMSR_sc11, SMLR_sc11, LMSR_sc11, LMLR_sc11, and Near_sc11).

The "one sigma level" values referred to above are calculated by multiplying the median, m, by the exponential of the standard deviation of the natural logs of the data; this is shown in the following equation (Luco 2001).

$$\sigma = m \cdot e^{\sqrt{\frac{1}{n-1}\sum_{i=1}^{n}\left[\ln(x_i)-\ln(m)\right]^2}} \tag{B1}$$

Matlab is used in order to check that this requirement is met for the scaled up bins used in this analysis. Fig. B3 shows the median and "one sigma level" curves for the spectral displacements of the five bins, with six records each, for each of the two sets of scale factors noted previously. The values for the ordinary bins and the near field bins are very close; therefore, these scale factors meet the requirements set forth by Luco (2001).

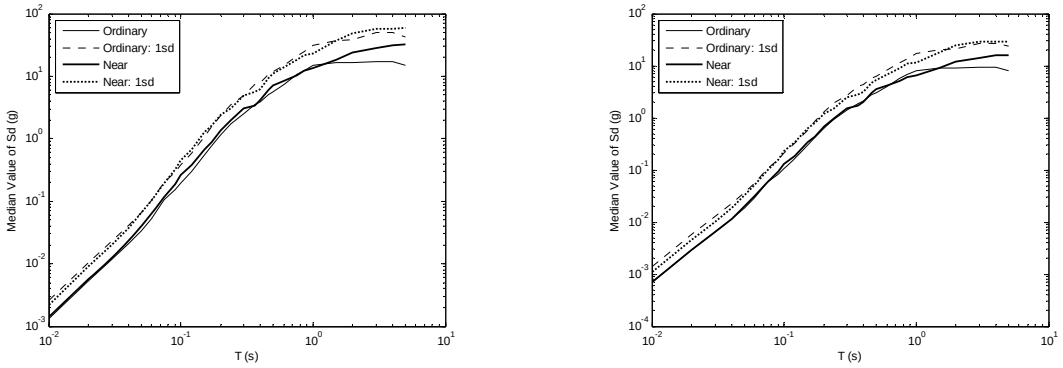

(a) Ordinary SF = 6; Near SF = 2 **(b)** Ordinary SF = 11; Near SF = 4

Fig. B3. Verification of Scale Factors

Earthquake Records

A tabulated summary of each of the thirty earthquakes used in the dynamic analysis within OpenSees is given in Table B2. Again, all earthquake records presented here are obtained from the PEER Strong Motion Database (2008).

Table B2. Earthquake Records per Bin

Record ID	Earthquake	M	R	GM	USGS	Station	Record/ Component	HP (Hz)	LP (Hz)	PGA (g)	PGV (cm/s)	PGD (cm)
SMSR												
P0348	Coalinga 1983/05/02 23:42	6	28	C	-	36457 Parkfield - Fault Zone 16	COALINGA/H-Z16-UP	0.2	30	0.061	6.5	1.92
P0361	Coalinga 1983/05/02 23:42	6	30	C	-	36448 Parkfield - Vineyard Cany 1W	COALINGA/H-VC1-UP	0.5	28	0.068	6.1	1.49

Table B2. Continued

Record ID	Earthquake	M	R	GM	USGS	Station	Record/ Component	HP (Hz)	LP (Hz)	PGA (g)	PGV (cm/s)	PGD (cm)
P0525	N. Palm Springs 1986/07/08 09:20	6	30	C	B	22170 Joshua Tree	PALMSPR/JOS-UP	0.5	36	0.04	3.6	0.6
P0617	Whittier Narrows 1987/10/01 14:42	6	17	C	C	90068 Covina - S Grand Ave	WHITTIER/A-GRA-UP	0.33	25	0.064	3.1	0.46
P0323	Coalinga 1983/05/02 23:42	6	26	D	-	46314 Cantua Creek School	COALINGA/H-CAK-UP	0.2	26	0.094	5.1	1.86
P0450	Morgan Hill 1984/04/24 21:15	6	15	D	C	47380 Gilroy Array #2	MORGAN/G02-UP	0.2	37	0.578	10.8	0.92
SMLR												
P0328	Coalinga 1983/05/02 23:42	6	44	C	-	36410 Parkfield - Cholame 3W	COALINGA/H-C03-UP	0.2	27	0.034	4.5	1.46
P0689	Whittier Narrows 1987/10/01 14:42	6	38	C	C	90044 Rancho Palos Verdes - Luconia	WHITTIER/A-LUC-UP	0.55	21.5	0.017	0.9	0.11
P0324	Coalinga 1983/05/02 23:42	6	42	D	-	36452 Parkfield - Cholame 1E	COALINGA/H-C01-UP	0.5	30	0.059	6.6	1.82
P0189	Imperial Valley 1979/10/15 23:16	7	32	D	C	5052 Plaster City	IMPVALL/H-PLS-UP	0.1	40	0.026	2.4	0.98
P0455	Morgan Hill 1984/04/24 21:15	6	30	D	B	1377 San Juan Bautista	MORGAN/SJB-UP	0.1	21	0.052	2.7	1.35

Table B2. Continued

Record ID	Earthquake	M	R	GM	USGS	Station	Record/ Component	HP (Hz)	LP (Hz)	PGA (g)	PGV (cm/s)	PGD (cm)
P0527	N. Palm Springs 1986/07/08 09:20	6	38	D	-	22T13 Landers Fire Station	PALMSPR/LDR-UP	0.5	40	0.055	2.4	0.42
LMSR												
P0933	Northridge 1994/01/17 12:31	7	18	C	B	90058 Sunland - Mt Gleason Ave	NORTHR/GLE-UP	0.1	30	0.193	11.6	2.35
P0975	Northridge 1994/01/17 12:31	7	23	C	B	24607 Lake Hughes #12A	NORTHR/H12-UP	0.13	46	0.121	4	2.59
P0058	San Fernando 1971/02/09 14:00	7	26	C	-	125 Lake Hughes #1	SFERN/L01021	0.5	35	0.145	17.3	2.88
P0814	Landers 1992/06/28 11:58	7	23	D	B	12149 Desert Hot Springs	LANDERS/DSP-UP	0.07	23	0.167	9.9	3.71
P0737	Loma Prieta 1989/10/18 00:05	7	16	D	C	57382 Gilroy Array #4	LOMAP/G04-UP	0.2	42	0.159	14.6	5.1
P0884	Northridge 1994/01/17 12:31	7	26	D	C	24303 LA - Hollywood Stor FF	NORTHR/HOL360	0.2	23	0.358	27.5	3.04
LMLR												
P0918	Northridge 1994/01/17 12:31	7	36	C	C	24271 Lake Hughes #1	NORTHR/LH1-UP	0.12	23	0.099	7	3.43

Table B2. Continued

Record ID	Earthquake	M	R	GM	USGS	Station	Record/ Component	HP (Hz)	LP (Hz)	PGA (g)	PGV (cm/s)	PGD (cm)
P0921	Northridge 1994/01/17 12:31	7	38	C	C	24055 Leona Valley #5 - Ritter	NORTHR/LV5-UP	0.2	23	0.097	11.6	2.53
P0999	Northridge 1994/01/17 12:31	7	39	C	C	90095 Pasadena - N Sierra Madre	NORTHR/SMV-UP	0.4	30	0.141	8.4	0.57
P0773	Loma Prieta 1989/10/18 00:05	7	36	D	-	58264 Palo Alto - 1900 Embarc.	LOMAP/PAE-UP	0.2	50	0.08	7.3	3.33
P0931	Northridge 1994/01/17 12:31	7	35	D	B	24401 San Marino, SW Academy	NORTHR/SMA-UP	0.6	23	0.083	3.7	0.41
P0944	Northridge 1994/01/17 12:31	7	38	D	C	24576 Anaverde Valley - City R	NORTHR/ANA-UP	0.2	46	0.044	4.7	1.7
Near												
P0816	Landers 1992/06/28 11:58	7	12	C	B	22170 Joshua Tree	LANDERS/JOS-UP	0.07	23	0.181	15	9.39
P0541	N. Palm Springs 1986/07/08 09:20	6	7.3	C	A	5072 White-water Trout Farm	PALMSPR/WWT-UP	0.5	40	0.471	13.4	1.02
P1005	Northridge 1994/01/17 12:31	7	7.1	C	C	77 Rinaldi Receiving Sta	NORTHR/RRS-UP	null	null	0.852	50.7	11.65

Table B2. Continued

Record ID	Earthquake	M	R	GM	USGS	Station	Record/ Component	HP (Hz)	LP (Hz)	PGA (g)	PGV (cm/s)	PGD (cm)
P0553	Chalfant Valley 1986/07/21 14:42	6	9.2	D	-	54171 Bishop - LADWP South St	CHALFANT/A-LAD-UP	0.1	40	0.14	6.7	2.25
P0006	Imperial Valley 1940/05/19 04:37	7	8.3	D	C	117 El Centro Array #9	IMPVALL/I-ELC-UP	0.2	15	0.205	10.7	9.16
P0736	Loma Prieta 1989/10/18 00:05	7	14	D	C	47381 Gilroy Array #3	LOMAP/G03-UP	0.1	50	0.338	15.5	7.03

APPENDIX C

STRENGTH AND STIFFNESS VERIFICATION DATA

Stiffness Verification

The relative bridge stiffnesses between the four cases are verified by comparing the static pushover results from OpenSees with simple hand calculations. The ratio of the moment of inertia of the concrete cross-section with the cover removed is compared to the moment of inertia of the full concrete cross-section by hand. This calculation is shown in the following equation,

$$\frac{I_{NC}}{I_{FC}} = \frac{\left(D_g - \left(2 \cdot spall\right)\right)^4}{\left(D_g\right)^4} \tag{C1}$$

where I_{NC} and I_{FC} refer to the moment of inertia of the cross-section with no cover and full cover, respectively, D_g refers to the gross column diameter, and $spall$ refers to the thickness of the concrete cover that has been removed. For this research, D_g is 63 in and $spall$ is 3 in; therefore, the ratio of the stiffnesses with this hand calculation is 0.67. This ratio means that an approximately 33% decrease in stiffness is expected for this case.

A bilinear analysis is then performed on the static pushover results obtained from OpenSees for all four bridge cases in both the longitudinal and transverse directions. An example of the results of the bilinear analysis is given in Fig. C1 for the FCFB case in the longitudinal direction.

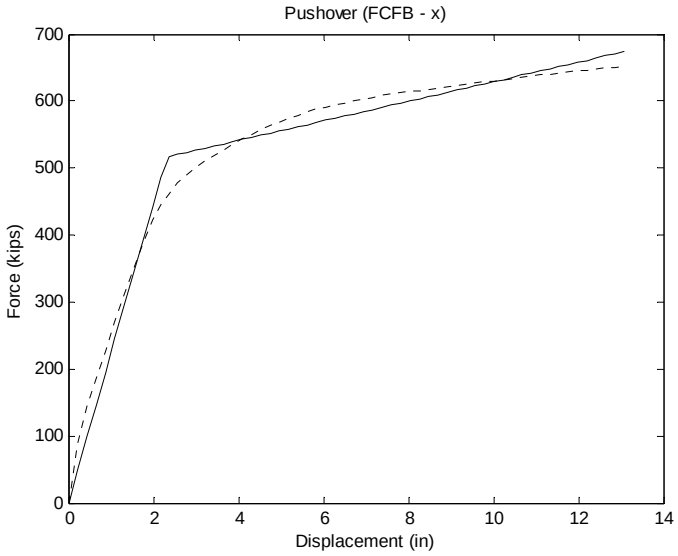

Fig. C1. Static Pushover Bilinear Analysis

The results of the bilinear analysis give an equivalent stiffness value for each case, and these stiffnessses are presented in Table C1. The bilinear stiffness values are easily verified by checking the slope of the elastic portion of each curve.

Table C1. OpenSees Bilinear Pushover Stiffnesses

Case	Longitudinal Stiffness (k/in)	Transverse Stiffness (k/in)
FCFB	224.16	177.66
FCPB	210.69	167.72
NCFB	167.27	143.01
NCPB	151.31	133.82

From the results given in Table C1, ratios between the damaged and undamaged columns can be determined. The ratio between the NCFB and FCFB cases in the

longitudinal direction is 0.75, and the ratio between the NCPB and FCPB cases in the same direction is 0.72. The pushover results show that a decrease in concrete cover corresponds to a decrease in stiffness of approximately 27%. This is slightly less than the 33% decrease expected with the simplified hand calculation; however, the hand calculation does not account for any effects from the bridge deck or the confined concrete.

Strength Verification

The relative strength differences between the four bridges cases are also verified using simple hand calculations and the OpenSees static pushover results. Fig. C2 shows the results of a static pushover analysis performed in the longitudinal direction within OpenSees.

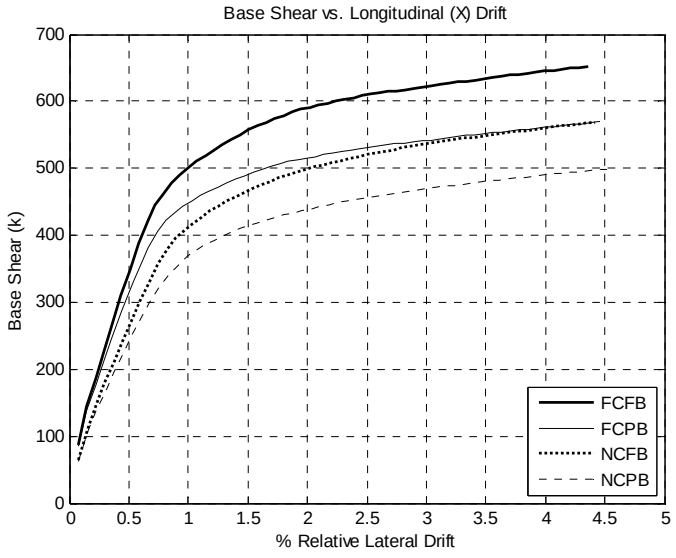

Fig. C2. OpenSees Longitudinal Static Pushover Results

The maximum base shear values at a relative drift of 4.5% are compared to determine the differences in strength between the four cases. Relative drift refers to the difference in the drift between the top and the bottom of the column. From these results, the strength reduction between the FCFB and FCPB cases is determined to be 13.8%. Similarly, the reduction in strength between the NCFB and NCPB cases is calculated to be 12.5%. These calculations are shown below,

$$\left(1-\frac{V_{FCPB}}{V_{FCFB}}\right)\cdot 100=\left(1-\frac{560}{650}\right)\cdot 100=13.8\% \tag{C2}$$

$$\left(1-\frac{V_{NCPB}}{V_{NCFB}}\right)\cdot 100=\left(1-\frac{490}{560}\right)\cdot 100=12.5\% \tag{C3}$$

where V_{FCPB} refers to the base shear force at 4.5% drift for the FCFB pushover case; similar notation is used for the base shear values corresponding to the FCPB, NCFB, and NCPB cases.

APPENDIX D

MOMENT CURVATURE CALCULATIONS

PCA Column

The values from the moment-curvature analysis given in Section 4.1 based on the PCA Column results are calculated from the axial load – moment interaction diagram. These are not exactly accurate values for the OpenSees model since the PCA Column analysis does not account for strain hardening in the steel or non-linear behavior like; however, these results should be relatively close to those obtained from OpenSees. Table D1 presents all of the material and section properties input into PCA Column.

Table D1. PCA Column Properties

Property	Value
f_c'	4 ksi
E_c	3605 ksi
f_c	3.4 ksi
β_1	0.85
f_y	65 ksi
E_s	29,000 ksi
A_g	3,117.25 in^2
I_x	773,272 in^4
I_y	773,272 in^4
Clear Cover	3.0 in
Transverse Spacing	3.19 in
ρ_{long}	2.0 %

The definitions for the moment and curvature values are shown in Fig. D1 where EI_e is defined as $0.7EI_g$.

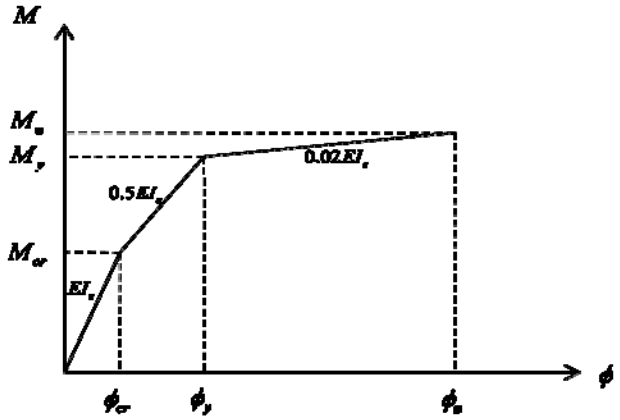

Fig. D1. PCA Column Moment-Curvature Relationship

OpenSees

The values presented for the moment-curvature analysis in Section 4.1 based on the OpenSees results are calculated following the procedure given in Gardoni et al. (2002). Fig. D2 shows the definition of each parameter, and it is clear that the values are defined differently the PCA Column results.

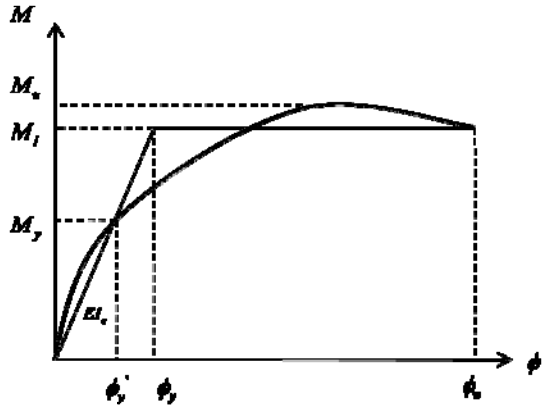

Fig. D2. OpenSees Moment-Curvature Relationship

APPENDIX E

STATIC PUSHOVER COMPARISON

To help verify the static pushover results obtained from OpenSees, two comparison programs, IDASS (Kunnath 2003) and USC_RC (Esmaeily 2001), are utilized. More information about these two models is presented here for reference.

IDASS

First of all, the IDASS model only accounted for a single column with the mass lumped at one node at the top. The input data used in the IDASS model came directly from the PCA Column interaction diagram shown previously. In other words, the values for M_{cr}, M_y, M_{ult}, ϕ_y, and ϕ_{ult} from PCA Colum are all manually input into the program; therefore, the graphical pushover results shown for IDASS match the PCA column results. A single column with a fully fixed base is created in IDASS, and a displacement controlled, monotonic pushover analysis is run.

Within IDASS, the column material properties are defined using a tri-linear degrading hysteretic model with a stiffness degrading coefficient (PARAM1) of 0.7, an energy-based strength decay factor (PARAM2) of 0.05, a ductility-based strength decay factor (PARAM3) of 0.0, and a target slip or crack closing parameter (PARAM4) of 0.7 (Kunnath 2003). Fig. E1 (a) through (c) show the significance of each parameter as well as how IDASS accounts for stiffness and strength degradation in addition to the effect of slip. All three figures are obtained directly from Kunnath (2003).

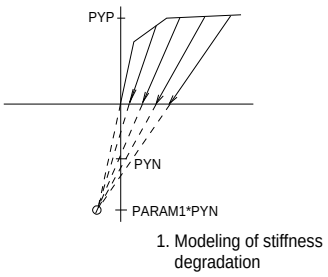

(a) Stiffness Degradation

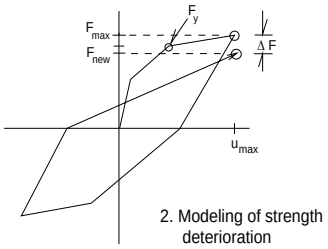

(b) Strength Degradation

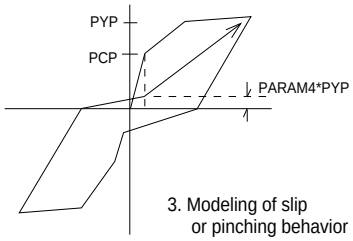

(c) Reinforcement Slip

Fig. E1. IDASS Modeling Assumptions

In the previous figures, PYP refers to the positive yield moment, PYN refers to the negative yield moment, and PCP refers to the positive cracking moment. The following expression is used to determine the loss of strength for this material model where μ represents the curvature ductility and Λ represents the total hysteretic energy dissipated (Kunnath 2003).

$$\Delta F = F_{\max}\left(PARAM2 \cdot \Lambda + PARAM3 \cdot \mu\right) \tag{E1}$$

The rigid zones for the IDASS column model are set as 0.0 at the top and bottom, and the column length used is 25 ft. The stiffness of the column before cracking is set as

$I_{eff} = 0.7EI_g$, the stiffness from cracking to yielding is $0.5I_{eff}$, and the stiffness beyond yielding is set as $0.02I_{eff}$. The values for the material properties used in Table E1; these values are for the FCFB case.

Table E1. IDASS Properties

Property	800 kips
E	29,000 ksi
I_g	773,272 in^4
A	3117 in^2
G	1502 ksi
EI_{eff}	1,951,349,170 ksi
EA/L	37,459 k/in
GA	4,682,362 k

While the IDASS column model is similar to the bridge column modeled in OpenSees, there are some modeling differences. First of all, the IDASS model assumes a lumped mass at the top of the column as opposed to the distributed mass modeled in OpenSees. Additionally, different reinforcing steel models are assumed. The OpenSees model also accounts for the confined concrete using the model proposed by Mander et al. (1988) while IDASS does not make this distinction. Since a full, three-dimensional bridge could not be easily modeled in IDASS, a single column with a fixed base is modeled; the OpenSees model accounts for a pile foundation, a full deck, and rigid abutments. The last major difference between the two models is that the definition of the "delta" value assumed when accounting for the second order P-Δ effects varies.

USC_RC

USC_RC is a fiber model based program, and the analysis performed is a monotonic lateral displacement pushover. This program modeled a single circular column with a fully fixed base. Although the steel material properties used in USC_RC are slightly different than those used in OpenSees, the concrete material behavior is quite similar because it uses the confined concrete model proposed by Mander et al. (1988). Fig. E2 and Fig. E3 show the steel and concrete stress-strain curves, respectively, used in USC_RC (Esmaeily 2001).

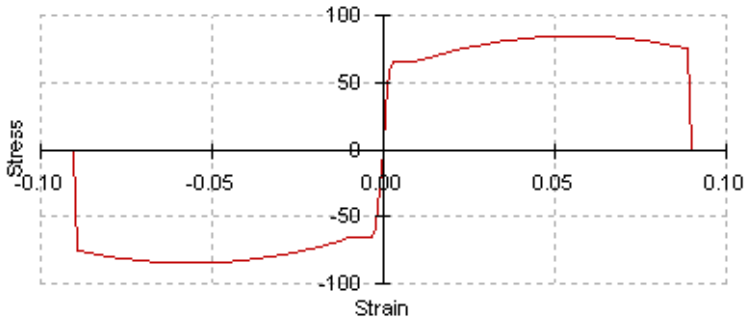

Fig. E2. USC_RC Steel Stress-Strain

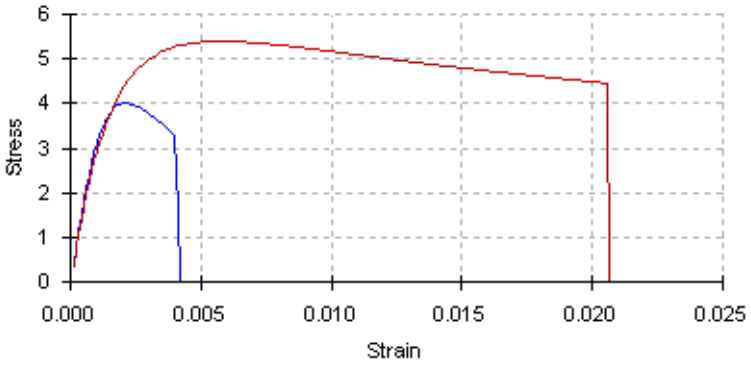

Fig. E3. USC_RC Concrete Stress-Strain

The input parameters used within USC_RC are shown in Table E2 below. These values are applicable to the FCFB case only.

Table E2. USC_RC Input Parameters

Property	Value
D	63 in
Cover	3 in
$f_c^{'}$	4 ksi
E	29,000 ksi
f_y	65 ksi
A_l	1.56 in^2
N	40 bars
A_t	0.44 in^2
S	4.49 in

The parameters in Table E2 are defined as follows: D is the diameter of the gross concrete cross-section, *Cover* is the clear cover distance from the edge of the concrete to the transverse steel, $f_c^{'}$ is the unconfined concrete compressive strength, E is the modulus of elasticity of the reinforcing steel, f_y is the strength of the reinforcing steel, A_l is the area of one longitudinal rebar, N is the number of longitudinal rebars, A_t is the area of one transverse rebar, and S is the spacing of the transverse reinforcement. These values correspond directly with those used within OpenSees.

APPENDIX F

MODAL ANALYSIS STUDY

The results for the fundamental bridge periods from seven different sources are compared in order to determine the most accurate values. The seven sources are each described in this Appendix.

OpenSees eigen command

The first method used to determine the modal frequencies and mode shapes is using an eigen-analysis function within OpenSees. This function is referred to as the "eigen" command. Both the roller abutment and the Caltrans abutment cases are analyzed using this method. For this method, the modal frequencies and eigenvectors are calculated directly by OpenSees, and the modal periods are then calculated by taking the inverse of the frequency values (in Hz). In order to determine which mode shape corresponded to each frequency, the eigenvector data from OpenSees is imported into Matlab and then plotted. According to the mode shapes, the first modal frequency for both the roller and Caltrans abutment cases corresponded with vertical motion of the column. The second mode shape for the roller abutment case is torsion in the column; however, the Caltrans abutment case showed longitudinal displacement for the second mode. The third mode for both the roller and Caltrans abutment cases is displacement in the transverse direction. The fourth mode shape for the roller abutment case is longitudinal displacement, and the fourth mode shape for the Caltrans abutment case is torsion in the column. The values of the periods for the first four modes of each abutment model as

well as a short description of the corresponding mode shapes are given in Table F1. The fifth through eighth modal periods and corresponding mode shapes are also obtained; however, they are not important for this comparison. It is curious to see that the periods obtained for the Caltrans abutment in the vertical and longitudinal directions are very similar to the periods obtained in the longitudinal and transverse directions, respectively, from some of the more reliable methods of modal analysis (presented later in this section).

Table F1. OpenSees "eigen" Periods (sec)

Mode	Caltrans	Roller
Longitudinal	0.2982	0.0909
Transverse	0.1816	0.6424
Vertical	0.6061	1.6939
Torsion	0.1060	0.7422

Fig. F1 (a) through (d) shows the mode shapes that are referred to in Table F1. The vertical shape has an unexplainably large deflection of the deck. The longitudinal and transverse mode shapes look as expected, and the torsion in the column is represented by the deck twisting. Each mode shape in Fig. F1 has three subplots which correspond to the shape of the deck, the column, and the pile (from top to bottom).

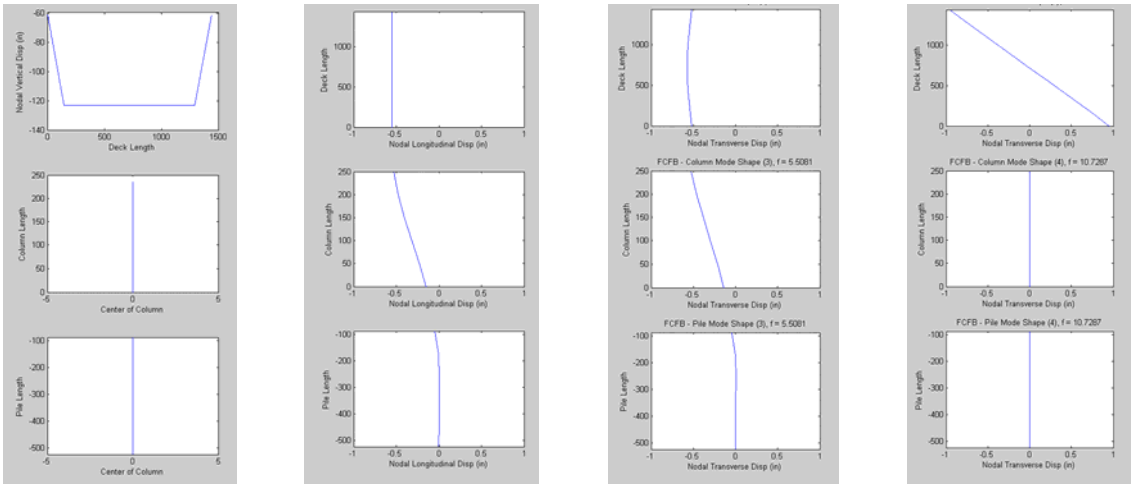

(a) Vertical **(b)** Longitudinal **(c)** Transverse **(d)** Torsion

Fig. F1. OpenSees Mode Shapes

These mode shapes show the motion of the deck, column, and pile; the mode shapes of the abutments can be found as well, but they are not presented here. One unique result from this analysis is that the vertical mode shape changed as a function of the gravity load applied on the structure. For the case shown above, the deck self weight is distributed based on the tributary area of all nodes on the deck; therefore, the two end nodes received half of the applied weight that the interior nodes received. This is shown in the deflected shape; however, the deflected shape is not expected to change based on the static loading. The mode shapes are expected to be dependent on the mass and stiffness of the structure only, not the applied loading. Additionally, the vertical column motion is not expected to be the dominant mode of vibration for this structure; however, both the roller and Caltrans abutment cases showed this to be true. Therefore, the results given by the "eigen" command within OpenSees are presented with skepticism and

additional methods of determining the modal periods and corresponding mode shapes are performed.

ETABS

The second modal analysis performed is done using the commercial, building design software called ETABS. Only the roller abutment case is modeled in ETABS because of the complex nature of modeling the springs within the Caltrans abutment. Another limitation in the ETABS computer model is that the beam and column elements are modeled elastically; a nonlinear analysis is not performed. However, even with the stated limitations, the ETABS model is used to determine the order of the modes and a rough estimate of the expected modal frequencies and periods. The ETABS model is created using the same geometric layout and member masses and cross-sections used in the OpenSees analysis. The first four modal periods determined using the ETABS model, along with descriptions of the corresponding mode shapes, are given in Table F2.

Table F2. ETABS Periods (sec)

Mode	Caltrans	Roller
Longitudinal	-	0.4509
Transverse	-	0.5561
Vertical	-	-
Torsion	-	2.9622

As expected, the vertical column motion does not show up within the first four modes of the structure; actually, ETABS presented twelve mode shapes and frequencies, and the vertical column motion is not present at all. It can be seen that the order of the

first three modes from ETABS is the same as the first three modes for the OpenSees "eigen" case with the roller abutment (assuming the vertical column motion mode is neglected). However, the values for the periods are significantly different.

Matlab FFT (Fast Fourier Transform) command

Another method used to determine the modal periods for the longitudinal, transverse, and vertical bridge motions is a Fast Fourier Transform (FFT) analysis. In order to use the FFT analysis, free vibration acceleration response data from the bridge structure is needed. Data from the first three seconds of an arbitrary earthquake record is used to induce vibration in the structure, and the acceleration response in the longitudinal, transverse, and vertical directions is recorded with a time step of 0.001 sec. at each node of the deck. The first three seconds of the response data is then truncated so that only the free vibration response remained. Because the response is obtained directly from OpenSees, this analysis is performed for both the Caltrans and the Roller abutment cases.

This free vibration acceleration time history for each direction is then input into Matlab in order to perform the FFT. The FFT command built into Matlab is used to transform the time history data into the frequency domain in order to determine the fundamental period(s). Each peak in the frequency domain plot obtained from the FFT denotes a fundamental frequency for the structure. Usually multiple peaks are developed (which represent the multiple modal frequencies of the structure); however, for this particular case only the first mode is excited in each direction (i.e. only one peak is

shown). The periods determined from the FFT analysis for both the Caltrans and roller abutment cases are shown in Table F3.

Table F3. Matlab FFT Periods (sec)

Mode	Caltrans	Roller
Longitudinal	0.6068	0.6425
Transverse	0.2979	0.7447
Vertical	0.0972	0.0900
Torsion	-	-

In addition to determining the fundamental periods for the longitudinal, transverse, and vertical displacements, the mode shapes of the deck are also determined from the FFT analysis. The mode shapes are determined by plotting the peak values from the FFT analyses at each point along the deck. These mode shapes are shown in Fig. F2 (a) through (c).

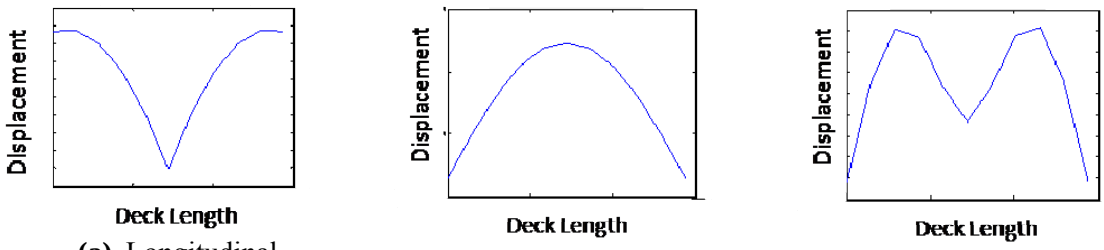

(a) Longitudinal **(b)** Transverse **(c)** Vertical

Fig. F2. Matlab FFT Mode Shapes

The FFT peak values for the mode shape in the longitudinal direction are all extremely close to each other; therefore, the shape is close to a straight line. The

transverse direction shows that the column deflects more than the abutments because the mid-span of the deck is displaced farther than the ends. The vertical mode shape shows how the column and abutments hold the deck down at the mid-span and ends of the deck, respectively. The mode shapes for both the Caltrans and the Roller abutment cases are the same; however, as stated previously, the modal frequencies are different.

Matlab TDD (Time Domain Decomposition) program

Another method, which is quite similar to the FFT, is the Time Domain Decomposition (TDD) program developed within Matlab by Michael Reyer (Unpublished program, July 2007). This purpose of this program is to determine the modal frequencies and mode shapes for any given structure, based solely on the acceleration time history response. This response can be from either forced or free vibration; for this case, the same free vibration data used for the FFT analysis is used. The TDD program essentially performs a FFT on the data and then determines the first few modal frequencies and corresponding shapes. The difference between TDD and the FFT analysis is that TDD is a complete program which was previously developed; however, the FFT analysis within Matlab is simply created using the "fft" command within Matlab. Just like the FFT analysis, the TDD analysis could only determine the first mode in each direction from the supplied response data. The modal periods obtained from TDD for the longitudinal, transverse, and vertical directions of each bridge (Caltrans and Roller supports) are shown in Table F4.

Table F4. Matlab TDD Periods (sec)

Mode	Caltrans	Roller
Longitudinal	0.6023	0.6399
Transverse	0.3011	0.7313
Vertical	0.0975	0.0898
Torsion	-	-

As shown, the periods obtained from TDD are extremely similar to those obtained from the FFT analysis; this is expected because both analysis methods used the same input data and performed very similar analyses. The mode shapes determined with TDD are also essentially the same as those obtained from the FFT analysis.

OpenSees pushover results

A fifth way to determine the periods for the longitudinal, transverse, and vertical displacement modes is to perform a bilinear analysis on the static pushover results obtained from OpenSees. Six different pushover analyses are performed: one for each direction with both the Caltrans and roller abutments. The pushover force is applied at the top node of the column (where it attaches to the mid-span of the deck), and the relative displacement between the top and bottom of the column is recorded. Plots are then created to compare the total pushover force with the relative displacement of the column. The initial stiffness values obtained from fitting a bilinear curve to the pushover data are used with an equivalent lumped mass at the top of the column to calculate the fundamental periods for a single degree of freedom system. The equivalent mass and the fundamental periods are calculated using the following equations,

$$m = \frac{1}{2}\left(m_{deck} + m_{col}\right) \tag{F1}$$

$$T = 2\pi\sqrt{\frac{m}{k}} \tag{F2}$$

where k is the initial stiffness obtained from the bilinear analysis, m_{deck} is the mass of the full deck, m_{col} is the mass of the entire column, and m is the equivalent lumped mass. The lumped mass used for these calculations is found to be 1.699 k-s^2/in. A comparison of the periods obtained from the pushover analyses for both the Caltran and roller abutment cases is shown in Table F5.

Table F5. OpenSees Pushover Periods (sec)

Mode	Caltrans	Roller
Longitudinal	0.4762	0.5518
Transverse	0.2011	0.6172
Vertical	0.0848	0.0848
Torsion	-	-

As an example, the static pushover curves for both the Caltrans and roller abutment cases in the transverse direction are shown in Fig. F3. The Caltrans abutment leads to an increase in the stiffness of the structure; this is seen by the increased stiffness in the pushover curve and the decreased period in Table F5.

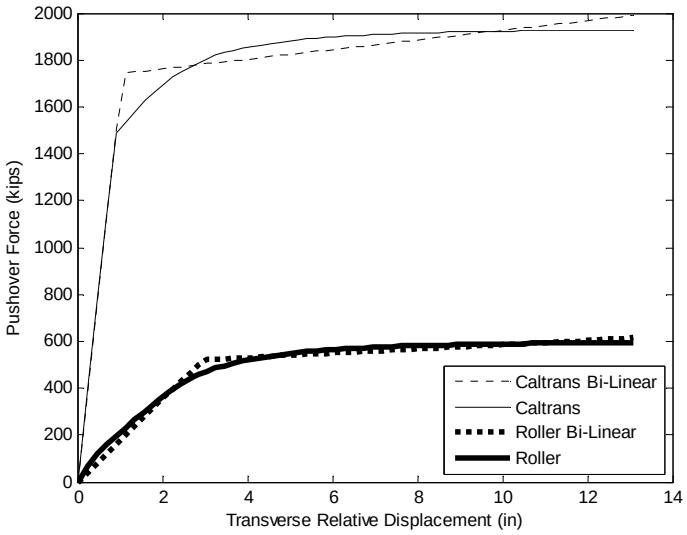

Fig. F3. Transverse Pushover Comparison

Hand Calculations

Another way to check the values for the periods in the horizontal and vertical modes is to perform simplified hand calculations. These results will not be too accurate; however, they will give a rough idea of the values that should be expected. These calculations are based on the assumption of a simple cantilever column with a single lumped mass at the top. This simplified single degree of freedom system allows easier calculations for the column axial and bending stiffnesses. The relationships used to find the column stiffnesses due to bending and axial loads are given by the following equations.

$$k_{bending} = \frac{3EI}{L^3} \tag{F3}$$

$$k_{axial} = \frac{EA}{L} \tag{F4}$$

The periods are then calculated using the same method as the pushover analysis. These results do not relate directly to either the Caltrans or roller abutment cases; however, they are closer to the roller abutment case because the horizontal motion is unrestrained. The values of the periods obtained for the horizontal (longitudinal and transverse) and vertical directions are given in Table F6.

Table F6. Hand Calculation Periods (sec)

Mode	Caltrans	Roller
Longitudinal	-	0.4500
Transverse	-	0.4500
Vertical	-	0.0410
Torsion	-	-

Many simplifications are made for the hand calculations which are not necessarily valid for the actual bridge. First of all, the entire bridge is modeled as a single degree of freedom system with one lumped mass accounting for half of the deck and half of the column. Secondly, the stiffnesses (and resulting periods) for both the longitudinal and transverse directions are assumed to be equal. The interaction from the top of column into the deck is not accounted for, and this rigid connection affects the stiffness of the column.

PEER Report

In another attempt to validate the modal periods, the values obtained by Mackie and Stojadinović (2003) are compared with those obtained with this model. The values obtained in the PEER report (Mackie and Stojadinović 2003) are for a structure with

slightly different geometrical and material properties; however, they provide a benchmark for the periods expected in the longitudinal and transverse modes. For the base bridge used by Mackie and Stojadinović (2003), the longitudinal period is reported to be T = 0.55 sec and the transverse period is reported to be T = 0.64 sec. When roller supports are used at the edge of the bridge deck (the base bridge), the transverse mode is dominant; however, once the Caltrans abutments are added at the deck support locations, Mackie and Stojadinović (2003) report that the longitudinal mode dominates. This is explained by the additional stiffness added by the abutments in the transverse direction. The Caltrans abutment does affect the motion in both the longitudinal and transverse directions, and the supports are modeled with a gap element in OpenSees. This gap element allows the deck to move freely for a specified distance (the gap) before the motion is resisted by a spring with a constant stiffness. The reason that the longitudinal direction controls in the Caltrans abutment case is because the gap is set at 6 inches for that direction while the gap in the transverse direction is set at 0 inches. This essentially means that the motion in the transverse direction is restricted sooner than in the longitudinal direction.

APPENDIX G

DAMPING VERIFICATION

The damping ratio is verified in two ways: the logarithmic decrement method and the half-power bandwidth method. Both methods will be explained here.

Logarithmic Decrement Method

The logarithmic decrement method uses the free vibration response data directly to calculate the level of viscous damping. The following equations are used to calculate the damping ratio,

$$\delta = \ln\left(\frac{y_n}{y_{n+1}}\right) \tag{G1}$$

$$\zeta = \frac{\delta}{\sqrt{4\pi^2 + \delta^2}} \tag{G2}$$

where ζ is the damping ratio, y_n is the value of any given peak, and y_{n+1} is the value of the subsequent peak. Fig. G1 shows these variables graphically.

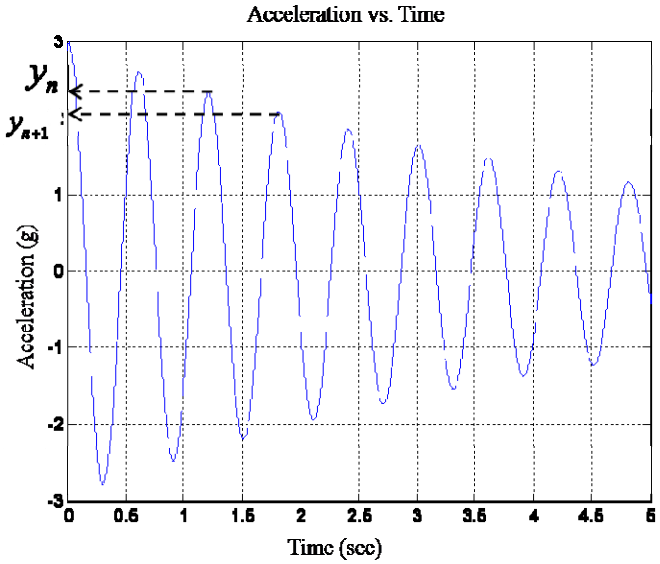

Fig. G1. Logarithmic Damping - Caltrans

The free-vibration results from the longitudinal direction with the Caltrans abutment case are shown in Fig. G1; from these results, y_n is found to be 2.6 and y_{n+1} is found to be 2.3. These values allow δ to be calculated as 0.1226 and the damping ratio, ζ, to be calculated as 1.95%.

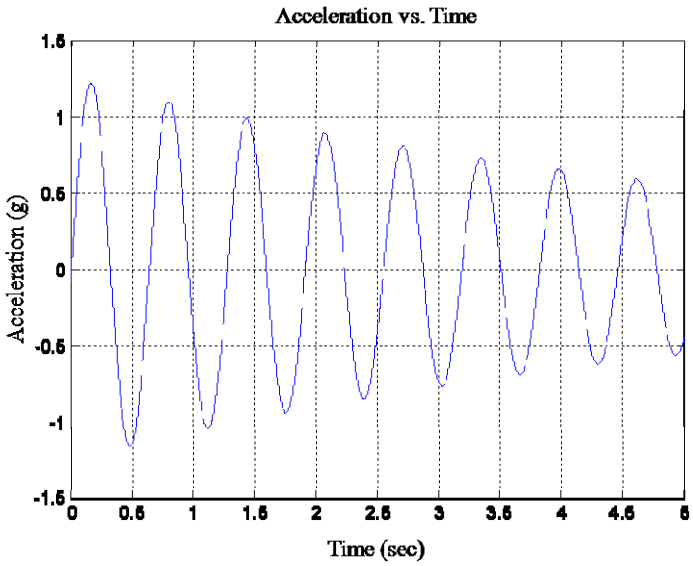

Fig. G2. Logarithmic Damping - Roller

The free-vibration results for the roller abutment in the longitudinal direction are shown in Fig. G2, where y_n is found to be 1.13 and y_{n+1} is found to be 1.10. This leads to a value of 0.1222 for δ and a damping ratio, ζ, of 1.94%. The results of the logarithmic decrement method verify that the structure is indeed experiencing 2% damping in the OpenSees model.

Half-Power Bandwidth Method

The second method used to verify the damping ratio is the half-power bandwidth method. This method requires that the response data be transformed into the frequency domain. This is easily done using the FFT procedure in Matlab. The damping ratio is then calculated with the following equation,

$$2\zeta = \frac{\omega_2 - \omega_1}{\omega_n} \tag{G3}$$

where ω_1, ω_2, and ω_n are frequency values which are shown in Fig. G3. The value for ω_n corresponds to the peak amplitude value of the FFT analysis ($X_{\max}$), and the values for ω_1 and ω_2 represent the frequencies where the power is 3dB less than the maximum $\left(X_{\max}/\sqrt{2}\right)$. A decrease of 3dB represents a reduction in half of the power, hence the name of this method.

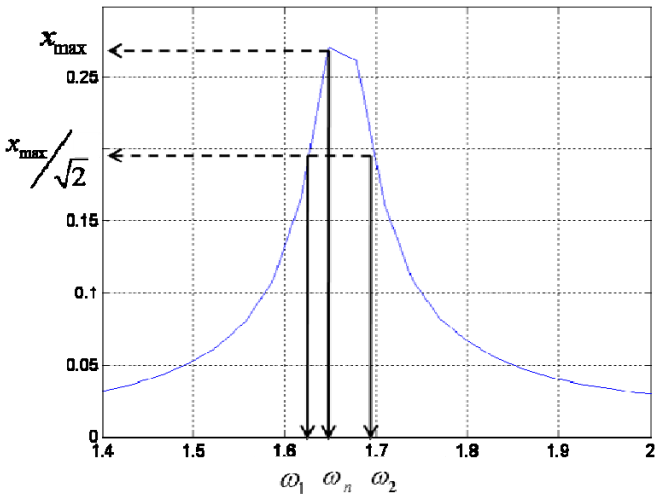

Fig. G3. Half-Power Bandwidth Damping - Caltrans

The results of the FFT in the longitudinal direction for the Caltrans abutment case are shown in Fig. G3; from this plot, $X_{\max}$ is found to be 0.27. As a result, ω_1, ω_2, and ω_n are determined to be 1.630, 1.648, and 1.700, respectively. These values yield a damping ratio of 2.1%.

The FFT plot for a similar analysis for the roller abutment case is shown in Fig. G4. From this plot, $X_{\max}$ is found to be 0.14 and ω_1, ω_2, and ω_n are determined to be 1.540, 1.557, and 1.605, respectively. The damping ratio is then calculated to be 2.09%.

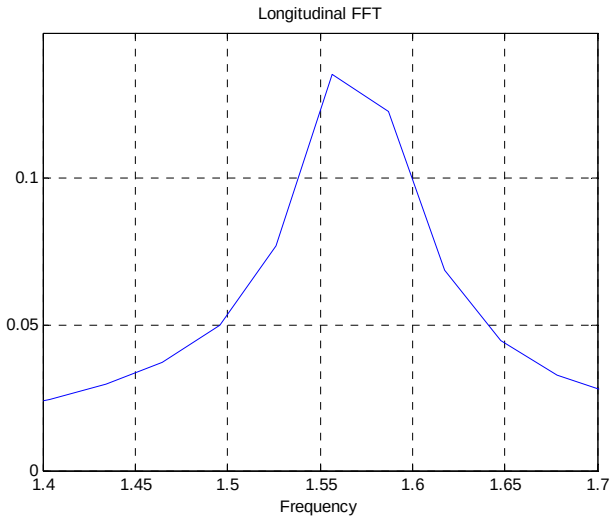

Fig. G4. Half-Power Bandwidth Damping - Roller

Similar to the logarithmic decrement method, the half-power bandwidth method confirmed the damping ratio to be approximately 2%. Although only the results in the longitudinal direction are checked to verify the damping, similar results are expected in the transverse and vertical directions.

APPENDIX H

ADDITIONAL DEMAND MODELS

Maximum Total Drift vs. Spectral Displacement/Drift

As mentioned in this report, a demand model is created based on the relationship between the maximum total drift obtained from OpenSees and the square root of the sum of the squares of the spectral displacement values in both the longitudinal and transverse directions. The following equations, similar to those for spectral acceleration given in this report, explain the variables in this demand model.

$$\Delta_{total,true} = \max\left(\sqrt{\Delta_x^2 + \Delta_y^2}\right) \tag{H1}$$

$$S_{d,SRSS} = \sqrt{S_{d,x}^2 + S_{d,y}^2} \tag{H2}$$

Fig. H1 (a) and (b) show the demand model in both the natural log and original space.

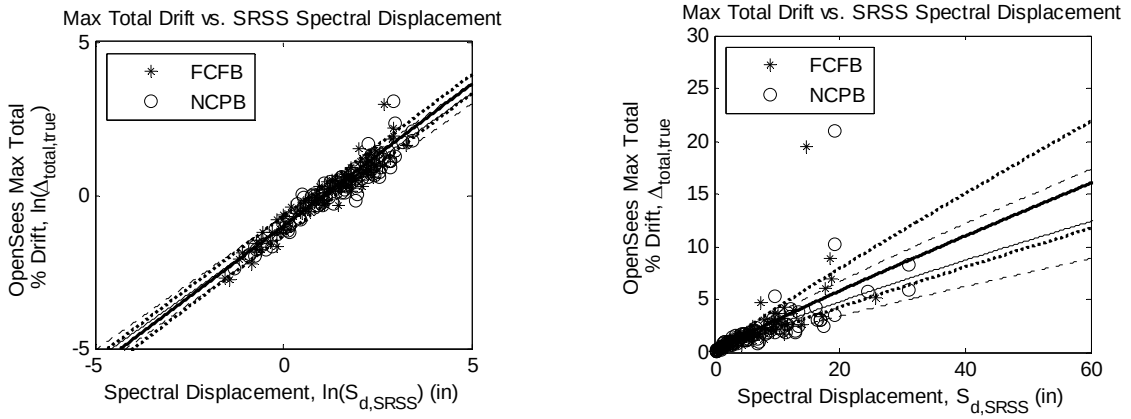

(a) Natural Log Space (b) Original Space

Fig. H1. Demand Model (based on $S_{d,SRSS}$)

Table H1 gives the values for the unknown parameters, along with the corresponding statistical information for each parameter, for the previously described demand model.

Table H1. MLE Statistics for Parameters in Total Demand Model ($S_{d,SRSS}$)

				Correlation Coefficients		
Case	Parameter	Mean	Standard Deviation	θ_0	θ_1	σ
FCFB	θ_0	-1.0210	0.0480	1.0	-0.7188	0.0228
	θ_1	0.9264	0.0323	-0.7188	1.0	-0.0000
	σ	0.3113	0.0748	0.0228	-0.0000	1.0
FCPB	θ_0	-0.9882	0.0523	1.0	-0.7485	-0.0268
	θ_1	0.9276	0.0333	-0.7485	1.0	0.0320
	σ	0.3287	0.0252	-0.0268	0.0320	1.0
NCFB	θ_0	-1.0820	0.0535	1.0	-0.7927	0.0348
	θ_1	0.8724	0.0299	-0.7927	1.0	-0.0192
	σ	0.3195	0.0247	0.0348	-0.0192	1.0
NCPB	θ_0	-1.0506	0.0587	1.0	-0.7992	-0.0341
	θ_1	0.8710	0.0337	-0.7992	1.0	0.0481
	σ	0.3353	0.0253	-0.0341	0.0481	1.0

One limitation of the previous demand model is that the spectral displacement values along the x-axis have units of inches while the OpenSees data along the y-axis is in percent drift. As a result, the data on both axes cannot be directly compared. Because of this limitation, one more demand model is developed following the same procedure. This demand model is almost identical to the previous one; however, it accounts for the spectral drift, as opposed to the spectral displacement. The drift value effectively

normalizes the spectral displacement data based on the height of the column and allows the data to be directly compared with the OpenSees total drift values. Fig. H2 (a) and (b) show the results of this demand model.

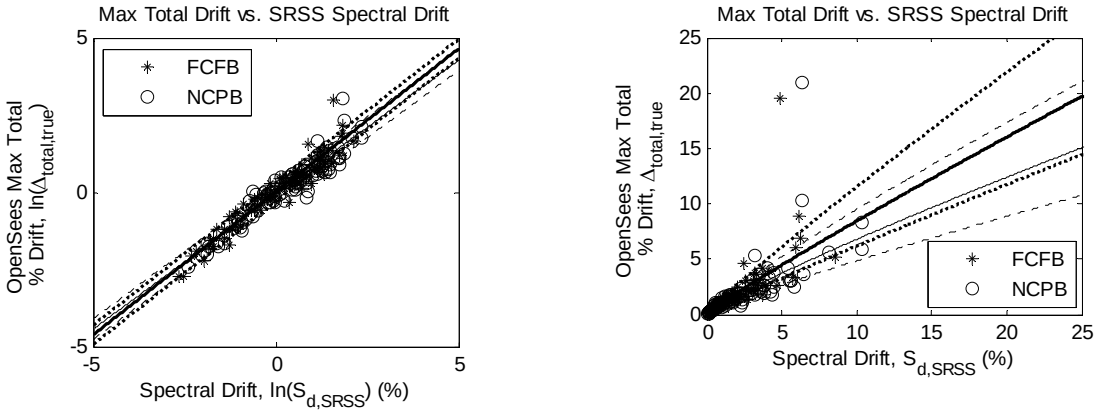

(a) Natural Log Space

(b) Original Space

Fig. H2. Demand Model (based on $S_{d,SRSS}(\%)$)

The values for the unknown parameters for each case, and their corresponding statistical data, are shown in Table H2 for this demand model.

Table H2. MLE Statistics for Parameters in Total Demand Model ($S_{d,SRSS}(\%)$)

				Correlation Coefficients		
Case	Parameter	Mean	Standard Deviation	θ_0	θ_1	σ
FCFB	θ_0	-0.0033	0.0338	1.0	-0.0910	0.0035
	θ_1	0.9267	0.0306	-0.0910	1.0	-0.0481
	σ	0.3113	0.0235	0.0035	-0.0481	1.0
FCPB	θ_0	-0.0309	0.0336	1.0	0.0484	0.0635
	θ_1	0.9276	0.0265	0.0484	1.0	-0.0888

Table H2. Continued

Case	Parameter	Mean	Standard Deviation	Correlation Coefficients		
				θ_0	θ_1	σ
	σ	0.3287	0.0238	0.0635	-0.0888	1.0
NCFB	θ_0	-0.1236	0.0360	1.0	-0.3446	-0.0877
	θ_1	0.8724	0.0372	-0.3446	1.0	0.2393
	σ	0.3195	0.0259	-0.0877	0.2393	1.0
NCPB	θ_0	-0.0937	0.0398	1.0	-0.3097	-0.0384
	θ_1	0.8710	0.0325	-0.3097	1.0	0.0179
	σ	0.3353	0.0251	-0.0384	0.0179	1.0

OpenSees Maximum Total Drift vs. Calculated Maximum Total Drift (based on S_d)

Following the same procedure explained in the report, a demand model is developed comparing the maximum total drift obtained from OpenSees to the maximum total drift calculated based on the spectral displacement data in the separate longitudinal and transverse directions. The first step in creating this demand model is to develop the relationship between the maximum drift and the spectral displacement values in both the longitudinal and transverse directions. These relationships are shown for the FCFB and NCPB cases in Fig. H3 (a) and (b) in the natural log space.

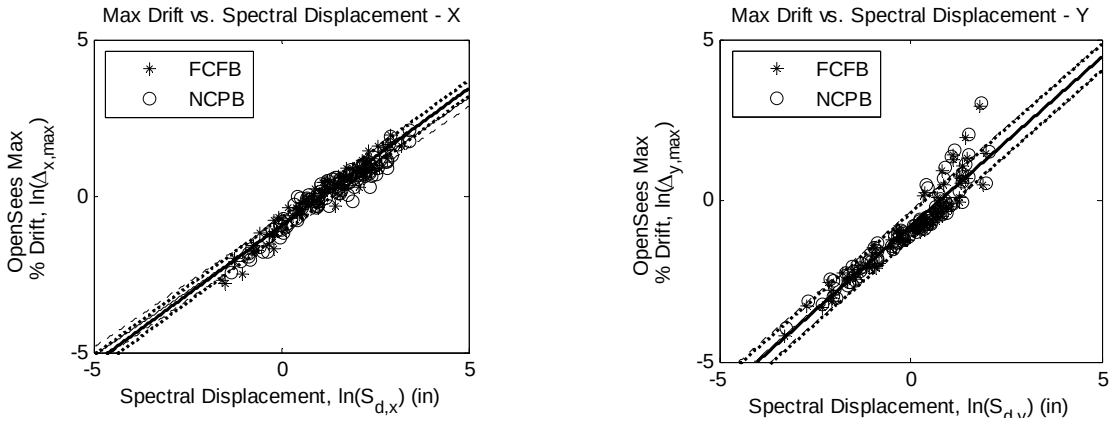

(a) Longitudinal Direction (b) Transverse Direction

Fig. H3. Maximum Drift vs. Spectral Displacement

The data in the previous figures is analyzed using the MLE method, and equations of the following form are developed,

$$\ln\left(\Delta_{x_{\max,calc}}\right) = \theta_{0,x} + \theta_{1,x} \cdot \ln\left(S_{d,x}\right) \pm \sigma_x \varepsilon \tag{H3}$$

$$\ln\left(\Delta_{y_{\max,calc}}\right) = \theta_{0,y} + \theta_{1,y} \cdot \ln\left(S_{d,y}\right) \pm \sigma_y \varepsilon \tag{H4}$$

where $\Delta_{x_{\max,calc}}$ is the maximum drift in the longitudinal direction, $\Delta_{y_{\max,calc}}$ is the maximum drift in the transverse direction, and $S_{d,x}$ and $S_{d,y}$ are the spectral displacement values in the longitudinal and transverse directions, respectively. The values for the unknown parameters (θ_0, θ_1, and σ) in each equation are given in Table H3 and Table H4 below for the longitudinal and transverse directions, respectively.

Table H3. MLE Statistics for Parameters in Longitudinal Demand Model ($S_{d,x}$)

Case	Parameter	Mean	Standard Deviation	Correlation Coefficients		
				$\theta_{0,x}$	$\theta_{1,x}$	σ_x
FCFB	$\theta_{0,x}$	-0.9755	0.0375	1.0	-0.6898	-0.0002
	$\theta_{1,x}$	0.8799	0.0245	-0.6898	1.0	-0.0412
	σ_x	0.2558	0.0193	-0.0002	-0.0412	1.0
FCPB	$\theta_{0,x}$	-0.9418	0.0396	1.0	-0.6651	0.0136
	$\theta_{1,x}$	0.8814	0.0251	-0.6651	1.0	0.0461
	σ_x	0.2771	0.0781	0.0136	0.0461	1.0
NCFB	$\theta_{0,x}$	-1.0402	0.0440	1.0	-0.7924	-0.0594
	$\theta_{1,x}$	0.8250	0.0247	-0.7924	1.0	0.0584
	σ_x	0.2515	0.0193	-0.0594	0.0584	1.0
NCPB	$\theta_{0,x}$	-1.0124	0.0465	1.0	-0.7449	-0.0296
	$\theta_{1,x}$	0.8248	0.0258	-0.7449	1.0	0.0153
	σ_x	0.2746	0.0209	-0.0296	0.0153	1.0

Table H4. MLE Statistics for Parameters in Transverse Demand Model ($S_{d,y}$)

Case	Parameter	Mean	Standard Deviation	Correlation Coefficients		
				$\theta_{0,y}$	$\theta_{1,y}$	σ_y
FCFB	$\theta_{0,y}$	-0.8133	0.0445	1.0	0.0956	-0.0386
	$\theta_{1,y}$	1.0484	0.0376	0.0956	1.0	-0.0446
	σ_y	0.4136	0.0315	-0.0386	-0.0446	1.0
FCPB	$\theta_{0,y}$	-0.7958	0.0446	1.0	0.0712	0.0155
	$\theta_{1,y}$	1.0553	0.0385	0.0712	1.0	-0.0047
	σ_y	0.4209	0.0328	0.0155	-0.0047	1.0
NCFB	$\theta_{0,y}$	-0.7952	0.0453	1.0	0.0874	0.0275
	$\theta_{1,y}$	1.0304	0.0407	0.0874	1.0	0.0473
	σ_y	0.4248	0.0316	0.0275	0.0473	1.0

Table H4. Continued

Case	Parameter	Mean	Standard Deviation	Correlation Coefficients		
				$\theta_{0,y}$	$\theta_{1,y}$	σ_y
NCPB	$\theta_{0,y}$	-0.7768	0.0452	1.0	-0.0118	-0.0266
	$\theta_{1,y}$	1.0393	0.0382	-0.0118	1.0	-0.0163
	σ_y	0.4319	0.0322	-0.0266	-0.0163	1.0

Once the equations for the maximum drifts in the longitudinal and transverse directions are developed, the data is combined to calculate the maximum total drift. The following equation is used for this calculation.

$$\Delta_{total,calc} = \sqrt{\Delta^2_{x_{\max,calc}} + \Delta^2_{y_{\max,calc}}} \tag{H5}$$

After the calculated maximum total drift is determined, it is compared to the maximum total drift obtained from the OpenSees dynamic results. The resulting plot is shown in Fig. H4 for the FCFB and NCPB cases.

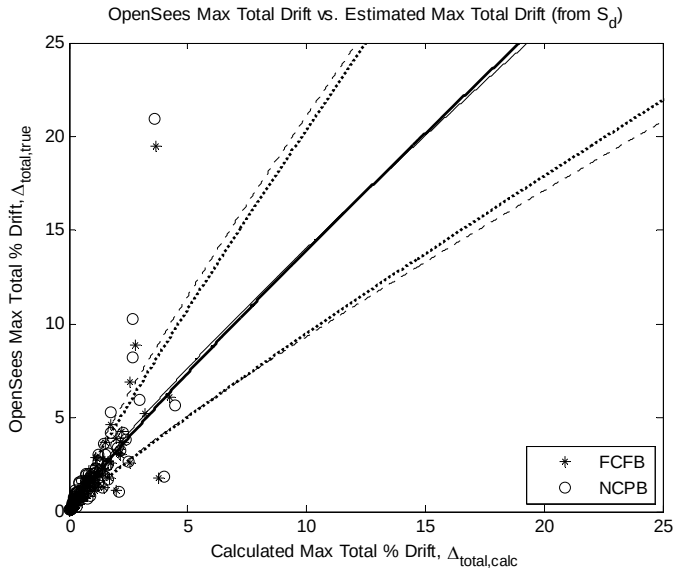

Fig. H4. OpenSees Maximum Drift vs. Calculated Maximum Drift (based on S_d)

Similar to the demand model based on S_a, the data in the previous demand model can be represented with a single linear model in the natural logarithmic space with the following equation,

$$\ln\left(\Delta_{total,true}\right) = \theta_0 + \theta_1 \cdot \ln\left(\Delta_{total,calc}\right) \pm \sigma\varepsilon \tag{H6}$$

where all unknowns are defined previously in this report. The values for all unknown parameters in this demand model are shown in Table H5.

Table H5. MLE Statistics for Parameters in Total Demand Model (baed on S_d)

				Correlation Coefficients		
Case	Parameter	Mean	Standard Deviation	θ_0	θ_1	σ
FCFB	θ_0	0.5172	0.0556	1.0	0.4627	-0.0025
	θ_1	0.9291	0.0408	0.4627	1.0	-0.1216
	σ	0.3867	0.0312	-0.0025	-0.1216	1.0
FCPB	θ_0	0.5272	0.0513	1.0	0.4425	-0.1176
	θ_1	0.9273	0.0397	0.4425	1.0	-0.0485
	σ	0.4032	0.0320	-0.1176	-0.0485	1.0
NCFB	θ_0	0.6131	0.0508	1.0	0.4763	-0.0620
	θ_1	0.8946	0.0402	0.4763	1.0	0.0054
	σ	0.3915	0.0304	-0.0620	0.0054	1.0
NCPB	θ_0	0.6189	0.0514	1.0	0.4243	-0.0123
	θ_1	0.8884	0.0404	0.4243	1.0	0.0366
	σ	0.4061	0.0324	-0.0123	0.0366	1.0

This demand model can be used in conjunction with the capacity model described in this report to determine the fragility of the bridge.

APPENDIX I

CAPACITY MODEL VERIFICATION

When verifying the capacity model for this bridge, a section analysis is performed using PCA Column, USC_RC, and OpenSees to determine the critical moment and curvature values required. Table I1 shows the results for the FCFB case, and Table I2 shows the results for the NCPB case. The results are slightly different because of the modeling assumptions made in the respective programs and the slight difference in the definition of the parameters.

Table I1. Moment-Curvature Comparisons (FCFB)

Property	OpenSees	USC_RC	PCA Column
$\phi_y\ (1/in)$	0.00010414	0.00011700	0.00006162
$\phi_u\ (1/in)$	0.00140997	0.00106904	0.00074618
$M_y\ (k \cdot in)$	88,494	75,262	79,661
$M_I\ (k \cdot in)$	102,435	125,793	106,214

Table I2. Moment-Curvature Comparisons (NCPB)

Property	OpenSees	USC_RC	PCA Column
$\phi_y\ (1/in)$	0.00012049	0.00014001	0.00007358
$\phi_u\ (1/in)$	0.00136994	0.00102591	0.00102743
$M_y\ (k \cdot in)$	61,542	67,428	63,728
$M_I\ (k \cdot in)$	74,191	105,267	88,512

A graphical comparison of the FCFB data is also developed, and it can be seen in Fig. I1. This figure shows that the values obtained for the yield curvature and moment are fairly comparable among the three cases; however, the definition of the ultimate curvature is significantly different in all three cases.

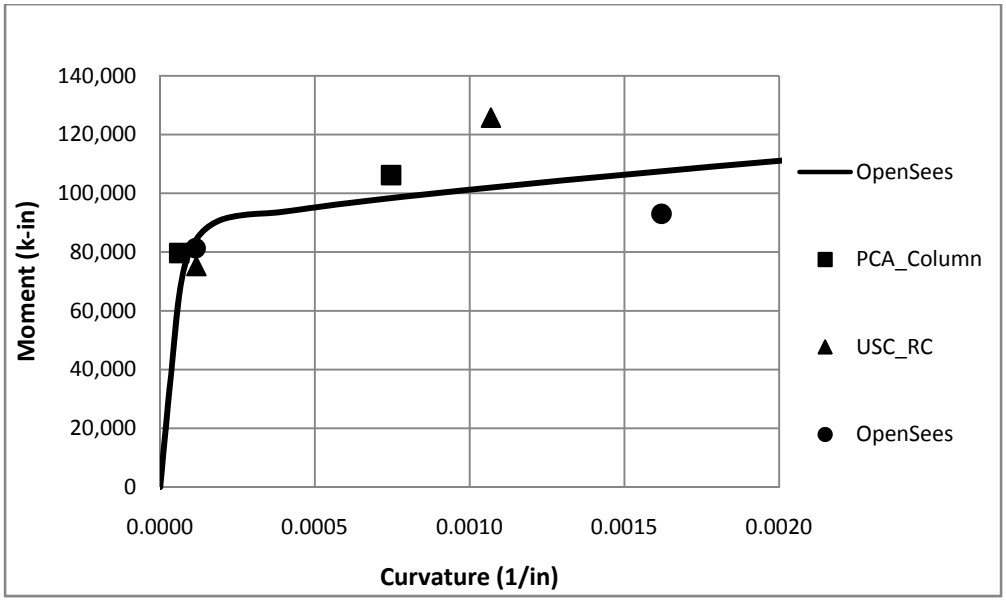

Fig. I1. Moment Curvature Comparison

The values obtained from OpenSees will be used for the capacity model because they are obtained following the procedure presented in Gardoni et al. (2002). Based on the results obtained from PCA Column and USC_RC, the OpenSees values are verified to be within the correct range and are assumed to be accurate.

APPENDIX J

ADDITIONAL FRAGILITIES

Using the demand model developed in APPENDIX H and the capacity model developed in this report, the demand, capacity, and fragility curves shown in Fig. J1, conditioned on $S_{d,SRSS}$ are developed. The same process described in this thesis for the model conditioned on $S_{a,SRSS}$ is used when developing this figure.

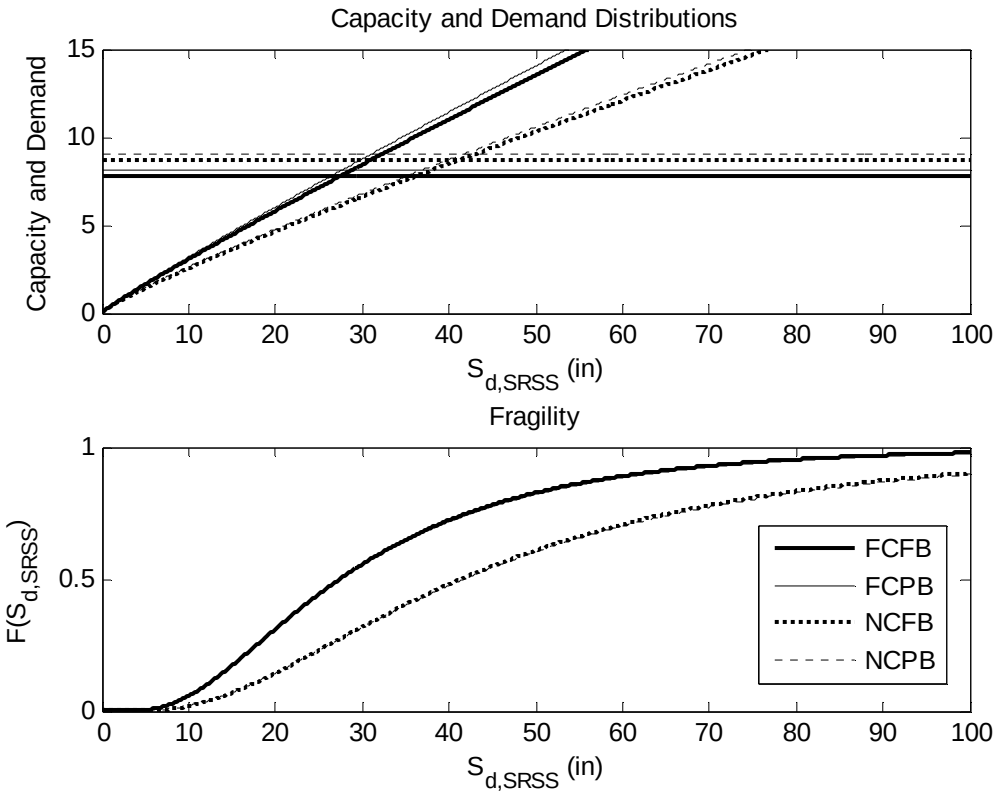

Fig. J1. Capacity and Demand Models with Corresponding Fragility (based on $S_{d,SRSS}$)

VITA

Name: Jessica Anne Harvat

Address: Department of Civil Engineering
Texas A&M University
3136 TAMU
College Station, Texas 77843

Email Address: jessica.harvat@gmail.com

Education: B.S., Civil Engineering, Texas A&M University, 2007